Structural properties of nanoscopic ring systems and their optical response

VIVALDO LOPES OLIVEIRA NETO

Federal University of São Carlos

Physics Department

Structural properties of nanoscopic ring systems and their optical response

VIVALDO LOPES OLIVEIRA NETO

PROF. DR. VICTOR LOPEZ RICHARD

Thesis presented to Physics Department of the Federal University of São Carlos - DF/UFSCar as part of the requirements for the PhD title in Physics.

UFSCar - São Carlos/SP

Juny/2016

Folha de Aprovação
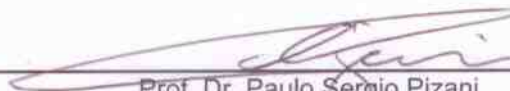
Assinaturas dos membros da comissão examinadora que avaliou e aprovou a Defesa de Tese de Doutorado do candidato Vivaldo Lopes Oliveira Neto, realizada em 30/03/2016:

Prof. Dr. Victor Lopez Richard
UFSCar

Prof. Dr. Paulo Sergio Pizani
UFSCar

Prof. Dr. Marcio Peron Franco de Godoy
UFSCar

Prof. Dr. Guo-Qiang Hai
USP

Prof. Dr. Marcelo Zoega Maialle
UNICAMP

to my family

Acknowledge

I would like to thanks:

Victor and Sergio, whereby I have great admiration, for their teachings, being patience and very friendly with me during the last years enabling the success of this project.

Nancy, Sergio, Julia and the rest of the family for receive Sarah and me wonderfully well at their house in Athens-OH, where we really felt at home, although being in another country.

All my group colleagues and professors for teachings and friendship during these years.

All my work collaborators that have engaged in works resulting in some papers.

My department friends and their families: Leonilson, Nanna, Jaldair, Hugo, Raphael, Vanessa, Daniel, Maycon, Renilton, Ana Paula and Clarissa for conferences travels and friendship.

My friends out of the department (Carpas's Club): Rafinha, Ivan, Carol, Tuti, Marcão, Zelda, Willian, Vinicius, Titi, Dinamerico, Joelma, PH, Ana, Rafael (Moh), Lu, Juninho, Pri, Du and Fran for our meetings and celebrations together.

CAPES for the financial support and sandwich stage.

Finally, I would like thanks all my family, in special my mother and wife for immense dedication, incentive and love.

There is no shortcut to success

" *The separation of talent and skill is one of the greatest misunderstood concepts for people who are trying to excel, who have dreams, who want to do things. Talent you have naturally. Skill in only developed by hours and hours and hours of beating on your craft.*"

(Will Smith)

Abstract

In this thesis, the electronic and structural properties of nanostructured systems were studied aiming to get a realistic model for quantum rings, potentially adaptable for quantum dots. To attain these goals, several studies supported by experimental results were carried out that allowed the introduction to the building blocks for the theoretical models such as: the envelope function approach within the k.p approximation in quantum wells, and quantum ring/dot with perpendicular magnetic field and without spin-orbit interaction. In these models, the effects of size, strain and localization were subsequently introduced to understand the ring formation process and their effects in the photoluminescence and magneto-photoluminescence. The experimental results of atomic force microscopy indicated the importance of structural properties and the types of asymmetries possibly found in quantum rings after the growth process. The understanding of these effects and the evidence of the anisotropy in a preferential direction of the ring helped building more realistic models for the potential profiles. Various systems were then studied with success. They also included a controllably magnetic field (both in magnitude and orientation), beside the geometric deformation, making the ring ellipsoidal, and taking into account the spin-orbit interaction. The most realistic model was used to analyze the Berry phase generation and the relative weight of the contribution of each term of the Hamiltonian.

Keywords: Quantum Rings. K.P Method. Berry Phase. Asymmetry.

Resumo

Nesta tese de doutorado, as propriedades eletrônicas e estruturais de sistemas nano estruturados foram estudadas visando a obtenção de um modelo realístico para anéis quânticos potencialmente adaptáveis a pontos quânticos. Para alcançar este objetivo, foram feitos alguns estudos, apoiados por resultados experimentais, que permitiram a construção passo a passo do modelo teórico, como: aproximação da função envelope na representação k.p em poços quânticos e anéis/pontos quânticos com campo magnético perpendicular e sem interação spin-órbita. Nestes modelos, os efeitos do tamanho, tensão e localização foram introduzidos subsequentemente para entender o processo de formação do anel e os resultados apresentados na fotoluminescência e na magneto-luminescência. O resultado experimental da microscopia de força atômica nos levou a analisar a importância das propriedades estruturais e os tipos possíveis de assimetria encontrados em anéis quânticos devido ao processo de crescimento. O entendimento desses efeitos e a evidência de anisotropia em uma direção preferencial do anel ajudou na construção de modelos mais realísticos para os perfis de potencial. Deste modo, vários sistemas foram estudados com sucesso. Eles também possuíam um campo magnético controlável (ambas, magnitude e orientação), além da deformação geométrica, que torna o anel elipsoidal, e a interação spin-órbita. O modelo mais realístico foi usado para analisar a geração da fase de Berry e o peso da contribuição de cada termo do Hamiltoniano.

Palavras-chave: Anéis Quânticos. Método K.P. Fase de Berry. Assimetria.

List of Figures

List of Tables

List os Abbreviations

QD   Quantum Dot

QWr   Quantum Wire

QR   Quantum Ring

MBE   Molecular Beam Epitaxy

AB   Aharonov-Bohm

PL   Photoluminescence

SO   Spin-Orbit

QW   Quantum Well

BIA   Bulk Inversion Asymmetry

SIA   Structure Inversion Asymmetry

LH   Light Hole

HH   Heavy Hole

AFM   Atomic Force Microscopy

HRXRD   High-Resolution X-Ray Diffraction

DSP   Degree of Spin Polarization

TEM   Transmission Electron Microscope

FEM   Finite-Element Method

Contents

Chapter 1

INTRODUCTION

Recent progress in nanostructure engineering has enabled foreseeing opto-electronic applications of systems based on quantum dots (QDs), quantum wires (QWrs) and quantum rings (QRs) such as low-threshold lasers [1], infrared photodetectors [2], solar cells [3], biosensors [4,5], spintronic gates [6], etc. In view of the wide application of QDs, QWrs, and QRs for the creation of efficient opto-electronic devices, extensive studies have been carried out in many nanoscale structures for understanding their basic properties and the physics underneath [7–14]. Among the possible nanostructures, the QRs present attractive features for fundamental quantum mechanics studies and applications, like terahertz detectors [15].

The nanostructures studied here were obtained by molecular beam epitaxy (MBE) [16], and in case of QRs, they are formed via the Stranski-Krastanov method [9, 10], where a very thin cap-layer of the same material from the barrier is deposited over the QDs previously formed by MBE. After this procedure, material from the QD center is ejected and redistributed around the QDs, creating a volcano crater-like ring nanostructure. Several studies have discussed the formation of the QRs in terms of the thermodynamic equilibrium and kinetic transition, but a satisfactory explanation of these processes is still under scrutiny [17–22]. This unique toroidal topology displayed by the QRs has also allowed the observation of the Aharonov-Bohm (AB) effect [23] in transport experiments [24–27].

The AB interference in type-I systems, where both electron and hole move together inside the QR, has been found in the magneto-photoluminescence from self-assembled InGaAs/GaAs QR single layer structures [28]. It has also been shown that optical emissions from type-II ZnTe/ZnSe QDs display large and persistent oscillations in both peak energy and intensity, thus indicating the formation of coherently rotating states in magnetic fields [28, 29].

The Stranski-Krastanov growth mode has attracted both theoretical and experimental interest [29, 30]. This method has become the main recipe for fabricating ordered arrays of QDs and QRs. To attain self-organization of nanoscopic structures with the highest possible uniformity and geometry control, a layer-by-layer growth is indispensable. Unavoidably, a vertical stack of nanoscopic islands is formed in this process. However, some unexpected geometric shapes could be observed in layer-by-layer growth, such as defects, making the resulting structure non circularly symmetric. In the case of QRs, one may find elongated/elliptical structures and QRs with punctual deformations [31]. These deformations affect directly their electronic structure.

In this thesis, we aim to build a realistic and versatile model to characterize QRs and QDs systems that allows analyzing several effects, such as those produced by strain, localization, asymmetry, spin orbit coupling, and controllable external magnetic fields. The existing models [32–37] are not able to analyze such a spectrum of effects within a single framework, which limits the study of dimensionality, for example, while our model allows verifying the combination of these effects simultaneously.

We have firstly introduced the fundamental concepts within chapter 2 and then described basic effects of the growth process in semiconductor nanostructures, in chapter 3. Here, the fundamental effects of composition, confinement, strain and localization are discussed in order to understand the complex nanostructure systems introduced later. To reach this goal we have discussed optical and magneto-optical results based on our electronic structure calculation, where the relative effects of modulation are associated to structural parameters analyzed by using multiband calculations. After that, in chapter 4, we have investigated the effects of external fields and asymmetries in QRs and QD-QR stacked structures, where one InGaAs/GaAs QR layer is grown on a vertical superlattice of InGaAs/GaAs QDs aligned laterally. This hybrid ensemble of nanostructures reveals strong optical anisotropy in the polarized photoluminescence (PL) spectrum and unusually strong oscillations of PL intensities as a function of magnetic field in both QDs and QRs spectral emission ranges. These oscillations are observed simultaneously and related to the Aharanov-Bohm interference patterns. Such a behavior of the magneto-PL can be understood in terms of joint effects associated to strain, spatial and magnetic confinements affecting the valence band states forming the magneto-exciton ground state of the hybrid structure. And finally, in chapter 5, we have studied another QR system, where an external controllable magnetic field was used together with spin orbit (SO) coupling and asymmetry effects aiming to elucidate the nature of each contribution to generates Berry phases.

In order to attain our goals, a combination of experimental results, provided by collaborators, and our theoretical procedures has been gathered to build an accurate framework for the analysis.

Till now, these efforts resulted in the following published papers:

1. Berry phase and Rashba fields in quantum rings in tilted magnetic field. Physical Review B 92, 035441 (2015).

2. Carrier transfer in vertically stacked quantum ring-quantum dot chains. Journal of Applied Physics 117, 154307 (2015).

3. Structural and magnetic confinement of holes in the spin-polarized emission of coupled quantum ring-quantum dot chains. Physical Review B 90, 125315 (2014).

4. Strain and localization effects in InGaAs(N) quantum wells: Tuning the magnetic response. Journal of Applied Physics 116, 233703 (2014).

A one year Sandwich PhD project was developed at Ohio University under the supervision of Prof. Sergio Eduardo Ulloa.

Bibliography

[1] Z. I. Alferov, Rev. Mod. Phys. **73**, 767 (2001).

[2] H. Pettersson, J. Tragardh, A. I. Persson, L. Landin, D. Hessman, and L. Samuelson, Nano Letters **6**, 229 (2006).

[3] M. Law, L. E. Greene, J. C. Johnson, R. Saykally, and P. Yang, Nature Materials **4**, 455 (2005).

[4] Y. Huang, X. Dong, Y. Shi, C. M. Li, L. J. Li, and P. Chen P, Nanoscale **2**, 1485 (2010).

[5] S. Su, Y. He, S. Song, D. Li, L. Wang, C. Fan, and S. T. Lee , Nanoscale **2**, 1704 (2010).

[6] P. Foldi, B. Molnar, M. G. Benedict, and F. M. Peeters, Phys. Rev. B **71**, 033309 (2005).

[7] Vas. P. Kunets, C. S. Furrow, T. Al. Morgan, Y. Hirono, M. E. Ware, V. G. Dorogan, Yu. I Mazur, V. P. Kunets, and G. J. Salamo, Appl. Phys. Lett. **101**, 041106 (2012).

[8] Vas. P. Kunets, C. S. Furrow, M. E. Ware, L. D. de Souza, M. Benamara, M. Mortazavi, and G. J. Salamo, J. Appl. Phys. **116**, 083102 (2014).

[9] J. Wu, Z. M. Wang, K. Holmes, E. Marega, Jr., Z. Zhou, H. Li, Yu. I. Mazur, and G. J. Salamo, Appl. Phys. Lett. **100**, 203117 (2012).

[10] J. Wu, Z. M. Wang, K. Holmes, E. Marega, Jr., Yu I. Mazur, and G. J. Salamo, J. Nanopart. Res. **14**, 919 (2012).

[11] M. D. Teodoro, V. L. Campo, Jr., V. Lopez-Richard, E. Marega, Jr., G. E. Marques, Y. Galvao Gobato, F. Iikawa, M. J. S. P. Brasil, Z.Y. AbuWaar, V. G. Dorogan, Yu. I. Mazur, M. Benamara, and G. J. Salamo, Phys. Rev. Lett. **104**, 086401 (2010).

[12] V. Lopes-Oliveira, Y. I. Mazur, L. D. Souza, L. A. B. Marçal, J. Wu, M. D. Teodoro, A. Malachias, V. G. Dorogan, M. Benamara, G. G. Tarasov, E. Marega Jr., G. E. Marques, Z. M. Wang, M. Orlita, G. J. Salamo, and V. Lopez-Richard, Phys. Rev. B **90**, 125315 (2014).

[13] Y. I. Mazur, V. G. Dorogan, M. E. Ware, E. Marega Jr., P. M. Lytvyn, Z. Ya. Zhuchenko, G. G. Tarasov, and G. J. Salamo, J. Appl. Phys. **112**, 084314 (2012).

[14] Y. I. Mazur, V. G. Dorogan, E. Marega Jr., P. M. Lytvyn, Z. Ya. Zhuchenko, G. G. Tarasov, and G. J. Salamo, New J. Physics **11**, 043022 (2009).

[15] E. Rasanen, A. Castro, J. Werschnik, A. Rubio, and E. K. U. Gross, Phys. Rev. Lett. **98**, 157404 (2007).

[16] L. L. Chang and K. Ploog, Molecular Beam Epitaxy and Heterostructures. Erice: Martinus Nijhoff Publishers, 1983.

[17] V. Baranwal, G. Biassol, S. Heun, A. Locatelli, T. O. Mentes, M. N. Orti, and L. Sorba, Phys. Rev. B **80**, 155328 (2009).

[18] G. Biasiol, R. Magri, S. Heun, A. Locatelli, T. O. Mentes, and L. Sorba, J. Cryst. Growth **311**, 1764 (2009).

[19] G. Biasiol and S. Heun, Phys. Reports **500**, 117 (2011).

[20] H-S. Ling and C-P. Lee, J. Appl. Phys. **102**, 024314 (2007).

[21] R. Blossey and A. Lorke, Phys. Rev. E **65**, 021603 (2002).

[22] A. Lorke, R. J. Luyken, J. M. García, and P. M. Petroff, Jpn. J. Appl. Phys. **40**, 1857 (2001).

[23] Y. Aharonov and D. Bohm, The Phys. Rev. **115**, 485 (1959).

[24] S. S. Buchholz, S. F. Fischer, U. Kunze, D. Reuter, and A. D. Wieck, Appl. Phys. Lett. **94**, 022107 (2009).

[25] D. Stepanenko, M. Lee, G. Burkard, and D. Loss, Phys. Rev. B **79**, 235301 (2009).

[26] T. C. G. Reusch, A. Fuhrer, M. Füchsle, B. Weber, and M. Y. Simmons, Appl. Phys. Lett. **95**, 032110 (2009).

[27] E. Ribeiro, A. O. Govorov, W. Carvalho Jr, and G. Medeiros-Ribeiro, Phys. Rev. Lett. **92**, 126402 (2004).

[28] M. D. Teodoro, V. L. Campo, Jr., V. Lopez-Richard, E. Marega, Jr., G. E. Marques, Y. Galvão Gobato, F. Iikawa, M. J. S. P. Brasil, Z.Y. AbuWaar, V. G. Dorogan, Yu. I. Mazur, M. Benamara, and G. J. Salamo, Phys. Rev. Lett. **104**, 086401 (2010).

[29] A. O. Govorov, S. E. Ulloa, K. Karrai, and R. J. Warburton, Phys. Rev. B **66**, 081309 (2002).

[30] N. A. J. M. Kleemans, I. Bominaar-Silkens, V. M. Fomin, V. N. Gladilin, D. Granados, A.G. Taboada, J. M. Garcia, P. Offermans, U. Zeitler, P.C. M. Christianen, J. C. Maan, J. T. Devreese, and P.M. Koenraad, Phys. Rev. Lett. **99**, 146808 (2007).

[31] M. P. Nowak and B. Szafran, Phys. Rev. B **80**, 195319 (2009).

[32] W.-C. Tan and J. C. Inkson, *Semicond. Sci. Technol.* **11**, 1635-1641 (1996).

[33] S.-S. Li and J.-B. Xia, J. Appl. Phys. **89**, 3434 (2001).

[34] S.-S. Li and J.-B. Xia, J. Appl. Phys. **91**, 3227 (2002).

[35] R. Rosas, R. Riera, and J. L. Marín, J. Phys.: Condens. Matter **12**, 6851 (2000).

[36] N. Kim, G. Ihm, H.-S. Sim, and K. J. Chang, Phys. Rev. B **60**, 8767 (1999).

[37] J. M. Llorens, C. Trallero-Giner, A. García-Cristóbal, and A. Cantarero, Phys. Rev. B **64**, 035309 (2001).

Chapter 2

THEORETICAL BACKGROUNDS

As stated previously, this work is a theoretical study of semiconductor nanostructured systems and tackles problems involving them. As they requested the interplay of various concepts and models, this chapter is dedicated to the introduction of the general theoretical concepts used in the work. Thus, the chapter begins with a basic description of the crystal structure and electronic properties. Then, followed by the concept of effective mass and envelope function, the **k.p** method and the Luttinger Hamiltonian are presented. They are the grounds for the conduction and valence bands simulations. Subsequently, the strain effects are introduced, ending with the description of the systems of interest: quantum wells (QWs), QDs, and QRs.

2.1   Crystal Structure and Properties

Crystals present special optical and electrical properties different from fluids and other solids, which make them useful for electro-optical and electronic applications. These properties, such as their band structure and conductivity, can be controlled during the crystal growth and doping, and are widely used for manufacturing electronic devices. To describe a crystal structure, there are three important questions to answer: what kind of lattice is present? what choice of fundamental translation vectors $\mathbf{v}_1$, $\mathbf{v}_2$ and $\mathbf{v}_3$ (that define the lattice) do we wish to make? what is the basis?

More than one lattice is always possible for a given structure, and more than one set of axes is always possible for a given lattice. The basis is identified once these choices have been made. Everything works out correctly in the end, satisfying the definition of Bravais lattice for

a crystal translation vector as [1]

$$T = u_1\mathbf{v}_1 + u_2\mathbf{v}_2 + u_3\mathbf{v}_3 \tag{2.1}$$

where u_1, u_2 and u_3 are arbitrary integers. A basis of atoms is attached to every lattice point, with every basis being identical in composition, arrangement, and orientation. A crystal structure is formed by adding a basis to every lattice point.

In Fig. 2.1, one may see an example of a primitive cell (blue parallelepiped) defined by the primitive axes $\mathbf{v}_1$, $\mathbf{v}_2$, $\mathbf{v}_3$. A primitive cell is a type of unit cell. A cell will fill all space by the repetition of suitable crystal translation operations. A primitive cell is a minimum-volume cell. There are many ways of choosing the primitive axes and primitive cells for a given lattice. The number of atoms in a primitive cell or primitive basis is always the same for a given crystal structure.
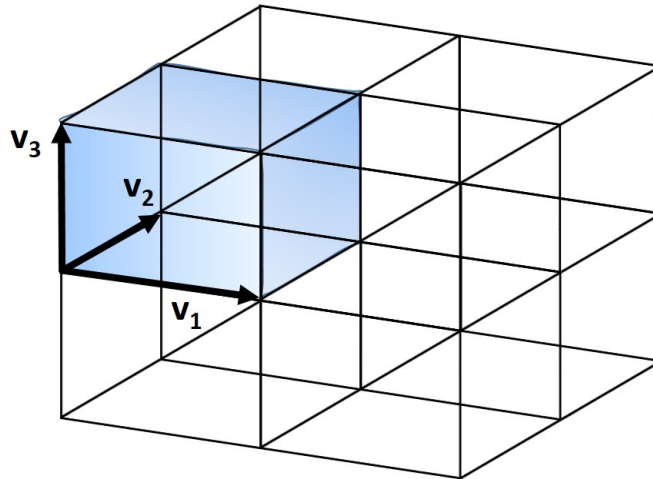
Figure 2.1: Scheme of a primitive cell, in blue, defined by the primitive axes $\mathbf{v}_1$, $\mathbf{v}_2$ and $\mathbf{v}_3$.

Bravais proved that there are only fourteen different space lattices, divided into seven crystal systems indicated in Fig. 2.2. We focus on cubic structures because that it is the symmetry of the InAs, GaAs and their alloys, studied in this thesis.

There is always one lattice point per primitive cell. If the primitive cell is a parallelepiped with lattice points at each of the eight corners, each lattice point is shared among eight cells, so that the total number of lattice points in the cell is one, as illustrated in Fig. 2.3, and the volume of a parallelepiped with axes $\mathbf{v}_1$, $\mathbf{v}_2$, $\mathbf{v}_3$ is $V_c = |\mathbf{v}_1 \cdot \mathbf{v}_2 \times \mathbf{v}_3|$. The basis associated with a primitive cell is called a primitive basis. No basis contains fewer atoms than a primitive basis contains.
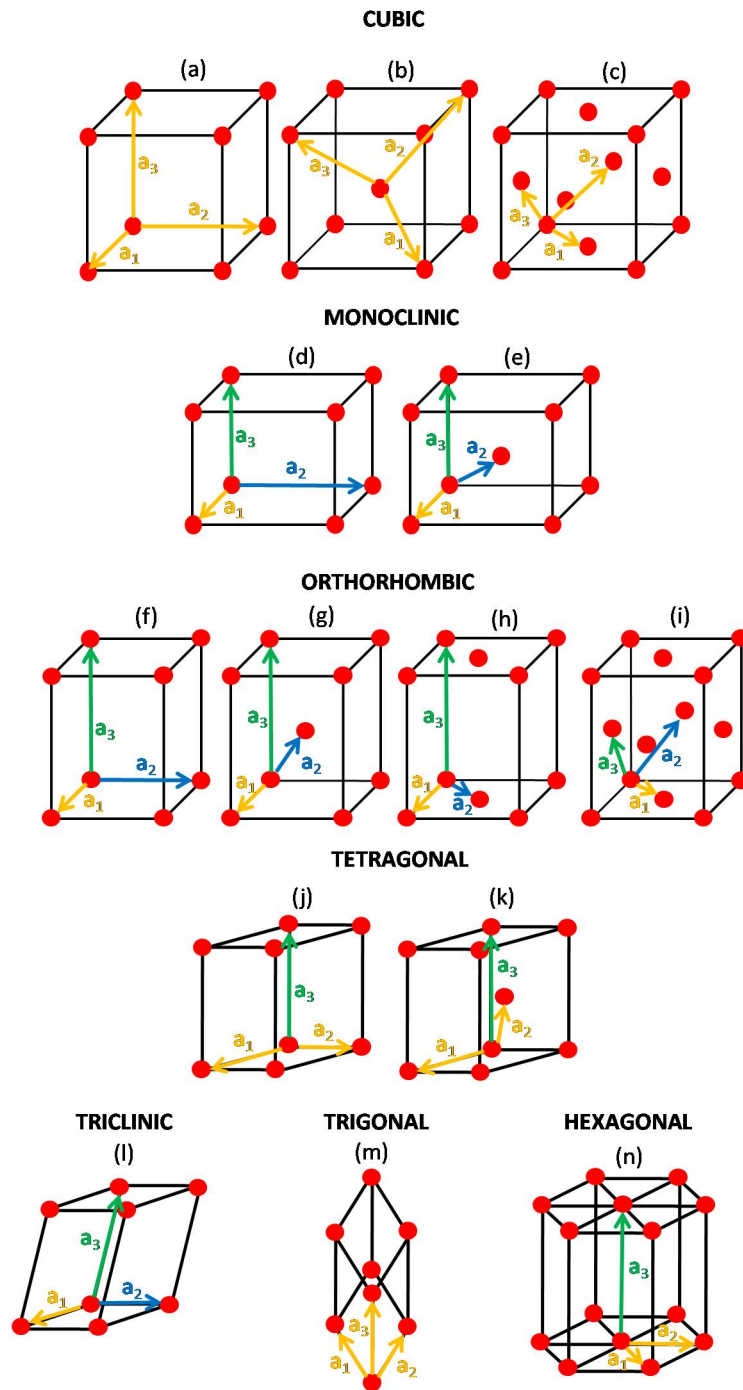
Figure 2.2: Bravais lattices in three-dimensions. The vector a_i and angle α_{ij} are in: (a) simple cubic, (b) body centered cubic and (c) faced centered cubic with $a_1 = a_2 = a_3$ and $\alpha_{12} = \alpha_{23} = \alpha_{31} = 90^o$; (d) simple monoclinic and (e) body centered monoclinic with $a_1 \neq a_2 \neq a_3$, $\alpha_{23} = \alpha_{31} = 90^o$ and $\alpha_{12} \neq 90^o$; (f) simple orthorhombic, (g) body centered orthorhombic, (h) base centered orthorhombic and (i) faced centered orthorhombic with $a_1 \neq a_2 \neq a_3$ and $\alpha_{12} = \alpha_{23} = \alpha_{31} = 90^o$; (j) simple tetragonal and (k) body centered tetragonal with $a_1 = a_2 \neq a_3$ and $\alpha_{12} = \alpha_{23} = \alpha_{31} = 90^o$; (l) triclinic with $a_1 \neq a_2 \neq a_3$ and $\alpha_{12} \neq \alpha_{23} \neq \alpha_{31}$; (m) trigonal with $a_1 = a_2 = a_3$ and $\alpha_{12} = \alpha_{23} = \alpha_{31} < 120^o$; and (n) hexagonal with $a_1 = a_2 \neq a_3$, $\alpha_{12} = 120^o$ and $\alpha_{23} = \alpha_{31} = 90^o$.
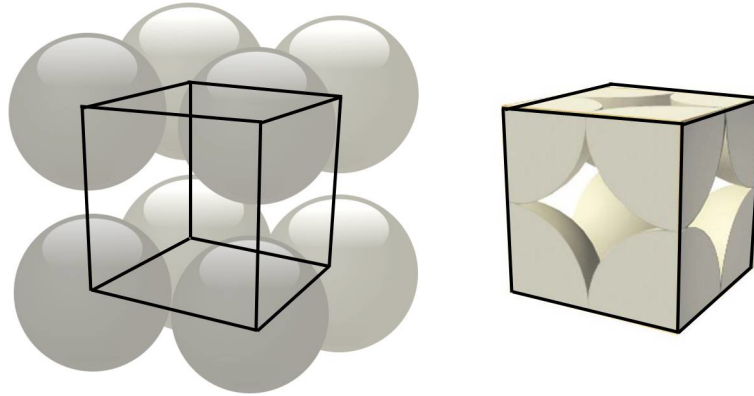
Figure 2.3: Scheme illustrating a unit cell containing just one atom.

In a crystal, it is important to know its crystal planes, defined by the atoms constituting the lattice. In semiconductor physics, knowing the crystal planes is crucial because depending on the plane the bulk substrate is cut and the samples are grown, one may obtain different properties and results of the growth process. In Fig. 2.4, we show possible planes obtained from the bulk structure cut along different directions. The planes are usually named by the Miller indices [2] [hkl] that indicate the direction of the normal vector to the in the basis of the corresponding reciprocal lattice.
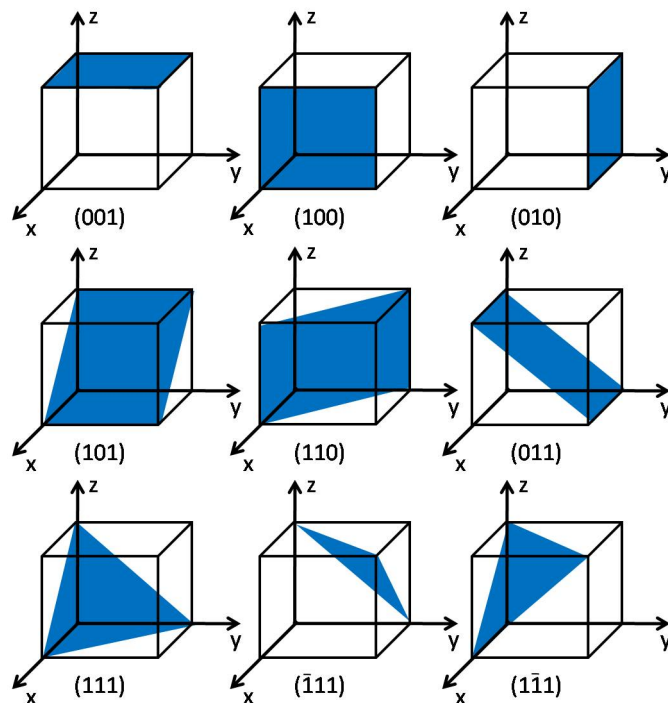
Figure 2.4: Miller indices of some important planes in a cubic crystal.

Crystals are usually classified by their conductivity/resistivity. Thus the crystals can be basically insulating, conductors or semiconductors. In this classification, semiconductors have elec-

trical resistivity at room temperature with values in the range of 10^{-2} to 10^9 ohm-cm, strongly dependent on temperature. At absolute zero, a pure perfect crystal of most semiconductors will be an insulator, if we arbitrarily define an insulator as having a resistivity above 10^{14} ohm-cm. Devices based on semiconductors include transistors, switches, diodes, photovoltaic cells, detectors, and thermistors. These may be used as single circuit elements or as components of integrated circuits.

A highly purified semiconductor exhibits intrinsic conductivity, as distinguished from the impurity conductivity of less pure specimens. In the intrinsic temperature range, the electrical properties of a semiconductor are not essentially modified by impurities in the crystal. The conduction band is void at absolute zero and is separated by an energy gap E_g from the filled valence band. The band gap is the energy difference between the lowest state of the conduction band and the highest state of the valence band. The lowest point in the conduction band is called the conduction band edge and the highest point in the valence band is called the valence band edge.

As the temperature is increased, electrons are thermally excited from the valence band to the conduction band. Both the electrons in the conduction band and the vacant state or holes left behind in the valence band contribute to the electrical conductivity [2]. The intrinsic conductivity and intrinsic carrier concentrations are largely controlled by E_g/k_BT, the ratio of the band gap to the temperature T, with k_B being the Boltzmann constant [3]. When this ratio is large, the concentration of intrinsic carriers will be low and also the conductivity.

The value of the band gap may be obtained from the temperature dependence of the conductivity or of the carrier concentration in the intrinsic range. The carrier concentration is obtained from measurements of the Hall voltage [4], sometimes complemented by conductivity measurements. Optical measurements determine whether the gap is direct or indirect. Germanium (Ge) and silicon (Si) are examples whose the band edges are connected by indirect optical transitions (Fig. 2.5(a)), while in indium antimonide (InSb) and gallium arsenide (GaAs) the band edges are connected by a direct transition (Fig. 2.5(b)). Here, we studied GaAs, indium gallium arsenide (InGaAs) and (InGaAsN) structures, all direct gap systems.

In the direct absorption process, as illustrated in Fig. 2.5(b), a photon is absorbed by with the creation of an electron in the conduction band and a hole, in the valence band. On the other hand, in the indirect absorption process, illustrated in Fig. 2.5(a), the minimum energy gap of the band structure corresponds to electrons and holes separated by a substantial wavevector $\mathbf{k}_c$.
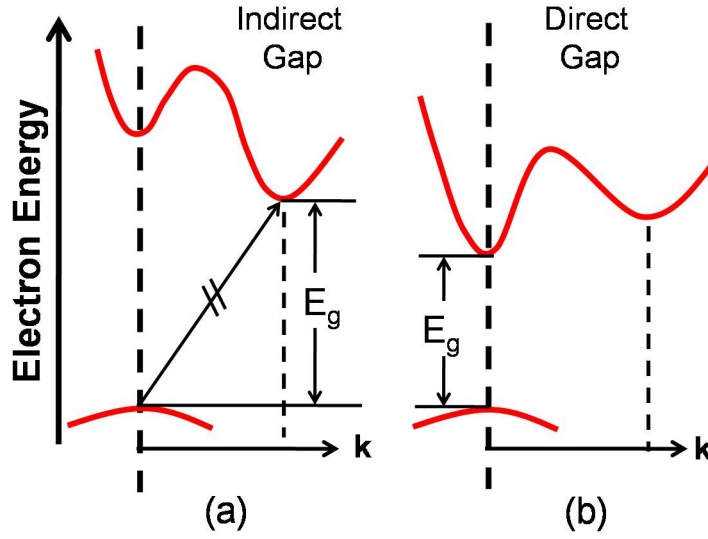
Figure 2.5: Transition between valence band and conduction band. (a) Indirect transition and (b) direct transition.

Here a direct photon transition at the energy of the minimum gap cannot satisfy the requirement of conservation of the wavevector, because photon wavevectors are negligible at the energy range of interest.

2.2 Effective mass approach and envelope function

The approach used in this thesis to calculate the band structures is based on the idea that one electron moving in the atomic lattice, under a periodic potential, can be treated through the effective mass concept, μ^* [5]. This approach is described within the **k.p** method, based on the perturbation theory. In this method various parameters are used such as: band gap, split-off energy, inter conduction and valence band coupling elements, etc. These parameters can be determined precisely by optical and magneto-optical experiments, or from first principle calculations, what makes the method a versatile tool. Another advantage of the **k.p** method is the use of a small basis with important applications in simulations of optical, magnetic and transport properties of semiconductors. According to the electronic states to be characterized, different approximations can be applied to this formalism. In particular, we shall use two: the parabolic approximation for the conduction band and the Luttinger model for the valence band.

The **k.p** method allows the electronic structure calculation close to the Γ point (**k** = 0) of the reciprocal lattice (states participating in the optical recombination). Basically, the effective band structure calculation is divided in three steps: (i) transformation of the crystal Hamiltonian

into the **k.p** representation; (ii) reduction of the problem to an eigenvalues matrix; and (iii) introduction of approximations.

To execute these steps, we start from the Schrodinger equation

$$\mathbf{H_0}\Psi_k(\mathbf{r}) = E_k\Psi_k(\mathbf{r}), \tag{2.2}$$

where

$$\mathbf{H_0} = \frac{\mathbf{P}^2}{2m_0} + V(\mathbf{r}), \tag{2.3}$$

$\mathbf{P} = -i\hbar\nabla$ is the linear momentum operator and m_0 is the mass of a free electron.

According to the Bloch theorem, the carrier movement characterization can be restricted to the first Brillouin zone [2]. The solutions of the Schrodinger equation (2.2) for one electron in a crystal is given by "envelope function"

$$\Psi_k(\mathbf{r}) = e^{i\mathbf{k}\cdot\mathbf{r}}u_k(\mathbf{r}) \tag{2.4}$$

where $u_k(\mathbf{r})$ is a function with the same spatial periodicity of the crystalline lattice [6].

Writing the operator $\mathbf{H_0}$ in terms of the wave vector **k**, we have

$$H(\mathbf{k}) = e^{-i\mathbf{k}\cdot\mathbf{r}}\mathbf{H_0}e^{i\mathbf{k}\cdot\mathbf{r}}, \tag{2.5}$$

and expanding the exponentials in Taylor series

$$H(\mathbf{k}) = H_0 - i\mathbf{k}.[\mathbf{r}, \mathbf{H_o}] - \frac{1}{2}\sum_{ij}k_ik_j[r_i, [r_j, H_0]] + ... \tag{2.6}$$

wherein the commutator $[\mathbf{r}, H_0] = i\hbar\mathbf{P}/m_0$ and $[\mathbf{r}, [\mathbf{r}, H_0]] = -\hbar^2\delta_{ij}/m_0$, results in

$$H(\mathbf{k}) = \frac{\mathbf{P}^2}{2m_0} + V(\mathbf{r}) + \frac{\hbar^2k^2}{2m_0} + \frac{\hbar}{m_0}\mathbf{k}.\mathbf{P}. \tag{2.7}$$

Applying (2.7) and (2.4) in Eq. (2.2), we get:

$$\left[\frac{\mathbf{P}^2}{2m_0} + V(\mathbf{r}) + \frac{\hbar^2k^2}{2m_0} + \frac{\hbar}{m_0}\mathbf{k}.\mathbf{P}\right]u_{n\mathbf{k}} = \mathscr{E}_{n\mathbf{k}}u_{n\mathbf{k}}, \tag{2.8}$$

where **k** is the wave vector, the potential $V(\mathbf{r})$ is the potential in which the electron moves, $\mathscr{E}_{n\mathbf{k}}$ is the carrier energy for certain wave vector **k**, and n indicates possible bands. At the high

symmetry point Γ, the terms that depend on $\mathbf{k}$ in Eq. (2.8) vanish. Thus, it is possible to assume a solution for this equation in $\mathbf{k} \approx 0$ given by

$$u_{n\mathbf{k}} = \sum_m C_{m\mathbf{k}} u_{m\mathbf{0}}. \tag{2.9}$$

Inserting the solution (2.9) in Eq. (2.8), multiplying by, $u_{m0}*$, and using orthogonality, we have

$$\sum_m \left[\left(\mathscr{E}_{n0} - \mathscr{E}_{n\mathbf{k}} + \frac{\hbar^2 \mathbf{k}^2}{2m_0} \right) \delta_{nm} + \frac{\hbar \mathbf{k}}{2m_0} \cdot \langle n0|\mathbf{P}|m0 \rangle \right] C_{m\mathbf{k}} = 0. \tag{2.10}$$

The diagonalization of the Eq. (2.10) results in the dispersion relation $\mathscr{E}_{n\mathbf{k}}$ and in the expansion coefficients $C_{m\mathbf{k}}$ for all the values of $\mathbf{k}$ and all bands n.

Suppose that the n-th band with $\mathscr{E}_{n0}$ energy is not degenerated and assume small values of $\mathbf{k}$. This allows to use the perturbation theory to get

$$C_n \sim 1; \ C_m = \frac{\hbar \mathbf{k}}{2m_0} \cdot \frac{\mathbf{P}_{nm}}{\mathscr{E}_{n0} - \mathscr{E}_{m0}}, \tag{2.11}$$

that, replaced in Eq. (2.10), gives a second order correction in $\mathscr{E}_{n0}$ energy,

$$\mathscr{E}_{n\mathbf{k}} = \mathscr{E}_{n0} + \frac{\hbar^2 k^2}{2m_0} + \frac{\hbar^2}{m_0^2} \sum_{m \neq n} \frac{|\mathbf{P}_{nm} \cdot \mathbf{k}|^2}{\mathscr{E}_{n0} - \mathscr{E}_{m0}}. \tag{2.12}$$

When $\mathbf{k}$ is small, the dispersion relation of the degenerated bands is parabolic around Γ point

$$\mathscr{E}_{n\mathbf{k}} = \mathscr{E}_{n0} + \frac{\hbar^2}{2} \sum_{i,j} k_i \frac{1}{\mu_n^{ij(*)}} k_j, \tag{2.13}$$

in which the i, j indexes refer to x, y, z and $\mu_n^{ij(*)}$ to the effective mass tensor, defined as [6]

$$\frac{1}{\mu_n^{ij(*)}} = \frac{1}{m_0} \delta_{ij} + \frac{2}{m_0^2} \sum_{n \neq m} \frac{P_{nm}^i P_{nm}^j}{\mathscr{E}_{n0} - \mathscr{E}_{m0}}. \tag{2.14}$$

In Eq. (2.14), the effective mass of the carrier is determined by the coupling effect with other bands. Among remote bands, in general only one or a set of bands (degenerated) have the stronger coupling. For a semiconductor of direct gap, the valence band coupling is dominant. If we neglect the other bands coupling, the sum in Eq. (2.12) has only one term for which the denominator is the band gap. When the gap is small, the effective mass is small too. This is the reason for a small effective electron mass in semiconductors of narrow gap.

The effective mass tensor (Eq. 2.14) takes into account only the kinetic term of the Hamiltonian and the periodic potential of the crystalline lattice. However, if we include the SO interaction [7]

$$H_{SO} = \frac{\hbar}{4m_0^2 c^2} \sigma \cdot \mathbf{p} \times (\nabla V), \qquad (2.15)$$

in Eq. (2.3) the lattice periodic parts of the Bloch functions become two-component spinors $|n\mathbf{k}\rangle$ and the Schrodinger equation (2.8) reads

$$\left[\frac{p^2}{2m_0} + V(\mathbf{r}) + \frac{\hbar^2 k^2}{2m_0} + \frac{\hbar}{m_0} \mathbf{k} \cdot \mathbf{p} + \frac{\hbar}{4m_0^2 c^2} (\sigma \times \nabla V) \cdot (\hbar \mathbf{k} + \mathbf{p}) \right] |n\mathbf{k}\rangle = \mathscr{E}_{n\mathbf{k}} |n\mathbf{k}\rangle, \qquad (2.16)$$

where $\sigma = (\sigma_x, \sigma_y, \sigma_z)$ is the vector of Pauli spin matrices and c is the speed of light.

With the notation

$$\pi = \mathbf{p} + \frac{\hbar}{4m_0 c^2} \sigma \times \nabla V, \qquad (2.17)$$

Eq. (2.16) becomes

$$\left[H_0 + H_{SO} + \frac{\hbar^2 k^2}{2m_0} + \frac{\hbar}{m_0} \mathbf{k} \cdot \pi \right] |n\mathbf{k}\rangle = \mathscr{E}_{n\mathbf{k}} |n\mathbf{k}\rangle. \qquad (2.18)$$

Note that in the presence of SO interaction the spin σ is not a good quantum number. We have only a common index n for the orbital motion and the spin degree of freedom, which classifies the bands according to the irreducible representations of the double group [6, 8]. The SO coupling has a very profound effect on the energy band structure. For example, it gives rise to the splitting of the topmost valence band. Spin degeneracy of electron and hole states in a semiconductor is the combined effect of inversion symmetry in space and time [2]. Both symmetry operations change the wave vector $\mathbf{k}$ into $-\mathbf{k}$, but time inversion also flips the spin, so that when we combine both we have a twofold degeneracy of the single-particle energies, $E_{+\mathbf{k}}$ and $E_{-\mathbf{k}}$. When the potential through which the carriers move is inversion-asymmetric, the spin degeneracy is removed even in the absence of an external magnetic field B. We then obtain two branches of the energy dispersion, $E_{+\mathbf{k}}$ and $E_{-\mathbf{k}}$. In heterostructures, the spin splitting can be the consequence of a bulk inversion asymmetry (BIA) of the underlying crystal, and of a structure inversion asymmetry (SIA) of the confinement potential [9, 10]. Since the SIA term is dominant over the BIA term in confined systems as QWs, QDs, and QRs, we neglected the BIA contribution, and keep the focus on SIA effects.

The SIA spin splitting in the conduction band Γ_6 is given by the Rashba term [10, 11],

$$H_{SIA} = \alpha_s \boldsymbol{\sigma} \cdot (\nabla V \times \mathbf{k}), \tag{2.19}$$

with a material-specific prefactor α_s [12, 13], and both ∇ and $\mathbf{k}$ polar vector as shown in Appendix A. Likewise, the vector of Pauli spin matrices is an axial vector. We see in Ref. [7] that the scalar triple product in Eq. (2.19) is the only term of first order in ∇ and $\mathbf{k}$ that is compatible with the symmetry of the bands.

The Rashba model (Eq. 2.19) for SIA spin splitting of electron systems is well established in the literature. For hole systems, on the other hand, the situation is more complex because of the fourfold degeneracy of the topmost valence band Γ_8. As our objective is the analysis of the SO effects in QR conduction band in the presence of magnetic fields, as will be discussed in chapter 5, we have neglected the SO effects in the valence band. The details about the SIA calculations for conduction band are presented in the Appendix A. However, in the presence of a tilted magnetic field, an additional term comes out. The calculations to get the SO additional term due to tilted magnetic field is presented in Appendix B. This configuration was used in chapter 5 for QRs systems, whose Hamiltonian is also detailed in Appendix B.

The most basic model to calculate band structure of a semiconductor is the parabolic model. In this case, we assume the effective mass tensor as isotropic rewriting the Eq. (2.13) as

$$\mathscr{E}_c(\mathbf{k}) = E_g + \frac{\hbar^2 k^2}{2\mu_e^*}, \tag{2.20}$$

for conduction band, and

$$\mathscr{E}_v(\mathbf{k}) = -\frac{\hbar^2 k^2}{2\mu_h^*}, \tag{2.21}$$

for valence band, where $\mu_{e/h}^*$ are the conduction (electron) and valence (hole) band effective masses [7].

For the conduction band, this approximation can proceed and was used for our electronic structure calculations. However, the valence band effective mass tensor in semiconductor materials has an anisotropic character and this approximation can not be adopted. For this reason, we had to use more complex approximations, considering the non parabolicity effects, anisotropy, and coupling among light holes (LHs) and heavy holes (HHs).

As introduced previously, the electronic structure description is based on the Bloch theorem and is applicable to volumetric systems (bulk). But, it can be extended to nanoscopic ones, such

as QWs, QWrs, QDs and QRs, where the crystalline properties still remain. In this case the envelope function approximation is used [6] and Eq. (2.10), for a potential, $V(\mathbf{r})$, with smooth variation in the crystal unit cell scale, becomes

$$\sum_m \left[\left(\mathscr{E}_{n0} - \mathscr{E}_{n\mathbf{k}} + \frac{\hbar^2 \mathbf{k}^2}{2m_0} + V(\mathbf{r}) \right) \delta_{nm} + \frac{\hbar \mathbf{k}}{2m_0} \cdot \langle n0|\mathbf{P}|m0\rangle \right] C_{m\mathbf{k}} = 0. \qquad (2.22)$$

Proceeding analogously as for Eqs. (2.20) and (2.21), we have

$$H_c = E_g + \frac{\hbar^2 k^2}{2\mu_e^*} + V(\mathbf{r}). \qquad (2.23)$$

for the conduction band. Changing $\mathbf{k}$ (before a number), for the operator $-i\nabla$, the effective Hamiltonian is written as

$$H_c = E_g - \frac{\hbar^2 \nabla^2}{2\mu_e^*} + V(\mathbf{r}). \qquad (2.24)$$

In the presence of a magnetic field, $\mathbf{B}$, the operator $\widehat{P} = -i\hbar\nabla$, should be replaced by $(\mathbf{P} + e\mathbf{A}/c)$ where e is the electron charge, and $\mathbf{A}$ is the vector potential, such that $\mathbf{B} = \nabla \times \mathbf{A}$. Besides, we should include the Zeeman contribution for the system, that results in

$$H_c = E_g + \frac{1}{2\mu_e^*} \left(\mathbf{P} + \frac{e}{c}\mathbf{A} \right)^2 + V(\mathbf{r}) + \frac{1}{2} g\mu_B \vec{B} \cdot \vec{\sigma}, \qquad (2.25)$$

where g is Lande g-factor and μ_B the Bohr magneton.

The symmetry of a given problem defines the best way to write the operator $\mathbf{P}$. In case of cylindrical systems, such as QDs and QRs, the problem is easily solved in cylindrical coordinates, so $\mathbf{P} = \mathbf{P}_{r\varphi} + \mathbf{P}_z$, where

$$\mathbf{P}_{r\varphi} = -i\hbar \left[\widehat{r}\frac{\partial}{\partial r} + \widehat{\varphi}\frac{1}{r}\frac{\partial}{\partial \varphi} \right] \qquad (2.26)$$

and

$$\mathbf{P}_z = -i\hbar\partial/\partial z. \qquad (2.27)$$

2.3   K.P Method and Luttinger hamiltonian

For direct gap semiconductors, the carriers (electrons and holes) occupying states close to the band edges are the most important for electronic and optical studies. In our approximation,

we take into account the interaction among bands, non parabolicity effects and spin effects, that are essential to get the electronic properties of semiconductor nanostructures. Among the analogue matrix methods, the simplest Kane model [14, 15] results in a 8x8 Hamiltonian, that should always be used when studying materials whose energy gap does not allow neglecting the interaction of conduction (Γ_6), valence (Γ_8) and split-off (Γ_7) bands. However, there are others useful approximations when some inter band coupling can be neglected: For uncoupled conduction and valence band, we use 6x6 Luttinger-Kohn Hamiltonian, while for separated valence band description, we use a 4x4 Luttinger Hamiltonian. This last model is used when the energetic separation between valence band and split-off is large enough to uncouple these bands, as in InGaAs and GaAs.

In this section we introduce the Luttinger model [16], based on **k.p** method. The objective is to build a simple and efficient model to calculate the valence band of semiconductors QDs and QRs. The solution obtained in Eq. (2.10) provides the exact energy bands calculation in any point of the Brillouin zone, however the region of interest in this work, as already stated, is around Γ point. Using the method developed by Löwdin [17], that treats the problem via perturbation theory and exact diagonalization, Luttinger got his Hamiltonian (H_L) taking into account only symmetry aspects for valence band calculation [18].

The Luttinger Hamiltonian matrix depends on the plane direction. Here, we are interesting on the direction [001]. This direction is the same as one our experimental collaborators grew their QWs, QDs and QRs samples. The representation of the Hamiltonian for direction [001] is the 4x4 matrix operator

$$H_L^{ij} = H_K^{ij} + V(\mathbf{r})\delta_{ij} \tag{2.28}$$

where H_K is the kinetic energy of holes, given by Luttinger in axial approximation [16]. This Hamiltonian describes the valence band dispersion Γ_8 and includes an applied magnetic field in z direction. The confinement potential $V(\mathbf{r})$ is added in the diagonal elements of the HH and LH matrix H_K.

The Hamiltonian H_K can be represented in a combination of eigenstates of the angular momentum 3/2,

$$\left|\frac{3}{2},\frac{3}{2}\right\rangle = \frac{1}{2}\left|(X+iY)\uparrow\right\rangle \tag{2.29}$$

$$\left|\frac{3}{2},\frac{1}{2}\right\rangle = \frac{i}{\sqrt{6}}\left|(X+iY)\downarrow\right\rangle - 2\left|Z\uparrow\right\rangle \tag{2.30}$$

$$\left|\frac{3}{2}, -\frac{1}{2}\right\rangle = \frac{1}{\sqrt{6}} |(X - iY) \uparrow\rangle + 2 |Z \downarrow\rangle \tag{2.31}$$

$$\left|\frac{3}{2}, -\frac{3}{2}\right\rangle = \frac{i}{2} |(X - iY) \downarrow\rangle \tag{2.32}$$

and is written as,

$$H_K = \begin{pmatrix} a_+^{hh\uparrow} & b_- & c_- & 0 \\ b_+ & a_-^{lh\uparrow} & 0 & c_- \\ c_+ & 0 & d_-^{lh\downarrow} & b_- \\ 0 & c_+ & b_+ & d_+^{hh\downarrow} \end{pmatrix}. \tag{2.33}$$

In this symbology, the arrows represent the spins up ($\uparrow$) and down ($\downarrow$), and the matrix elements are expressed as

$$\begin{aligned} a_\pm &= -\frac{\hbar^2}{2m_0}(\gamma_1 \mp 2\gamma_2)k_z^2 - \frac{\hbar^2}{4m_0}(\gamma_1 \pm \gamma_2)(k_+k_- + k_-k_+) \\ &\quad + \frac{(2 \pm 1)}{2}\hbar\omega_e \left(\kappa + \frac{(5 \pm 4)}{4}q\right), \end{aligned} \tag{2.34}$$

$$d_\pm = a_\pm - \frac{(2 \pm 1)}{2}\hbar\omega_e \left(\kappa + \frac{(5 \pm 4)}{4}q\right), \tag{2.35}$$

$$b_\mp = \hbar^2 \frac{\sqrt{3}}{4m_0}\gamma_3 k_z k_\mp, \tag{2.36}$$

$$c_\mp = \hbar^2 \frac{\sqrt{3}}{4m_0}(\gamma_2 + \gamma_3)k_\mp^2 \tag{2.37}$$

where the cyclotron frequency ω_e is given by $\omega_e = \frac{eB}{m_0}$ and the letters q, κ and γ_α ($\alpha = 1, 2, 3$) are called Luttinger parameters, determined by first-principle calculations, that define HH and LH effective masses in the ordinary way:

$$\mu_{hh}^z = m_0/(\gamma_1 - 2\gamma_2), \tag{2.38}$$

$$\mu_{lh}^z = m_0/(\gamma_1 + 2\gamma_2), \tag{2.39}$$

$$\mu_{hh}^{xy} = m_0/(\gamma_1 + \gamma_2) \tag{2.40}$$

and

$$\mu_{lh}^{xy} = m_0/(\gamma_1 - \gamma_2). \tag{2.41}$$

The parameters q and κ produce the Zeeman contribution, while γ_α are defined by Kane [19,20]

from (L', M, N'), as

$$\gamma_1 = -\frac{2m_0}{3\hbar^2}(L' + 2M) - 1 \tag{2.42}$$

$$\gamma_2 = -\frac{m_0}{3\hbar^2}(L' - M) \tag{2.43}$$

$$\gamma_3 = -\frac{m_0}{3\hbar^2}N' \tag{2.44}$$

where

$$L' = F' + 2G; \tag{2.45}$$

$$M = H_1 + H_2; \tag{2.46}$$

$$N' = F' - G + H_1 - H_2, \tag{2.47}$$

with

$$G = \frac{\hbar^2}{2m_0^2}\sum_{ij}\frac{|\langle x|p_x|n\Gamma_3 j\rangle|^2}{E_v - E_{n,\Gamma_3}}; \tag{2.48}$$

$$F' = \frac{\hbar^2}{m_0^2}\sum_{ij}\frac{|\langle x|p_x|n\Gamma_1 j\rangle|^2}{E_v - E_{n,\Gamma_1}}; \tag{2.49}$$

$$H_1 = \frac{\hbar^2}{2m_0^2}\sum_{ij}\frac{|\langle x|p_x|n\Gamma_5 j\rangle|^2}{E_v - E_{n,\Gamma_5}}; \tag{2.50}$$

$$H_2 = \frac{\hbar^2}{2m_0^2}\sum_{ij}\frac{|\langle x|p_x|n\Gamma_4 j\rangle|^2}{E_v - E_{n,\Gamma_4}}. \tag{2.51}$$

These terms can be calculated from first principles or the parameters can also be extracted experimentally through effective mass analysis.

The operators $\mathbf{k}$ may be written in polar coordinates from Eqs. (2.26) and (2.27),

$$\mathbf{k}_{\mp} = -ie^{\mp i\varphi}\left(\frac{\partial}{\partial r} \mp \frac{i}{r}\frac{\partial}{\partial \varphi} \pm \frac{m_0\omega_e}{2\hbar}r\right), \tag{2.52}$$

and

$$\mathbf{k}_z = -i\frac{\partial}{\partial z}. \tag{2.53}$$

Combining the Hamiltonian H_K with potential $V(\mathbf{r})$, we obtain the Luttinger Hamiltonian

H_L of Eq. (2.28),

$$H_L = \begin{pmatrix} a_+^{hh\uparrow} + V(\mathbf{r}) & b_- & c_- & 0 \\ b_+ & a_-^{lh\uparrow} + V(\mathbf{r}) & 0 & c_- \\ c_+ & 0 & d_-^{lh\downarrow} + V(\mathbf{r}) & b_- \\ 0 & c_+ & b_+ & d_+^{hh\downarrow} + V(\mathbf{r}) \end{pmatrix}. \tag{2.54}$$

This Hamiltonian is used for valence band calculations with unstrained structures. For strained ones we need to modify the Hamiltonian H_L as shown below.

2.3.1 Strain Effects

It is already known that the strain is the main factor that controls both QD and QR growth. This strain is produced by the mismatch between lattice parameters of the surfaces. Besides, the presence of strain affects the electronic properties resulting in energy bands changes. Therefore we must consider its effects in our calculations.

When stress is applied in a semiconductor, the crystal deformation results in energy shifts [21–23]. Application of stress in a crystal decreases the crystalline potential symmetry, $V(\mathbf{r})$, making impossible the expansion of perturbed system [23] in the old representation. However, we can introduce a deformed coordinates system,

$$r'_i = \sum_j (\delta_{ij} - \varepsilon_{ij}) r_j, \tag{2.55}$$

implying

$$p'_i = \sum_j (\delta_{ij} + \varepsilon_{ij}) p_j, \tag{2.56}$$

$$k'_i = \sum_j (\delta_{ij} + \varepsilon_{ij}) k_j. \tag{2.57}$$

Here ε denotes the strain tensor. The Bravais lattice of a crystal under strain in the new coordinates system matches to a crystal without strain in the old coordinates system.

Going back to the old notation and doing the modification $r' \to r$, the deformed crystal potential, $V_\varepsilon[(1+\varepsilon)r]$ has the same periodicity of the unperturbed potential $V(\mathbf{r})$. Therefore,

we can expand $V_\varepsilon(r)$ in series of ε,

$$V_\varepsilon[(1+\varepsilon)r] = V(\mathbf{r}) + \sum_{ij} V_{ij}(r)\varepsilon_{ij} + ..., \qquad (2.58)$$

where

$$V_{ij} = \frac{1}{2-\delta_{ij}} \lim_{\varepsilon \to 0} \frac{V_\varepsilon[(1+\varepsilon)r] - V(\mathbf{r})}{\varepsilon_{ij}}. \qquad (2.59)$$

Restricting ourselves to linear terms of strain, we get, instead Eq. (2.8), an expression given by

$$\left[\frac{\mathbf{P}^2}{2m_0} + V(\mathbf{r}) + \frac{\hbar^2 k^2}{2m_0} + \frac{\hbar}{m_0}\mathbf{k}.\mathbf{P} + \sum_{ij} \left(-\frac{\mathbf{P}_i\mathbf{P}_j}{m_0} + V_{ij} \right) \varepsilon_{ij} \right.$$
$$\left. -\frac{\hbar^2}{m_0}\mathbf{k}\varepsilon\mathbf{k} - \frac{2\hbar}{m_0}\mathbf{k}\varepsilon\mathbf{P} \right] u_{n\mathbf{k}} = \mathscr{E}_{n\mathbf{k}}u_{n\mathbf{k}}. \qquad (2.60)$$

Solving Eq. (2.60) analogously to Eq. (2.8), we have a similar expression to Eqs. (2.20) and (2.21), yet including the term responsible to the strain shift. The important matrix elements, proportional to ε are

$$v_{ij_{\sigma\sigma'}^{\nu\nu'}} = \left\langle \nu\sigma \left| -\frac{\mathbf{P}_i\mathbf{P}_j}{m_0} + V_{ij} \right| \nu'\sigma' \right\rangle, \qquad (2.61)$$

called deformation potentials [7].

The connection between stress and strain was identified by Robert Hooke [24] and can be given by the linear relation,

$$\tau_{ij} = c_{ijkl}\varepsilon_{ij} \qquad (2.62)$$

where c_{ijkl} is the fourth order elastic stiffness tensor with 81 coefficients, but depending on the crystal symmetry, the number of coefficients can be reduced. For instance, for crystals with cubic symmetry, like zinc blende, such as InAs and GaAs, the non vanishing coefficients are only three: c_{11}, c_{12} and c_{44}. These coefficients are known as elastic stiffness constants. The generalization of the Hooke law, for crystals with cubic symmetry, in matrix form, can be

written as [25]

$$
\begin{pmatrix} \tau_{11} \\ \tau_{22} \\ \tau_{33} \\ \tau_{23} \\ \tau_{31} \\ \tau_{12} \end{pmatrix} = \begin{pmatrix} c_{11} & c_{12} & c_{12} & 0 & 0 & 0 \\ c_{12} & c_{11} & c_{12} & 0 & 0 & 0 \\ c_{12} & c_{12} & c_{11} & 0 & 0 & 0 \\ 0 & 0 & 0 & c_{44} & 0 & 0 \\ 0 & 0 & 0 & 0 & c_{44} & 0 \\ 0 & 0 & 0 & 0 & 0 & c_{44} \end{pmatrix} \times \begin{pmatrix} \varepsilon_{11} \\ \varepsilon_{22} \\ \varepsilon_{33} \\ 2\varepsilon_{23} \\ 2\varepsilon_{31} \\ 2\varepsilon_{12} \end{pmatrix}.
\tag{2.63}
$$

For a system with axial symmetry where the symmetry axis is along z (3 in the previous notation) direction (along crystallographic direction [001] in our case), the strain components are given by,

$$
\varepsilon_{11} = \varepsilon_{22} = \varepsilon_{\parallel}, \quad \varepsilon_{\perp} = \varepsilon_{33}.
\tag{2.64}
$$

In the absence of external uniaxial stress (along z), where $\tau_{33} = 0$, and according to Eq. (2.63), we can get the relation between different components,

$$
\varepsilon_{\perp} = -\frac{2c_{12}}{c_{11}}\varepsilon_{\parallel}.
\tag{2.65}
$$

The variation of parallel $\varepsilon_{\parallel}$ and perpendicular $\varepsilon_{\perp}$ strain components are responsible for the deformation in-plane and along z axis, respectively. Thus, when the component $\varepsilon_{\parallel}$ is positive, $\varepsilon_{\perp}$ is negative; so compressing one direction expands the other. The Bir-Pikus Hamiltonian [23] is

$$
H_L^D = \begin{pmatrix} a_+^{hh\uparrow} + \Delta E_{hh} & b_- & c_- & 0 \\ b_+ & a_-^{lh\uparrow} + \Delta E_{lh} & 0 & c_- \\ c_+ & 0 & d_-^{lh\downarrow} + \Delta E_{lh} & b_- \\ 0 & c_+ & b_+ & d_+^{hh\downarrow} + \Delta E_{hh} \end{pmatrix} + V(\mathbf{r})\delta_{ij},
\tag{2.66}
$$

with

$$
\Delta E_{hh} = -(P+Q) = -\frac{1}{2}\left[\beta_1(2\varepsilon_{\parallel} + \varepsilon_{\perp})\right] - \beta_2\varepsilon_{\parallel\perp}
\tag{2.67}
$$

for HH subband, and

$$
\Delta E_{lh} = -(P-Q) = -\frac{1}{2}\left[\beta_1(2\varepsilon_{\parallel} + \varepsilon_{\perp})\right] + \beta_2\varepsilon_{\parallel\perp}
\tag{2.68}
$$

for LH subband. Besides $\beta_1 = -2a_v$ and $\beta_2 = b$, where a_v and b are defined by the material compositions.

2.4 QW and QD/QR Models

Another important factor relative to the subbands position is the anisotropic confinement. For electronic structure description it is important to know the details about the morphology of the system. These details are given experimentally through structural characterization techniques such as atomic force microscopy (AFM). The theoretical models used here are based in structural data obtained by our experimental collaborators that characterized the systems.

The 3D structures studied in this thesis allow the separation of their confinement in a radial (xy) confinement and a (z) confinement. Thus. in this section, we present the systems, the models to emulate the potential confinements, and some important properties that depend on confinement shape and composition. We know that the composition changes the energy gap, shifting the levels [26, 27], while the confinement modifies completely the energy behavior [28]. The models used in this thesis can be basically applied to QWs, QDs, QRs systems and combinations of them.

2.4.1 QW Model

The confinement in z direction, used to simulate a QW and z confinement in QD and QR, is given by a rigid wall, with a potential profile given by

$$V(z) = \begin{cases} eFz, & 0 < z \leq L \\ \infty, & \text{otherwise.} \end{cases} \tag{2.69}$$

For $F = 0$, the wave function for a rigid wall is given by

$$\chi_l^{(e/h)}(z) = \sqrt{\frac{2}{L}} \sin\left(\frac{l\pi z}{L} + \frac{l\pi}{2}\right), \tag{2.70}$$

with $l = 1, 2, ...$ and F an external electric field applied along the growth axis. The corresponding eigenenergies are

$$E_l^{(e/h)} = \left(\frac{l^2 \pi^2 \hbar^2}{2\mu_{(e/h)}^* L^2}\right), \tag{2.71}$$

24

where L is the height/thickness of the QW.

2.4.2 QD and QR model

The calculation of the spectrum in the QD and QR utilizes the full diagonalization of the Hamiltonian written in the basis that considers a sufficiently large Hilbert space, truncated to the desired accuracy. We typically consider 11 eigenstates, with angular momentum $|m| < 5$ for each spin orientation. These are found sufficient for convergence in the entire field and parameter range considered in this work [29].

The choice of the model used to emulate the in-plane confinement for a 0D structure was of great importance, since we want an expression as simple as possible to be adaptable for QDs and QRs. The in-plane confinement potential chosen, $V(\rho, \varphi)$, is characterized by [29, 30]

$$V(\rho, \varphi) = \frac{a_1}{\rho^2} + a_2 \rho^2 - 2\sqrt{a_1 a_2} \tag{2.72}$$

in cylindrical coordinates, while the vertical confinement is modeled by a rigid wall model as described in Eq. (2.69). The parameters a_1 and a_2 are used to define the effective confinement and structure shape. Eq. (2.72) is used to simulate a QR on the present form while for a QD we set $a_1 = 0$. Figs. 2.6(a) and 2.6(b) represent QD and QR potential profile, respectively, obtained by Eq. (2.72).
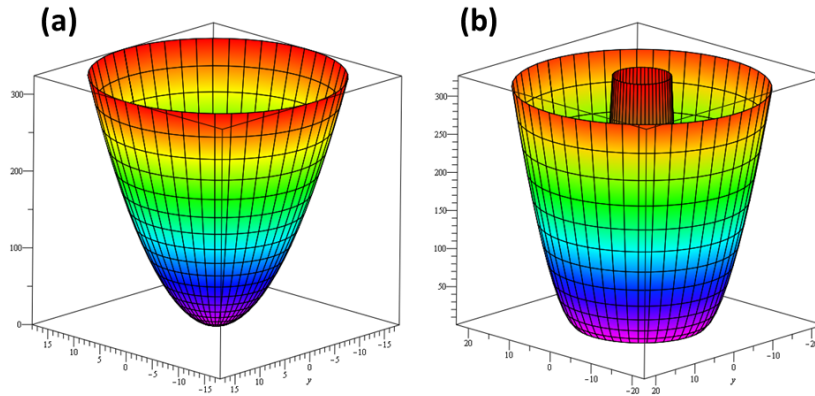
Figure 2.6: The potential profile for (a) QD and (b) QR.

The QR radius can be calculated as $R_{QR} = (a_1/a_2)^{1/4}$ and, once the ground state energy, E_0, is calculated, the effective width of the QR can be estimated as $\Delta r = \left(\frac{E_0}{a_2}\right)^{\frac{1}{2}}$. Fig. 2.7 shows a scheme indicating the radius and effective width of the QR. As we can see, R depends on a_1 and a_2 and Δr depends on a_2 and E_0 parameters. We can choose a_1 and a_2 in such a way that

R_{QR} remains unchanged while Δr becomes adjustable and vice-versa. For the estimation of Δr, E_0 is calculated for $B = 0\,T$, while the QD radius is estimate by $R_{QD} = h/(2\pi\sqrt{2a_2\mu^*})$.
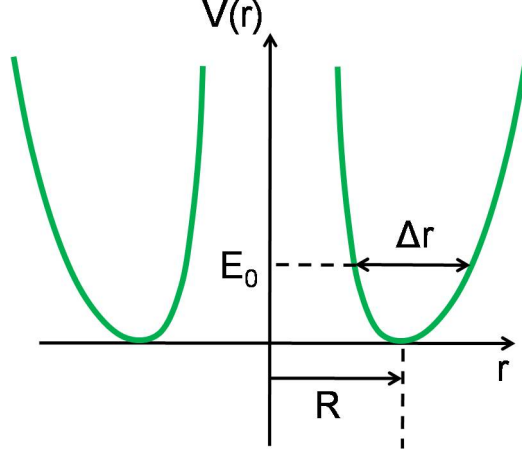
Figure 2.7: Scheme indicating radius R and effective width $\Delta(r)$ of the QR.

The solution for the 3D Schrödinger equation, $\Phi(\rho,\theta,z)$, corresponding to the potential profile in Eq. (2.72) can be found in Ref. [31] and has been used in Ref. [30] to describe the conduction band electronic structure of QRs under applied magnetic fields. The corresponding wavefunction, $\psi_{n,m,l}^{(e/h)}(\rho,\varphi,z)$, is given by

$$\psi_{n,m,l}^{(e/h)}(\rho,\varphi,z) = \phi_{n,m}^{(e/h)}(\rho,\varphi)\chi_l^{(e/h)}(z)u_{e/h}, \tag{2.73}$$

where $\chi_l^{(e/h)}(z)$ is the wave function for a rigid wall of the Eq. (2.70) and $u_{e/h} = |j,m_j\rangle$ are the basis functions at the zone center in the Kane model: $|1/2,\pm1/2\rangle$, $|3/2,\pm3/2\rangle$ and $|3/2,\pm1/2\rangle$, for electron, HH and LH states, respectively. The planar wave function has the form

$$\phi_{n,m}^{(e/h)}(\rho,\varphi) = \frac{1}{\lambda_{(e/h)}}\left(\frac{\Gamma[n+M_{(e/h)}+1]}{2^{M_{(e/h)}}n!(\Gamma[M_{(e/h)}+1])^2}\right)^{1/2}$$
$$\times\left(\frac{\rho}{\lambda_{(e/h)}}\right)^{M_{(e/h)}}\frac{e^{-im\varphi}}{\sqrt{2\pi}}e^{-\frac{1}{4}\left(\frac{\rho}{\lambda_{(e/h)}}\right)^2}$$
$$\times {}_1F_1\left(-n,M_{(e/h)}+1,\frac{1}{2}\left(\rho/\lambda_{(e/h)}\right)^2\right), \tag{2.74}$$

where ${}_1F_1$ is the hypergeometric function, $n = 0,1,2..$ is the radial quantum number, $m = 0,\pm1,\pm2,...$ is the angular momentum. The corresponding eigenenergies for the 3D problem

26

are

$$E_{n,m,l}^{(e/h)} = \left(n + \frac{1}{2} + \frac{M_{(e/h)}}{2}\right)\hbar\omega_{(e/h)} - \frac{m}{2}\hbar\omega_{c(e/h)}^*$$
$$- \frac{\mu_{(e/h)}^*}{4}\omega_{0(e/h)}^2{\rho_0}^2 + \left(\frac{l^2\pi^2\hbar^2}{2\mu_{(e/h)}^*L^2}\right), \tag{2.75}$$

with $M_{(e/h)} = \sqrt{m^2 + \frac{2a_1\mu_{(e/h)}^*}{\hbar^2}}$, $\omega_{c(e/h)}^* = eB/\mu_{(e/h)}^*$, $\omega_{0(e/h)} = \sqrt{8a_2/\mu_{(e/h)}^*}$, $\omega_{(e/h)} = \sqrt{\omega_{c(e/h)}^2 + \omega_{0(e/h)}^2}$ and $\lambda_{(e/h)} = \sqrt{\frac{\hbar}{\mu_{(e/h)}^*\omega_{(e/h)}}}$.

The iso-probability surfaces corresponding to lower values of the quantum numbers n, m and l (quantum number of the confinement on the z direction) of the wave function are displayed in Fig. 2.8. We shall use the function of the Eq. (2.73) as a basis set for the representation of the **k.p** Luttinger Hamiltonian for the valence band states within the multiband envelope function approximation

$$\Phi(\rho,\varphi,z) = \sum_{n,m,l} C_{n,m,l}\psi_{n,m,l}(\rho,\varphi,z). \tag{2.76}$$
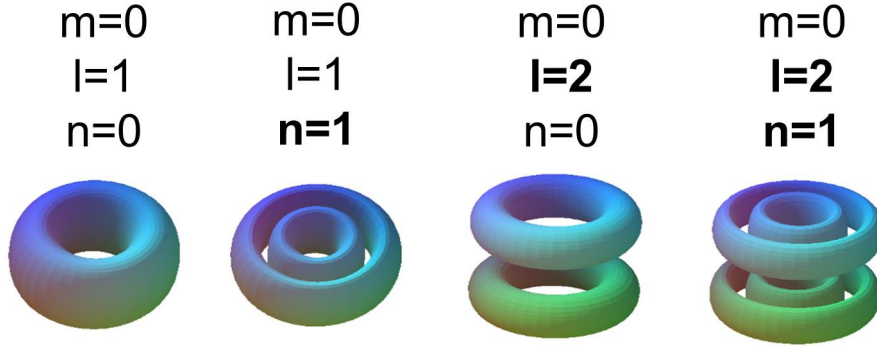
Figure 2.8: QR electronic orbitals for different values of l and n, with $m = 0$.

The matrix elements for QR Luttinger Hamiltonian as function of quantum number m are shown in Appendix D.

The QW and QD/QR were used to study confinement, external fields and asymmetries effects. Besides, we use our more complex and complete QR shapes to analyze the potential effects on the geometric phase of the potential profile asymmetries, that are shown in the upcoming chapters.

2.5 Geometric phase

Geometric phase acquired over the course of a cycle, when a system is subjected to cyclic adiabatic processes, which results from the geometrical properties of the parameter space of the Hamiltonian.

Berry found that an additional phase factor occurs in contrast to the well known dynamical phase factor. This phenomenon can be described by "global change without local change". But this was not the first time that someone found such a phase factor. Considerations, for instance, of the Born-Oppenheimer approximation done by Mead and Truhlar in 1979 [33] revealed also this additional phase factor but it had been neglected. Berry showed that this was not correct because the phase is gauge invariant and therefore can not be gauged away. Ever since, much work has been done on this issue and the so called Berry phase is now well established, theoretically as well as experimentally [34].

The Berry phase of a given eigenstate v was defined as [35]

$$\Theta_v = i \int_0^{2\pi} \langle \Psi_v \mid \frac{\partial}{\partial \hat{\varphi}} \mid \Psi_v \rangle d\hat{\varphi} \tag{2.77}$$

where φ parametrizes a cyclic adiabatic process. It follows a closed path around the QR.

To understand the concept of Berry phase, we should think about the conditions where this phase is build up. To do this, we must first introduce the description of an adiabatic processes. A good example that illustrates it can be given by imagining a perfect pendulum inside a box with no friction or air resistance, oscillating back and forth in a vertical plane. If the box is grabbed and shacked in a jerky manner, the bob will swing around in a wild chaotic fashion. But if moved gently and steadily, the pendulum will continue to swing in a nice, smooth way, in the same plane (or one parallel to it) with the same amplitude (and, of course, the same frequency). This gradual change in the external conditions characterizes an adiabatic process.

Using this classical model, we can imagine that this ideal pendulum can be set down to the point A, at the equator, and set it swinging, in the direction North-South as represented in Fig. 2.9. For the moment, we will pretend the earth is not rotating. Very gently (that is, adiabatically), it can be carried up to the North Pole, and then down the to the point B (where the pendulum does not swing in North-South direction anymore). Then, it can be carried back to the point A, along the new longitude line. It is clear that the pendulum will no longer be swinging in the same plane as it was when it was set out. Indeed, the new plane makes an angle

α with the old one.
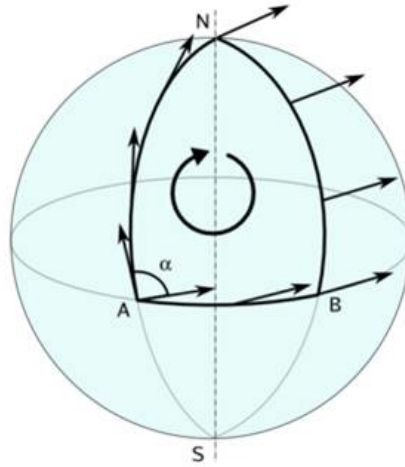
Figure 2.9: Itinerary for adiabatic transport of a pendulum on the surface of the earth.

Lets assume that α is equals the solid angle (Ω) subtended by the path around which the pendulum was carried. This path surrounds a fraction $\alpha/2\pi$ of the A point, so its area is $Area = (1/2)(\alpha/2\pi)4\pi R^2 = \alpha R^2$ (where R is the earth radius), and hence

$$\alpha = \frac{Area}{R^2} = \Omega \tag{2.78}$$

This turns out to be independent of the shape of the path, as shown in Fig. 2.10. Incidentally, the Foucault pendulum is an example of precisely this sort of adiabatic transport around a closed loop on a sphere.
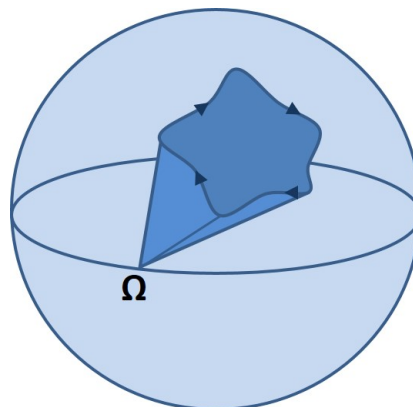
Figure 2.10: Arbitrary path on the surface of a sphere, subtending a solid angle.

A system which does not return to its original state when transported around a closed loop, is said to be nonholonomic (The "transport" in question does not need to involve a physical

motion: What we have in mind is that the external parameters of the system are changed in some fashion that eventually returns them to their initial values).

Yet one question is still open. **Is Berry phase mensurable?** We are used to think that the phase of the wave function is arbitrary and that physical quantities involve just $|\Psi|^2$, thus the phase factor cancels out. But Θ_v can be measured, if (for example) we take a beam of particles (all in the state Ψ) and split it in two, so that one beam passes through an adiabatically changing potential, while the other does not. When the two beams are recombined, the total wave function has the form

$$\Psi = \frac{1}{2}\Psi_0 + \frac{1}{2}\Psi_0 e^{i\Gamma} \tag{2.79}$$

where Ψ_0 is the "direct" beam wave function, and Γ is the extra phase (in part dynamic, and in part geometric) acquired by the beam subjected to the varying B). In this case

$$
\begin{aligned}
|\Psi|^2 &= \frac{1}{4}|\Psi_0|^2(1+e^{i\Gamma})(1+e^{-i\Gamma}) \\
&= \frac{1}{2}|\Psi_0|^2(1+\cos\Gamma) = |\Psi_0|^2(1+\cos^2\Gamma/2).
\end{aligned}
\tag{2.80}
$$

So by looking for points of constructive and destructive interference (where Γ is an even or odd multiple of π, respectively), one can easily measure Γ. Berry, and other early writers, worried that the geometric phase might be swamped by a larger dynamic phase, but it has been proved possible to arrange things so as to separate out the two contributions [36].

In our case, we have studied the Berry phase under a controllable magnetic field angle within an asymmetric QR. We were able to study the influence of the angle of the applied field and the asymmetry of the QR shape.

Bibliography

[1] N. W. Ashcroft and N. D. Mermin, Solid State Physics. Orlando: Harcourt, 1976.

[2] C. Kittel, Introduction to Solid State Physics. New York: Wiley, 1963.

[3] W. Lopes, Revista Brasileira de Ensino de Física **32**, 3308 (2010).

[4] E. H. Putley, The Hall Effect and Related Phenomena. London: Butterworths, 1960.

[5] E. F. Schubert, Quantum Mechanics Applied to Semiconductor Device. New York: Wiley, 1986.

[6] G. Bastard, Wave Mechanics Applied to Semicondutor Heterostructures. New York: Wiley, 1990.

[7] R. Winkler, Spin-Orbit Coupling Effects in Two-Dimensional Electron and Hole Systems. Erlangen: Springer, 2003.

[8] S. Datta, Quantum Phenomena (Modular Series on Solid States Devices). New York: Addison Wesley, 1989.

[9] F. J. Ohkawa and Y. Uemura, J. Phys. Soc. Jpn. **37**, 1325 (1974).

[10] Y. A. Bychkov and E. I. Rashba, J. Phys. C: Solid State Phys. **17**, 6039 (1984).

[11] Y. A. Bychkova and E. I. Rashba, JETP Lett. **39**, 78 (1984).

[12] G. Lommer, F. Malcher, and U. Rossler, Phys. Rev. B **32**, 6965 (1985).

[13] U. Rossler, F. Malcher, G. Lommer: "Spin splitting in structured semiconductors", in *High Magnetic Fields in Semiconductor Physics II*, ed. by G. Landwehr (Spring, Berlin, Heidelberg, 1989), Vol. 87 of Solid-State Sciences, p. 376

[14] E. O. Kane, J. Phys. Chem. Solids **1**, 82-99 (1956).

[15] E. O. Kane, The $\vec{k}.\vec{p}$ Method in: Semiconductor and Semimetals. (R. K. Willardson and A. C. Beer), cap. 3, v. 1. New York: Academic Press, 1966.

[16] J. M. Luttinger, Phys. Rev. **102**, 1030 (1956).

[17] P.-O. Löwdin, J. Chem. Phys. **19**, 1396 (1951).

[18] V. Lopez-Richard, *Magneto-Optical Properties of Zinc-Blende Type Semiconductors and Semiconductor-Nanostructures.* Departamento de Física da Universidade Federal de São Carlos, 2001. Tese.

[19] E. Kane, Physics of III-V Compounds. v. 1. p. 75, New York: Academic Press, 1966.

[20] E. O. Kane, J. Phys. Chem. Solids **1**, 249 (1957).

[21] K. Suzuki and J. C. Hensel, Phys. Rev. B **9**, 4184 (1974).

[22] H. R. Trebin, U. Rössler, and R. Ranvaud, Phys. Rev. B **20**, (1979).

[23] G. L. Bir, G. E. Pikus, Symetry and Strain-Induced Effects in Semiconductors. New York: Wiley, 1974.

[24] R. Hooke, The Potentia Restitutiva. London, 1678.

[25] L. D. Landau, E. M. Lifshitz, Theory of Elasticity. v. 7. 2 ed. Pergamon, 1959.

[26] T. Nuytten, M. Hayne, B. Bansal, H. Y. Liu, M. Hopkinson, and V. V. Moshchalkov, Phys. Rev. B **84**, 045302 (2011).

[27] S. Tomic and E. P. O'Reilly, Phys. Rev. B **71**, 233301 (2005).

[28] J. -Y. Marzin and G. Bastard, Solid. State. Communications **92**, 437-442 (1994); A. Fuhrer, S. Lusher, T. Ihn, T. Heinzel, K. Ensslin, W. Wegscheider, and M. Bichler, Nature **413**, 822 (2001).

[29] V. Lopes-Oliveira, Y. I. Mazur, L. D. Souza, L. A. B. Marçal, J. Wu, M. D. Teodoro, A. Malachias, V. G. Dorogan, M. Benamara, G. G. Tarasov, E. Marega Jr., G. E. Marques, Z. M. Wang, M. Orlita, G. J. Salamo, and V. Lopez-Richard, Phys. Rev. B **90**, 125315 (2014).

[30] W.-C. Tan and J. C. Inkson, Semicond. Sci. Technol. **11**, 1635-1641 (1996).

[31] L. D. Landau, E. M. Lifshitz, Quantum Mechanics (Non-relativistic Theory). v. 3. 3 ed. 1977.

[32] F. Nagasawa, D. Frustaglia, H. Saarikoski, K. Richter, and J. Nitta, Nature Communications **4**, 2526 (2013).

[33] C. A. Mead and D. G. Truhlar, J. Chem. Phys. **70**, 2284 (1979).

[34] K. Durstberger, Geometric Phases in Quantum Theory. Wien: Universitat Wien, 2002.

[35] D. Xiao, M. -C. Chang, and Q. Niu, Rev. Mod. Phys. **82**, 1959 (2010).

[36] D. J. Griffiths, Introduction to Quantum Mechanics. New Jersey: Printice Hall, 1994.

Chapter 3

SELF-ORGANIZATION EFFECTS: Localization and Strain

In this chapter, we focus our discussion on the effects of the growth process in semiconductor nanostructures. Although this work aims studying the structural properties of QRs, it is important to analyze the effects of reduced confinement and the appearance of strain fields starting from layered structures such a QWs. We use indeed QW profiles to model the vertical confinement of our nanostructures. Thus, the effect of composition, confinement, strain and localization will be discussed and this will help us better understand the complex QR system that are analyzed in sequence.

This chapter is organized as follows: Section 3.1 presents a brief introduction. Section 3.2 discusses strain and localization effects in QWs. In section 3.3, the strain and confinement effects in QRs are outlined and section 3.4 is devoted to the conclusions.

3.1   Introduction

Nowadays, the advances in growth techniques have resulted in a wide spectrum of nanoscale structures suitable for various applications. The use of MBE techniques has made possible the growth of semiconductor structures ranging from simple QW to QD or QR. The thorough control of structural parameters in this process allows the engineering of the electronic structure which is sensitive to alloy compositions, confinement profiles, strain, and external fields. The simultaneous combination of such effects results in the particular behaviors analyzed in this thesis.

For instance, it is known that the presence of small amounts of nitrogen (N) in conventional III-V arsenide based alloys causes a drastic decrease in the band gap emission due to the coupling between the bottom conduction band and the top of the resonant band of localized nitrogen [1, 2], which alters the optical emission in different ways [3–6]. The potential applications of nitrogenated systems as optoelectronic devices working in the optical range of $1.30 - 1.55 \mu$m are the motivations for studying them. Additionally, given the growth at low temperature of nitrogenated layers, the appearance of interface alloy imperfections due to the changing of the lattice parameters is practically unavoidable inducing local modulation of the band gap [7, 8]. This also imposes some theoretical challenges since various band parameters are not currently reported and have to be determined to build the **k.p** Hamiltonian. Apart from effects due to the N addition, strain and confinement can also cause drastic changes on the electronic structure and optical response by the symmetry breakdown. Indeed, in the case of QRs, the ring geometry itself might be affected by localized defects produced during the growth processes.

When the growth of these structures is produced in layers, the vertical stacking induces the self-assembling, starting from the QD seeds towards the QRs, along with their lateral alignment. It is then imperative to assess the relative contribution of each mode to the optical response, since their geometries and strain field propagation may affect differently the responses. Thus, the electronic structure, in particular in the valence band, where anisotropy and deformation potentials are so crucial, must be accounted for. We will show that these effects can be enhanced by the application of a magnetic field.

Our interest here is to correlate strain and confinement modulation produced by defects introduced during the growth processes in nitrogenated QW, that will be modelled as localized states in QD-like structures, and single QRs [9–13].

3.2 Structural effects of the layers growth in the electronic structure: InGaAs and InGaAsN

In this section, we discuss some impacts of confinement, strain, and alloy imperfection based on the experimental optical properties of [001] InGaAsN/GaAs and InGaAs/GaAs QWs. The model used here was described in section 2.4.1 on the previous chapter. Our calculations use the Bir-Pikus Hamiltonian formalism [14] to emulate the effects of the strain fields on the

electronic properties. The biaxial strain produced at the interfaces of the structure is introduced into the multiband calculation, where the hydrostatic component (δE_h) renormalizes the gap proportionally to the deformation potential $a_d = a_v + a_c$, with a_v being the valence band contribution and a_c the contribution of the conduction band. In turn, the shear strain leads to the relative shift (δE_s) between the top valence subbands for HH, E_{hh}, and LH, E_{lh}.

Since, to our knowledge, the ternary $In_{0.36}Ga_{0.64}As$ and quaternary $In_{0.36}Ga_{0.64}As_{0.988}N_{0.012}$ alloys, have no structural parameters values reported in the literature, it was necessary to determine them according to the material concentration for $A_xB_{1-x}C$ and $A_xB_{1-x}C_{1-y}D_y$. We interpolated between reported values of band parameters corresponding to the relevant binary alloys. Thereby, the equations used for the interpolation [15] are

$$Q(x) = xQ_{AC} + (1-x)Q_{BC} \tag{3.1}$$

$$Q(x,y) = x(1-y)Q_{AC} + xyQ_{AD} + (1-x)(1-y)Q_{BC} + (1-x)yQ_{BD}. \tag{3.2}$$

where $Q(x)$ and $Q(x,y)$ are the parameters to be determined for ternary and quaternary alloys, respectively, and x and y define the relative content of each specie. The relevant parameters obtained by the interpolation are listed in Table C.1 in Appendix C. However, for the energy gap, the nitrogen content causes an anomalous shrinking impossible to emulate by a simple interpolation.

It is notably that for both GaN and InN, the value of the energy gap exceeds the one for InGaAs regardless of the In-content. Thus, we used available alternative models to obtain the gaps of the ternary $E_g^{In_xGa_{1-x}As}$ and quaternary alloys $E_g^{In_xGa_{1-x}As_{1-y}N_y}$ [16–18] which accounts for the coupling between the nitrogen resonant level and the conduction band edge.

$$E_g^{In_xGa_{1-x}As} = 0.4105 + 0.6337(1-x) + 0.475(1-x)^2, \tag{3.3}$$

$$E_g^{In_xGa_{1-x}As_{1-y}N_y} = \frac{1}{2}\left\{ E^c(k) + E^N \pm \sqrt{[E^c(k) - E^N]^2 + 4S^2y} \right\} \tag{3.4}$$

where $E^c(k) = E_g^{In_xGa_{1-x}As}$,

$$E^N = 1.65(1-x) + 1.44x - 0.38x(1-x), \tag{3.5}$$

and

$$S = 2.7(1-x) + 2x - 3.5x(1-x). \tag{3.6}$$

It is well known that the split-off and top valence bands, in InGaAs QWs samples, are separated by more than 300 meV. Therefore, we have neglected the split-off effects and used a Luttinger Hamiltonian including strain. The contribution of strain to the HH and LH subbands are given by Eqs. (2.67) and (2.68). In turn, the representation of the Luttinger Hamiltonian for systems grown along the direction [001] is given by Eq. (2.66).

The strain effects in QWs changes both the conduction as valence bands. Following the experimental InGaAs and InGaAsN QW samples configuration, we calculated the variation of the conduction and valence band edges when the strain ($\varepsilon_\parallel$) changes from negative to positives values. The calculations were done for two QW sizes: 4 and 7 nm, and two compositions: $In_{0.36}Ga_{0.64}As$ and $In_{0.36}Ga_{0.64}As_{0.988}N_{0.012}$. The results are presented in Fig. 3.1. It is notable how the sign of the strain ($\varepsilon_\parallel$) affects the electronic structure, what is observed through the relative shift of the HH and LH sub-band.
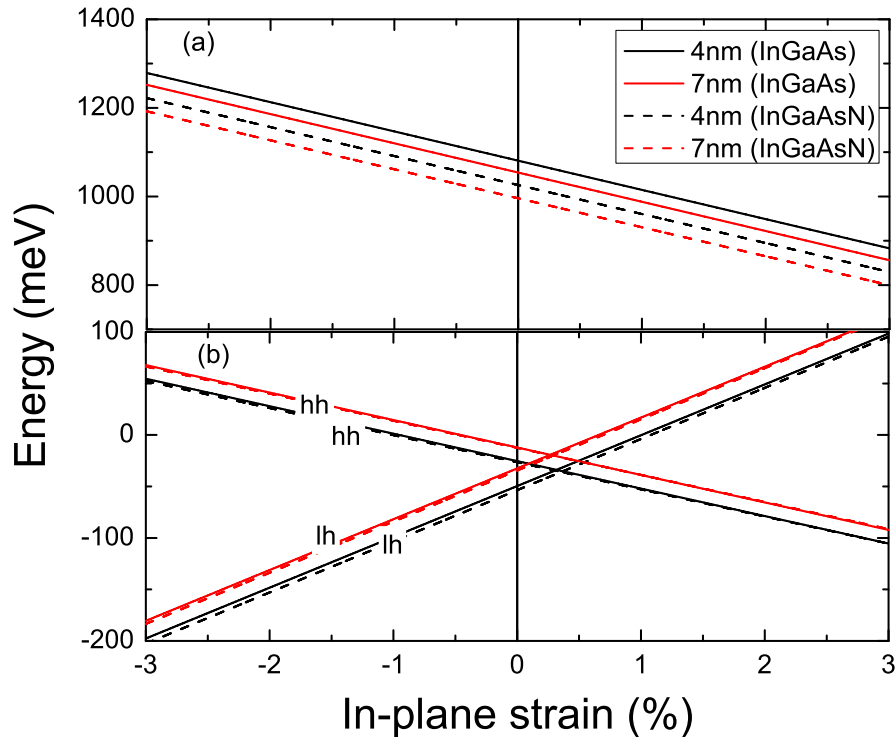
Figure 3.1: (a) Comparison between the conduction band edges as function of strain for the profiles corresponding to the samples of InGaAs and InGaAsN quantum well for two different sizes: 4 and 7nm. (b) Comparison between the valence subbands energies as function of strain for the profiles corresponding to the samples of InGaAs and InGaAsN quantum well for two different sizes: 4 and 7nm.

In Fig. 3.1, we show how a compressive strain ($\varepsilon_{\parallel} < 0$) increases the emission energy for optical recombinations involving either electron-LH or electron-HH. Yet, the electron-HH transition shift is less significant since the HH and conduction band move in the same direction.

The localization effects can be understood as the presence of small localization cores of volume Ω. The wave function Ψ_0, defined within V_0, transforms to $\Psi = \Psi_0 + \phi$, where ϕ is defined within the volume Ω, and the Hamiltonian, H_0, transforms to $H = H_0 + \Delta H$, within the total volume $V_T = V_0 + \Omega$. By defining, $\frac{1}{V_0} \int_{V_0} \Psi_0^* H_0 \Psi_0 dv = E_0$, $\frac{1}{\Omega_0} \int_{\Omega_0} \phi_0^* H_0 \phi_0 dv = \Delta E$, the eigenvalue of H can be determined as

$$E = \frac{1}{V_T} \int_{V_T} \Psi^* H \Psi dv = \frac{1}{V_T} \int_{V_0} \Psi_0^* H_0 \Psi_0 dv + \frac{1}{V_T} \int_{\Omega} \phi_0^* H_0 \phi_0 dv \tag{3.7}$$

$$E = \frac{V_0}{V_T} \frac{1}{V_0} \int_{V_0} \Psi_0^* H_0 \Psi_0 dv + \frac{\Omega}{V_T} \frac{1}{\Omega} \int_{\Omega} \phi_0^* H_0 \phi_0 dv \tag{3.8}$$

$$E = \frac{V_0}{V_T} E_0 + \frac{\Omega}{V_T} \Delta E. \tag{3.9}$$

This can be approximated to

$$E = E_0 + \frac{\Omega}{V_T} \Delta E \tag{3.10}$$

in the case where $\Omega \ll V_0$.

For a cylindrical localization core, as represented in Fig. 3.2(a), $\Omega = \pi \Delta_{xy}^2 \Delta_z / 4$. According to Eq. (2.34), the diagonal energy values of the HH and LH valence band ground states localized within Ω are given by

$$\Delta E_{hh(lh)} = -\frac{\hbar^2 \pi^2}{2\mu_{hh/lh}^z \Delta_z^2} - \frac{\hbar^2 (2\rho)^2}{2\mu_{hh/lh}^{xy} \Delta_{xy}^2} \tag{3.11}$$

where the $\mu_{hh/lh}^{z/xy}$ were already defined in Eqs. (2.38), (2.39), (2.40) and (2.41), Δ_{xy} and Δ_z are the effective dimensions of the localized state at the interface due to disorder. The first term of the Eq. (3.11) is the solution in the z direction similar to a QW problem solution, while the second one is the solution of a cylindrical confinement problem based on Bessel functions, with $\rho \simeq 2.4048$ being the zero of the Bessel function $J_0(\rho) = 0$.

The corresponding correction to the energy difference between both valence sub-bands, $\delta E_{hh} - \delta E_{lh} = \frac{\Omega}{V_T}(\Delta E_{hh} - \Delta E_{lh})$, is given by

$$\delta E_{hh} - \delta E_{lh} = \frac{\Omega}{V_T} \left[-\frac{\hbar^2 \pi^2}{2\mu_{hh}^z \Delta_z^2} - \frac{\hbar^2 4\rho^2}{2\mu_{hh}^{xy} \Delta_{xy}^2} + \frac{\hbar^2 \pi^2}{2\mu_{lh}^z \Delta_z^2} + \frac{\hbar^2 4\rho^2}{2\mu_{lh}^{xy} \Delta_{xy}^2} \right] \tag{3.12}$$

$$\delta E_{hh} - \delta E_{lh} = \frac{\Omega}{V_T} \frac{\hbar^2}{2} \left[\frac{\pi^2}{\Delta_z^2} \left(\frac{1}{\mu_{lh}^z} - \frac{1}{\mu_{hh}^z} \right) + \frac{4\rho^2}{\Delta_{xy}^2} \left(\frac{1}{\mu_{lh}^{xy}} - \frac{1}{\mu_{hh}^{xy}} \right) \right] \qquad (3.13)$$

$$\delta E_{hh} - \delta E_{lh} = \frac{\Omega \hbar^2}{2V_T} \frac{1}{\Delta_{xy}^2} \left[\pi^2 \left(\frac{\Delta_{xy}}{\Delta_z} \right)^2 \left(\frac{4\gamma_2}{m_0} \right) + 4\rho^2 \left(\frac{-2\gamma_2}{m_0} \right) \right] \qquad (3.14)$$

$$\delta E_{hh} - \delta E_{lh} = \frac{4\gamma_2 \Omega \hbar^2}{2V_T \Delta_{xy}^2 m_0} \left[\pi^2 \left(\frac{\Delta_{xy}}{\Delta_z} \right)^2 - 2\rho^2 \right] \qquad (3.15)$$

using the expression for Ω and $V_T = \pi L_z R_{eff}^2$

$$\delta E_{hh} - \delta E_{lh} = \varepsilon_0 \gamma_2 \frac{\Delta_z}{L_z} \left[\pi^2 \left(\frac{\Delta_{xy}}{\Delta_z} \right)^2 - 2\rho^2 \right] \qquad (3.16)$$

with $\varepsilon_0 = \frac{\hbar^2}{2m_0 R_{eff}^2}$, the binding energy for the unperturbed wavefunction confined within the QW and spread laterally within the effective Bohr radius.
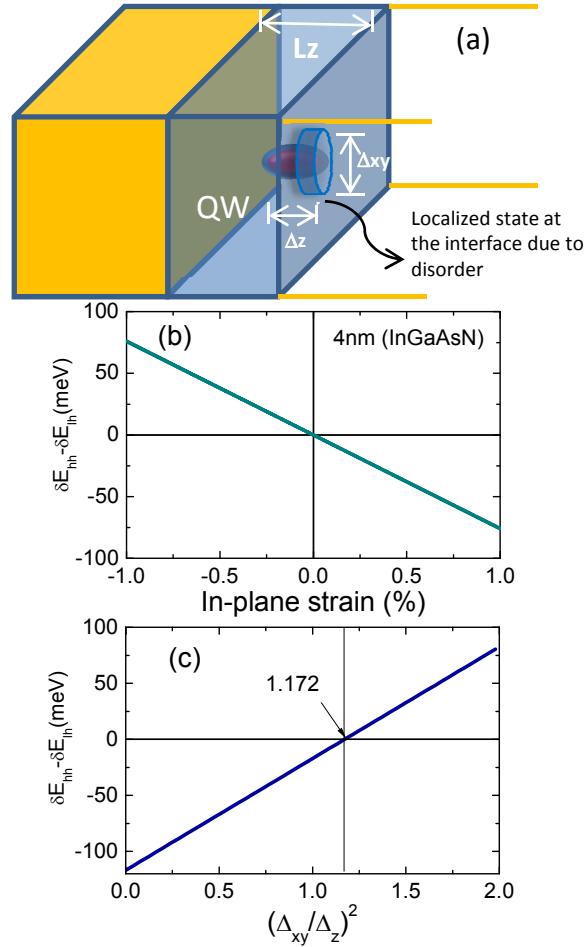
Figure 3.2: Diagram representing the QW layer with a lateral localization core with cylindrical symmetry. (a) Relative valence subband shift, $\delta E_{hh} - \delta E_{lh}$, due to strain effects. (b) The same shift by considering just the localization effects as a function of the square aspect ratio.

To associate the strain and localization effects, and show how they are comparable to each other, we plot the relative subband shift, $\delta E_{hh} - \delta E_{lh}$, obtained from Eqs. (2.67) and (2.68) and shown in Fig. 3.2(b) as a function of strain, and from Eq. (3.16), as a function of the square aspect ratio, $\left(\frac{\Delta_{xy}}{\Delta_z}\right)^2$ by using $\varepsilon_0 = 17.5\text{meV}$ from Ref. [19]. This comparison is possible when we consider a local one-monolayer fluctuation of the QW size, which according to Table C.1 (Appendix C) corresponds to $\Delta_z/L_z \sim 0.15$ for $L_z = 4\text{nm}$. The results shown in Figs. 3.2(b) and 3.2(c) illustrate that both strain modulation and the aspect ratio, in confined valence band states, tune the relative sub-band position. This has a potential effect on the hybridization of valence sub-bands due to interband coupling, as described by the Hamiltonian in Eq. (D.1). This coupling modulates various effective parameters such as effective masses, Lande factors, and diamagnetic shifts, as well as their dependence on external fields [18, 19].

The experimental results obtained by collaborators for high-resolution x-ray diffraction (HRXRD) and PL, shown in Figs. 3.3 and 3.4, respectively, confirm our calculations. Such HRXRD (Fig. 3.3) shows that the introduction of nitrogen induces a reduction in the lattice parameter along z, leading to a shift of the diffraction angle toward the peak of GaAs, while the PL peak energy (Fig. 3.4) presents a red shift for N-containing QWs due to the reduction in energy gap with increasing N-content.
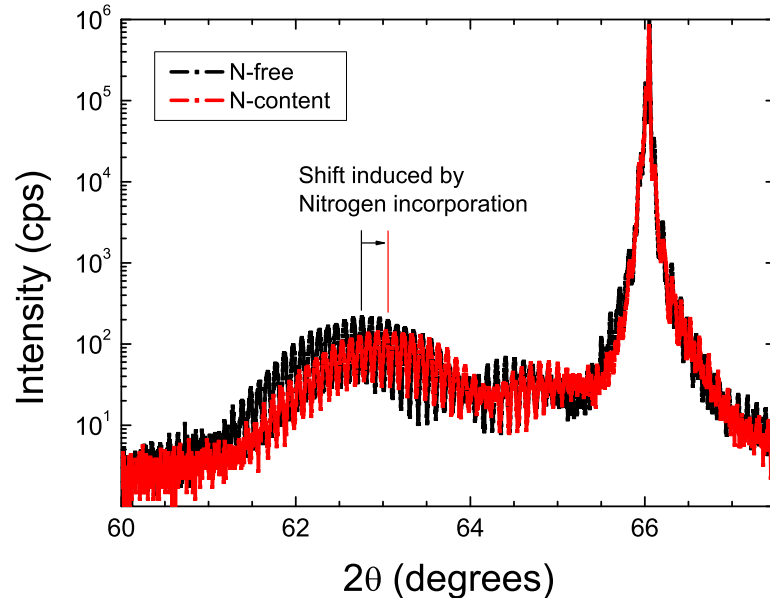
Figure 3.3: Comparison between sample N-free (black line) and N-containing QW (red line) x-ray diffraction. The shift of the red broad peak to higher angles is induced by nitrogen incorporated into the two QWs [21].

To connect our theoretical results to the optical experiments, we have studied the temper-
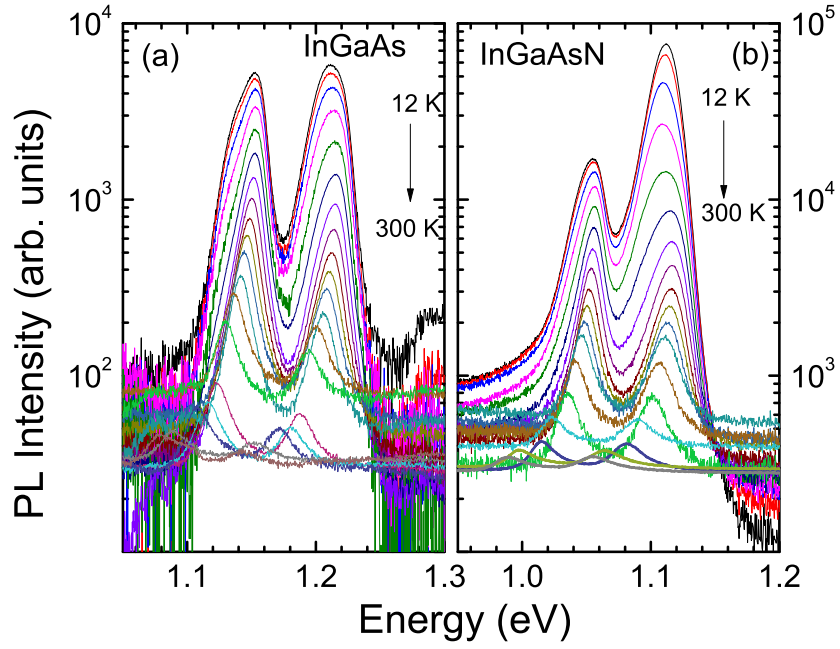
Figure 3.4: PL spectra as a function of temperature (a) InGaAs (QW) reference sample and (b) InGaAsN (QWN) sample. [21].

ature dependence of the PL peak energy for both samples in the range $10 - 300$K. Fig. 3.5 presents the theoretical and experimental results for the temperature dependence of the PL peak energy for both QWs with and without N. PL peak positions were estimated theoretically in the presence and absence of strain effects. In general, the decrease in emission energy as a function of temperature follows the Varshni model [22]

$$E_g(T) = E_g(0) - \frac{\alpha T^2}{T + \beta}. \tag{3.17}$$

The values of the Varshni's parameters were calculated by linear interpolation using the values obtained in Ref. [23] and are given in Table 3.1.

Table 3.1: Values of Varshni's parameters obtained by the interpolation (* $\alpha = 0.4$ was adjusted to the experimental curves)

	In$_{0.36}$Ga$_{0.64}$As	In$_{0.36}$Ga$_{0.64}$As$_{0.988}$N$_{0.012}$
$E_g(0)$ (meV)	1010.6	950.3
α (meV/K)	0.445	0.445 (* 0.4)
β (K)	164.04	169.37

In Fig. 3.5, for both InGaAs and InGaAsN, the dashed lines represent the theoretical re-
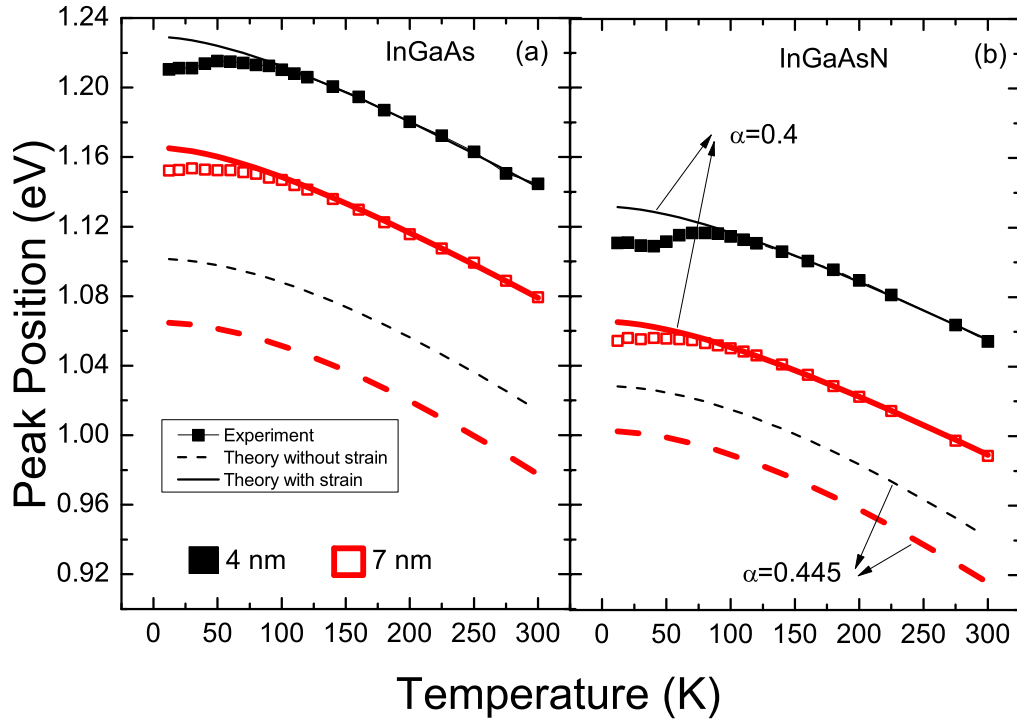
Figure 3.5: Transition energies as function of temperature. Experimental curves (dotted) and calculated values (curves): with strain effects (solid curves) and without strain (dashed curves) [21].

sults given by Eq. (3.17) excluding strain effects. By ascribing the gap difference between experiment and theory to strain effects, we can adjust these curves including the deformation $\varepsilon_\parallel$, whose values are given in Table 3.2. In the samples of $In_{0.36}Ga_{0.64}As$ QWs, the values of Varshni's parameters obtained by the interpolation process yield an adequate adjustment with the experiment, yet for the nitrogenated alloy, the experiment could only be fitted by reducing the value of α. However, we will show that beside the strain effects, various features detected experimentally can be unambiguously ascribed to the confinement modulation.

Table 3.2: Values of $\varepsilon_\parallel$ used in Fig. 3.5

Wells	Width	$\varepsilon_\parallel(\%)$
$In_{0.36}Ga_{0.64}As$	4nm	-2.62
$In_{0.36}Ga_{0.64}As$	7nm	-2.14
$In_{0.36}Ga_{0.64}As_{0.988}N_{0.012}$	4nm	-2.15
$In_{0.36}Ga_{0.64}As_{0.988}N_{0.012}$	7nm	-1.24

Note in Fig. 3.5 the S-shape obtained experimentally for the temperature dependence of the peak position which was associated to exciton localization given the high density of structural defects introduced during the low temperature growth of the QWs [9, 24]. We remark that such

S-shape behavior was observed for both samples. Yet, as expected, the InGaAsN QWs show more significant S-shape behavior as compared to the InGaAs samples and thus it is mainly associated to localization of carriers by structural defects.

In Fig. 3.6, we fitted the integrated PL intensity as a function of temperature for all QW configurations (N-containing and the reference) by the phenomenological expression,

$$I(T) = \frac{I_0}{1 + \gamma(1)e^{\frac{-E_a(1)}{k_B T}} + \gamma(2)e^{\frac{-E_a(2)}{k_B T}}}, \tag{3.18}$$

where $E_a(1,2)$ are the thermal activation energies, $\gamma(1,2)$ are the ratios between radiative and non-radiative lifetimes and I_0 is the intensity at $T = 0$K. The fitting parameters are presented in Table 3.3. To simplify the characteristic of integrated density, we use two non-radiative processes. The first process, $\gamma(1)$, is related to localized excitons, predominant at low temperature, while the second one, $\gamma(2)$, is relative to delocalized excitons, predominant at higher temperatures.

Table 3.3: Fitted parameters obtained by Arhenius plot

Parameters	I_0 (arb.un)	$\gamma(1)$	$E_a(1)$ meV	$\gamma(2)$	$E_a(2)$ meV
QW 4 nm	162	58	15	25000	68
QW 7 nm	141	17	11	7500	60
QWN 4 nm	1900	78	14	6400	50
QWN 7 nm	470	14	11	1500	46

Notice that both samples present similar values of activation energy for localized excitons. However, differences in the activation energies and radiative lifetimes ratios for the delocalized excitons reflect a slightly different localization effect for the N-containing sample which persists at higher temperatures. Based on the higher intensity for the thinner QW in the nitrogenated sample as compared to the thicker QW observed in Fig. 3.6, and ascribed to confinement effects, it was necessary to study the wave function behavior. We emulated the wave functions, $\Psi_{e(hh)} = F_{e(hh)}(z)\phi_{e(hh)}(r,\theta)$, within a finite barrier QW, $V_e(z)$ for electrons and $V_{hh}(z)$, for holes, according to the corresponding band offsets at the conduction and valence bands and a tunable effective lateral cylindrical confinement with effective radius R given by the Hamiltonian

$$H_{e(hh)} = \frac{p^2}{2\mu_{e(hh)}} + V_{e(hh)}(z) + \frac{\hbar^2}{2m_0 R^4}r^2, \tag{3.19}$$

with $p = -\hbar\Delta + e/cA$, and $A = B/2(-y,x,0)$, under magnetic field strength, B. In this ap-
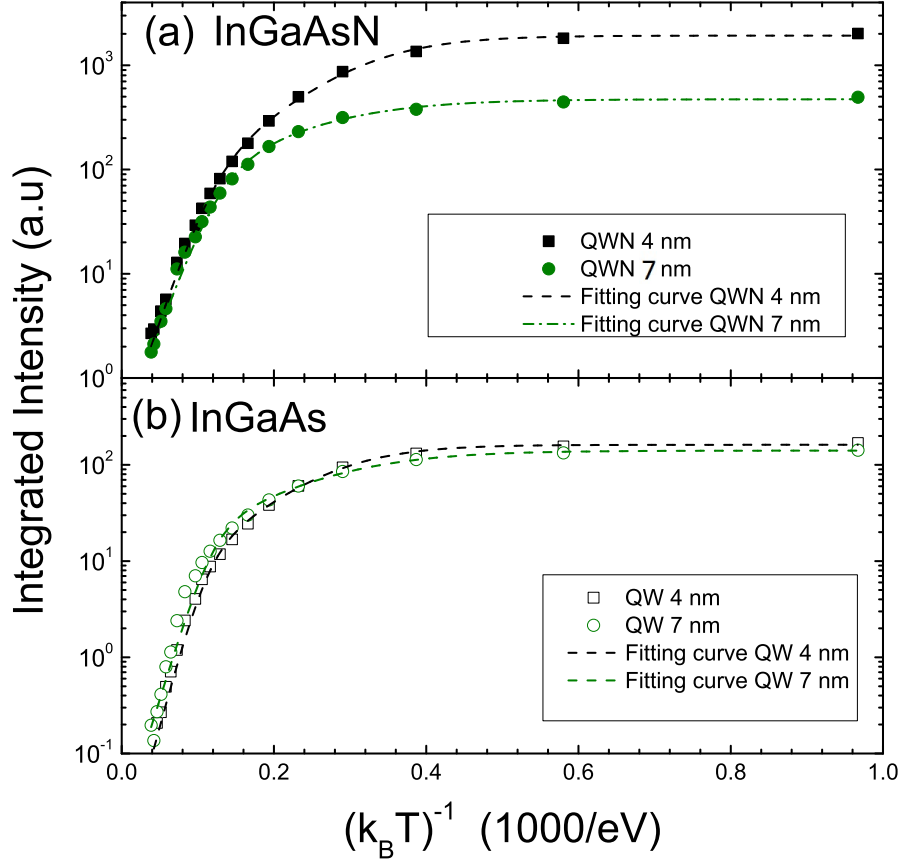
Figure 3.6: Integrated PL intensity as function of the inverse of temperature for: (a) InGaAsN samples of 4 and 7 nm and (b) InGaAs samples of 4 and 7 nm [21].

proach, the spin is assumed does not affect the wave function. Then, the overlap integrals $|\langle F_e(z)|F_{hh}(z)\rangle|^2$ and $|\langle \phi_e(r,\theta)|\phi_{hh}(r,\theta)\rangle|^2$, proportional to the intensity presented in Fig. 3.6, results in Fig. 3.7. Through Fig. 3.7(a), it is clear to see that by only reducing the QW width it would not produce an increase of the oscillator strength proportional to the overlap of wave functions. Yet, promoting a lateral effective confinement, either by reducing the value of the effective radius, R, or by increasing the magnetic field strength, as shown in Fig. 3.7(b), the probability of the electron-hole recombination can be enhanced.

In experimental results in Ref. [21] it was also observed a non-linear anomalous behavior for the magnetic shift of the 4 nm InGaAsN QW. It should be highlighted that this effect can be well ascribed to both strain and confinement modulation. This non-linear behavior of the magnetic shift of the valence band ground state calculated from the multiband k.p Hamiltonian was characterized in Fig. 3.8(a) for positive strain in an InGaAs QW. Yet, even for negative strains, as reported experimentally, a decreasing aspect ratio in confined hole states at the interfaces may lead to a drastic non-linear response as shown for a InGaAsN, 4 nm, QW as shown in Fig.
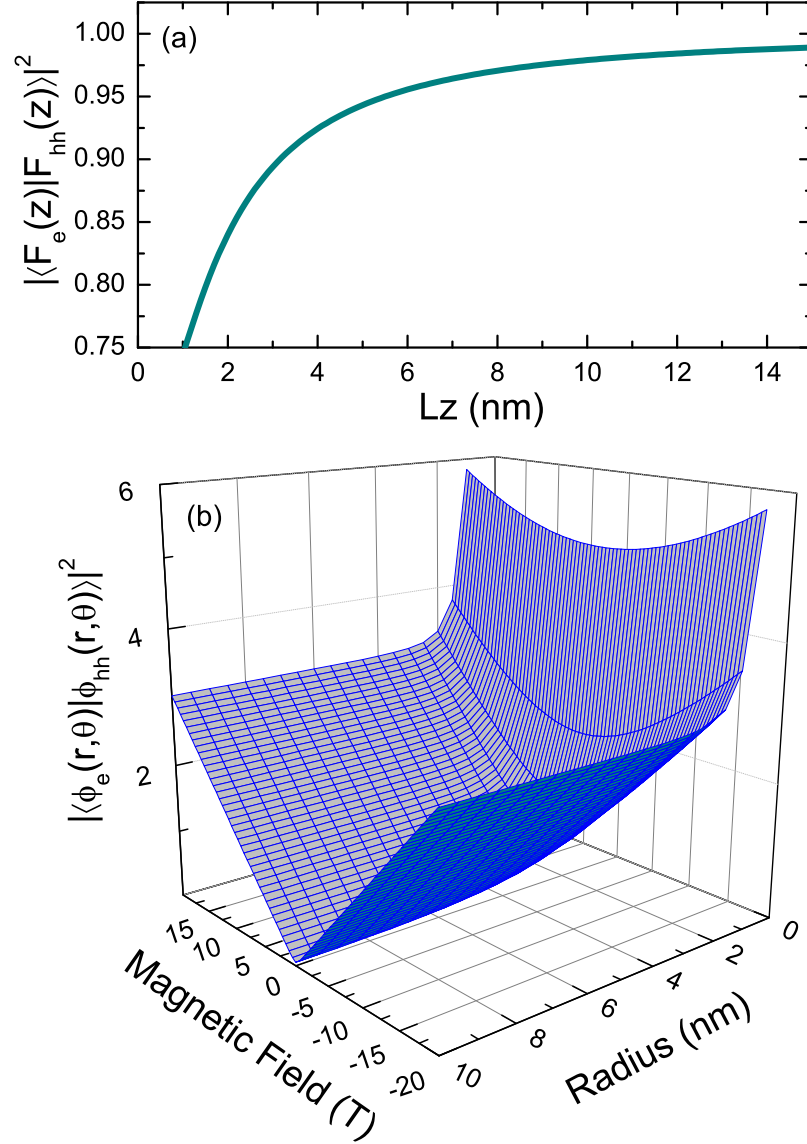
Figure 3.7: (a) Calculated overlap integral for a GaInAsN/GaAs QW as a function of its width, *Lz*. (b) Calculated overlap integral for the in-plane wavefunctions as a function of the lateral confinement radius, *R*, and magnetic field [21].

3.8(b). Note that negative values of $\mu_h^{xy}(B)$ can be attained at low fields. This will ultimately lead to increases in the reduced mass $\mu^{xy} = \mu_e^{xy}/(1 - \mu_e^{xy}/|\mu_h^{xy}|)$, flattening the magnetic shift of the electron-hole pair emission peak, as observed in the experiment in Ref. [21] or even an inversion of its sign, turning the electron-hole magnetic shift negative. This effect has already been predicted and measured for confined excitons [18, 19].

Assuming the magnetic energy of a trapped electron as given by an effective Hamiltonian and presented in Eq. (3.19), the solution for the ground state energy due to the lateral and
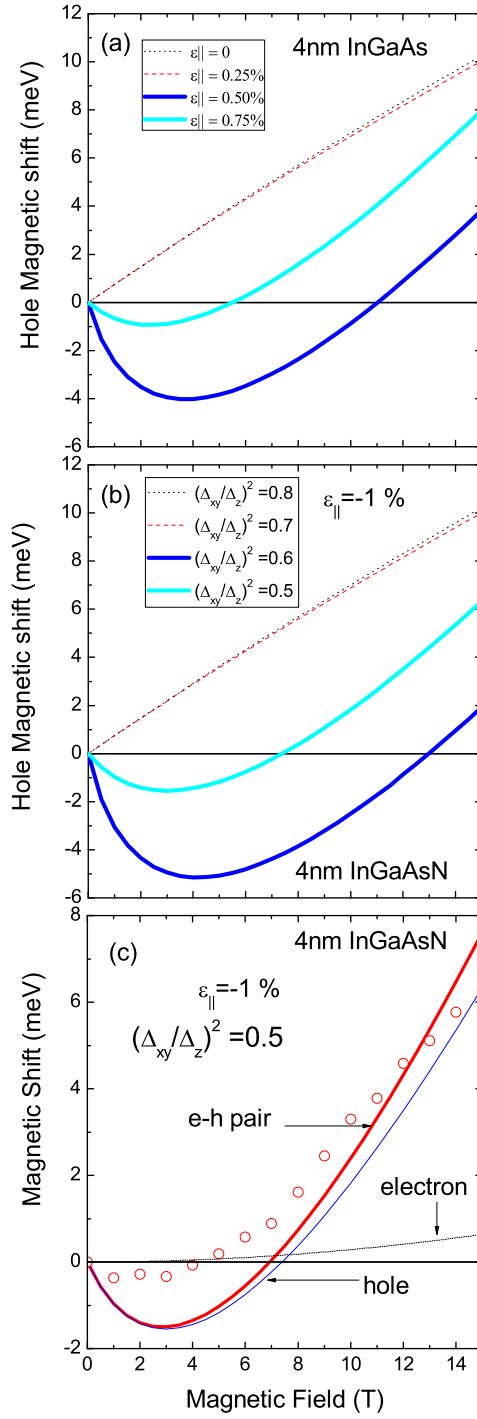
Figure 3.8: Calculated magnetic shift for: (a) the holes at the ground state of the 4 nm InGaAs QW for various values of the in-plane strain, (b) the holes ground state in a 4 nm InGaAsN QW at a fixed $\varepsilon_{||} = -1\%$ for various values of the square aspect ratio. (c) Calculated magnetic shift in a 4 nm InGaAsN QW for electrons, holes and electron-hh pair. The symbols represent the experimental results [21].

magnetic confinement is given by

$$E_e^{xy} = \frac{\hbar^2}{\sqrt{\mu^{xy} m_0 R^2}} \left[1 + \frac{1}{4\mu^{xy}} \left(\frac{eBR^2}{c\hbar} \right)^2 \right]^{\frac{1}{2}}. \tag{3.20}$$

This equation was used to calculate the effective magnetic shift for the single particle energy of the 4 nm InGaAsN QW, whose results are plotted in Fig. 3.8(c) for an effective radius of the lateral confinement $R = 1.2$ nm, and the electron mass reported in Table C.1. In Fig. 3.8(c), the symbols represent the experimental results and the net relative electron-hole energy modulation is also shown. The result attained would correspond to the weak magnetic field regime discussed in Ref. [6] when

$$B < \frac{2\sqrt{\mu^{xy}}\hbar c}{eR^2}. \tag{3.21}$$

Comparing experimental and calculated results, we ascribed the non-linear magnetic shift to the field tuning of the hole effective mass, $\mu^{xy}(B)$, due to nonparabolicity and inter-subband coupling.

We also feature the magneto-optical response and its correlation with the electronic structure. Here we focus on relevant valence band effects tuned by strain modulation and confinement. The first effect studied was the magnetic field effect in the valence band, whose results are presented in Fig. 3.9, where the valence band Zeeman Splitting of the ground state at 15 T is shown. In the Fig. 3.9(a), we can observe that the character changes from HH to LH for in-plane strain around 0.3%. This behavior is also presented in Fig. 3.1 and leads to a drastic shift in the magnetic splitting. It is also important to highlight the sign inversion of the Zeeman splitting by varying the values of the compressive strain, where the character of the ground state is predominantly HH.
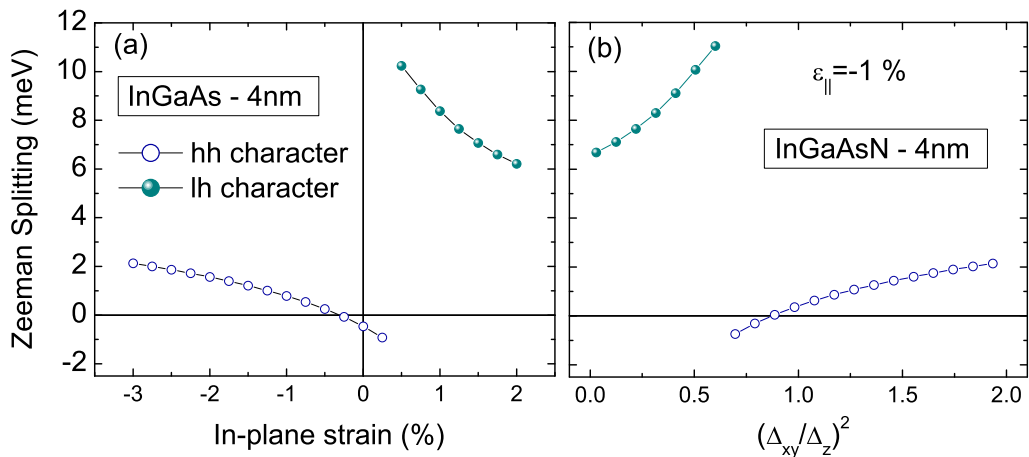
Figure 3.9: Calculated valence band ground state Zeeman splitting at 15 T for: (a) $In_{0.36}Ga_{0.64}As$ 4nm as a function of the in-plane strain and (b), for $In_{0.36}Ga_{0.64}As_{0.088}N_{0.012}$ for a fixed $\varepsilon_{\parallel} = -1\%$ as a function of the square aspect ratio [21].

In contrast, in Fig. 3.9(b), the aspect ratio, $\left(\frac{\Delta_{xy}}{\Delta_z}\right)^2$, decrease can even tune a character

change of the valence band ground state making it more LH-like. The values obtained for the valence band spin splitting in the vast part of the parameter range, shown in Fig. 3.9 (calculated at $B = 15\ T$), are in accordance with the values detected in the experiments for the electron-hole pair recombination in Ref. [21]. Yet, close to the parameter boundary where a character change takes place at the ground state, sudden changes of the magnetic response is expected (in agreement to the Fig. 3.1). According to the values represented in Fig. 3.9, we calculate the degree of spin polarization (DSP) of the valence band ground state.

Assuming the occupation probability given by

$$\frac{\partial n_\uparrow}{\partial t} = P_\uparrow - \frac{n_\uparrow}{\tau_s} - \frac{n_\uparrow}{\tau} + \frac{n_\downarrow}{\tau_s} e^{-\frac{\Delta E}{k_B T}} \tag{3.22}$$

$$\frac{\partial n_\downarrow}{\partial t} = P_\downarrow + \frac{n_\uparrow}{\tau_s} - \frac{n_\downarrow}{\tau} - \frac{n_\downarrow}{\tau_s} e^{-\frac{\Delta E}{k_B T}} \tag{3.23}$$

in the stationary condution, $\frac{\partial n_\uparrow}{\partial t} = \frac{\partial n_\downarrow}{\partial t} = 0$
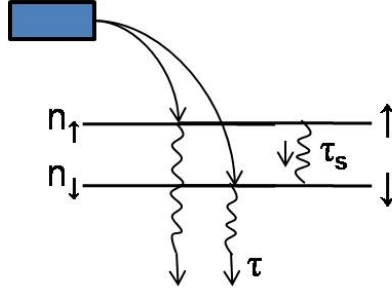
Figure 3.10: Degree of polarization.

$$DSP = \frac{n_\uparrow - n_\downarrow}{n_\uparrow + n_\downarrow} \tag{3.24}$$

getting the equation

$$DSP = \frac{\Delta E_{\uparrow\downarrow}}{|\Delta E_{\uparrow\downarrow}|} \left[\frac{exp\left(\frac{-|\Delta E_{\uparrow\downarrow}|}{k_B T}\right) - 1}{\left(1 + \frac{\tau_s}{\tau}\right) + exp\left(\frac{-||\Delta E_{\uparrow\downarrow}|}{k_B T}\right)} \right]. \tag{3.25}$$

According to Eq. (3.25) we got Fig. 3.11 where $\Delta E_{\uparrow\downarrow}$ is the energy difference between the spin-up and down states. The ratio τ_s/τ was set to 0.1 that is reasonable for QWs of this size [25], where τ_s is the flipping time of the spin and τ is the optical recombination time. Note in this case that despite the monotonic variation of the Zeeman splitting described before as a function of the structural parameters (strain and aspect ratio of the confined state), the DSP for holes in Fig. 3.11 follows very flat behaviors at $T = 2$ K below and above the critical parameter region
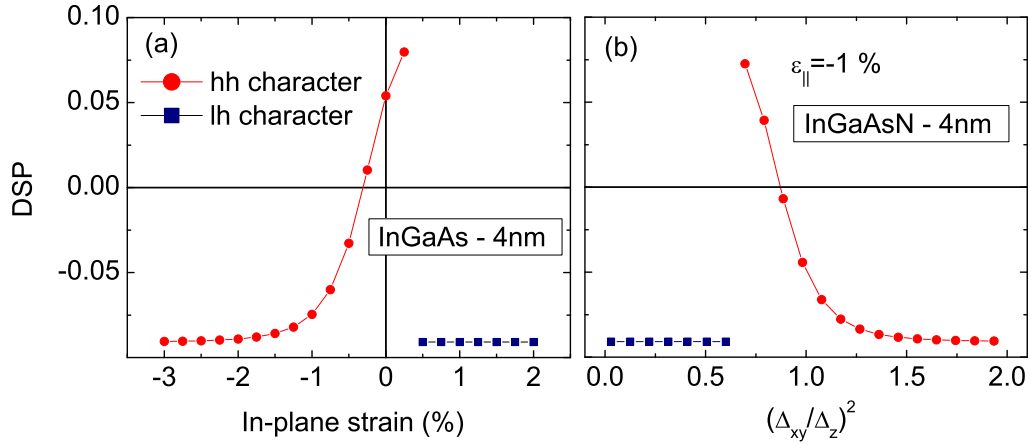
Figure 3.11: Calculated degree of spin polarization for the valence band ground state at 15 T, for: (a) the 4 nm $In_{0.36}Ga_{0.64}As$ quantum well at T=2 K as a function of the in-plane strain and (b) for the 4 nm $In_{0.36}Ga_{0.64}As_{0.088}N_{0.012}$ QW at a fixed $\varepsilon_{||} = -1\%$ as a function of the square aspect ratio [21].

($\varepsilon_{||} \sim 0.5$ in Fig. 3.11(a) or $\Delta_{xy}/\Delta_z \sim 0.5$ in Fig. 3.11(b)), where the character of the valence ground state changes. The valence band DSP is, under these conditions, close to -10%, at $B = 15$ T. Thus, the experimental observation of a slight dependence of the polarization degree on the structural parameters in Ref. [21] can, in principle, be ascribed to the spin polarization of the valence band ground state. Therefore, systems with n-type character should have the polarization defined by the minority carriers (in this case holes) at the valence band.

3.3 Modulation effects of strain fields on QR and QD systems

This section reports a discussion about the strain fields and confinement effects in QR and QD structures. For this part of the work we use the effective potential profile described in the section 2.4.2 to theoretically emulate the ring-shape confinement, simulating the electron and hole band structures by a multiband **k.p** calculation.

This work is also motivated by experimental measurements in QRs and QDs grown by our collaborators, where the composition and strain effects in this kind of nanostructures have been studied. In Fig. 3.12, we show the in-plane variation of the In-content along the radial QR coordinate as determined by [26]. We note that this variation changes the effective energy-gap and places the electron-hole pair closer to the inner QR rim where the In-content shows maximum values (see Fig. 3.13). By using the In-content estimation along the QR radial direction, displayed in Fig. 3.12, one may obtain the profile associated to the effective InAs/GaAs

energy-gap variation for InAs QRs as a function of the position, as shown in Fig. 3.14.
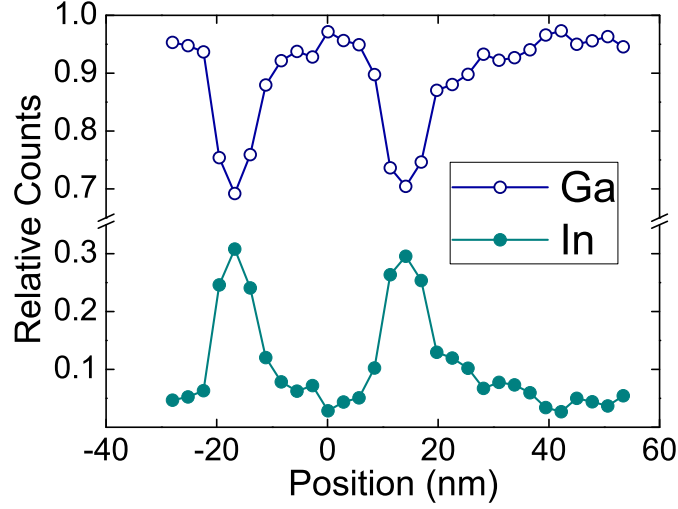
Figure 3.12: Indium and Gallium content estimations along the QR radial direction using TEM. The respective magnitudes of In and Ga were defined as relative counts: Cont(Ga) = Count(Ga)/(count(Ga) + Count(In)) and Cont(In) = Count(In)/(count(Ga) + Count(In)) [26].

In the sequence, we analyze how the shape of the QR potential profile affects the electronic structure and how this can be tuned by varying structural parameters such as size and strain field strength. The strain effects can be included into this Hamiltonian model by introducing the corresponding contribution of deformation potentials as described in the section 2.3.1 [27]. We shall consider the mean values of the strain tensor components within the QR rim, as obtained by the X-ray diffraction (Fig. 3.13). In order to contrast the electronic structure, with and without strain effects, we have performed the calculations for $\varepsilon_{\parallel} = 0$ and 1.37%, as shown in Fig. 3.13. The energy levels obtained as a function of QR radius are displayed in Fig. 3.15, where the relative effect of the strain field on the subband positions can be noted. Given the mass anisotropy and the difference of in-plane masses between the subbands, as described by the diagonal terms of the Hamiltonian $H_{i,i}$, the HH and LH levels approach each other as the radius grows. More drastic effects were obtained for an analogous variation of the effective QR width, as displayed in Fig. 3.16. However, it is difficult to characterize the actual degree of hybridization of the valence subbands through these figures, once the energy levels are mixed. Thus, it is necessary to calculate the character of these levels.

The main character of the valence ground state can be assessed by comparing the weight coefficients of the wavefunction expansion in Eq. (2.4.2). These coefficients have been displayed in Figs. 3.17(a) and 3.17(b), and labeled as $|\nu, m, n, l\rangle$, where ν represents either a HH or LH level (presented with lowercase letters in figures). The character of a given energy level may be-
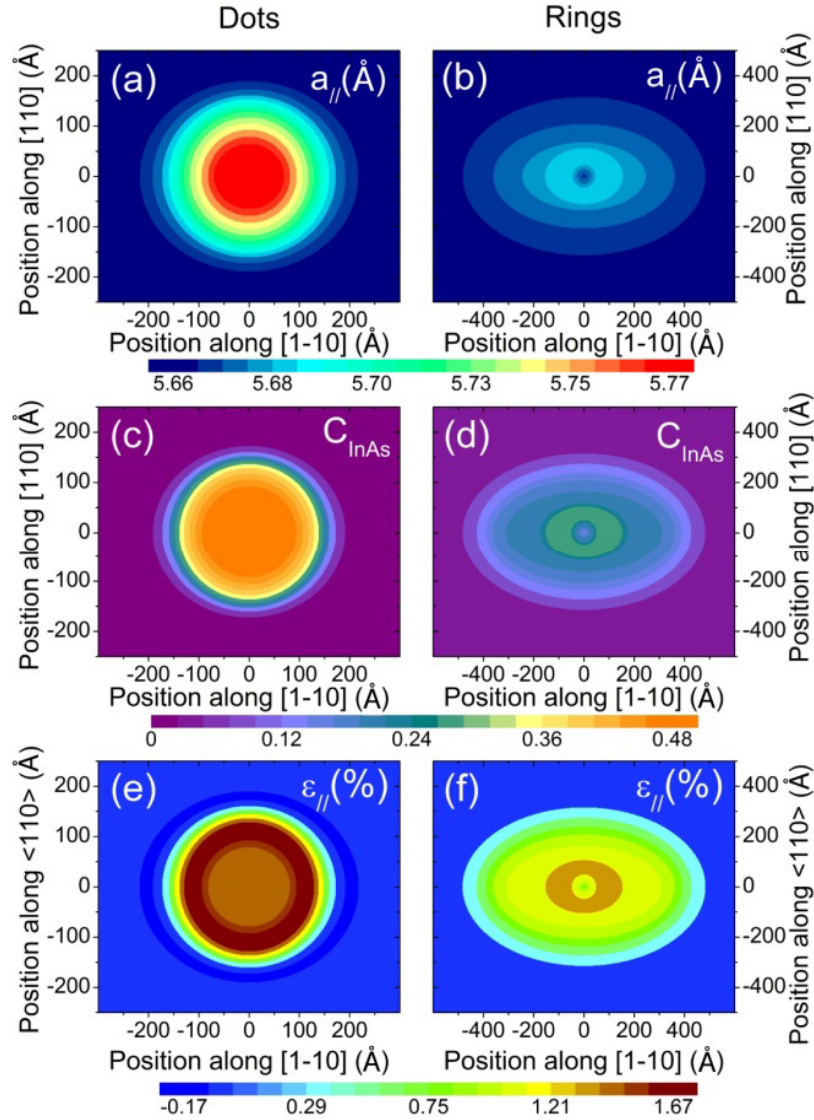
Figure 3.13: In-plane iso-lattice parameter projections, obtained by X-ray diffraction, for QD and QR samples are shown in panels (a) and (b), respectively. Panels (c) and (d) are representations of the In concentration for each iso-lattice parameter region from QDs and QRs. Elastic in-plane strain projections, obtained by considering the deviation from the measured lattice parameter to the relaxed alloy concentration are shown in panels (e) and (f) [26].

come hybridized due to inter-subband coupling. Furthermore, the character of the ground state has contributions from wavefunction components with different m. The expansion coefficients, in this case, show slight variation with radius within the range $8 - 19$ nm. However, contrasting differences appear by varying the value of the strain tensor component. The strained QR shows a valence band ground state with a significant HH character and an effective angular momentum $m = 0$. Yet, by relaxing the strain, the ground state attains higher values of the LH character and with an effective angular momentum $m = 1$. The interchange between hole characters in the valence band ground state and their modulation with the strain field has also been reported
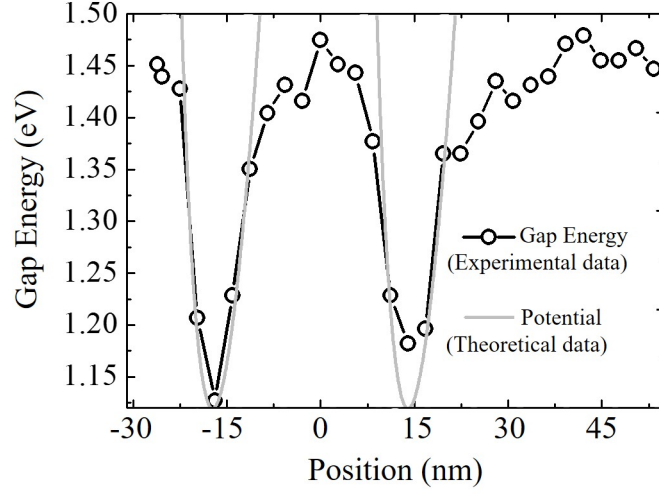
Figure 3.14: Adjustment of theoretical and experimental In-content obtained.
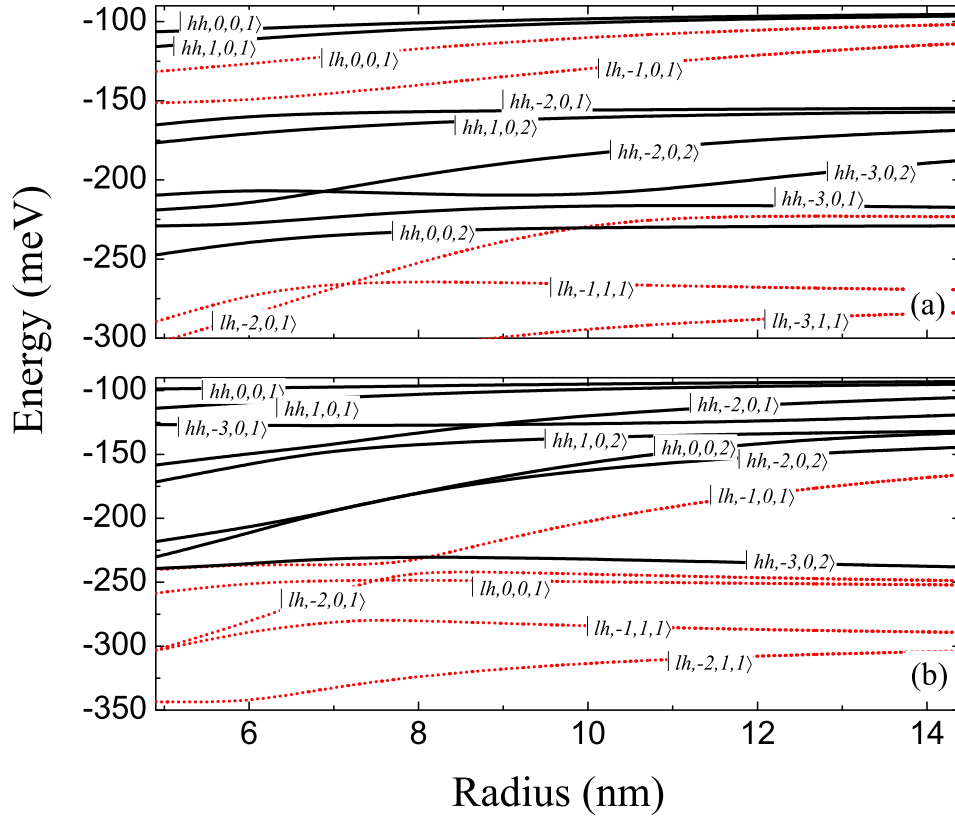
Figure 3.15: Energy levels of hole states as a function of the effective QR radius(R) for fixed values of the QR height ($L = 5$ nm), QR width, $\Delta r = \left(\frac{E_0}{a_2}\right)^{\frac{1}{2}} = 2.29$ nm, and in-plane strain value: (a) $\varepsilon_\parallel = 0$ and (b) $\varepsilon_\parallel = 1.37\%$. The dominant HH or LH characters of the energy states are indicated [26].

previously for self-assembled QDs [18] and may become an important tool for tuning anomalous magnetic properties in these nanostructures. It can be seen in Fig. 3.17(b), that the ground
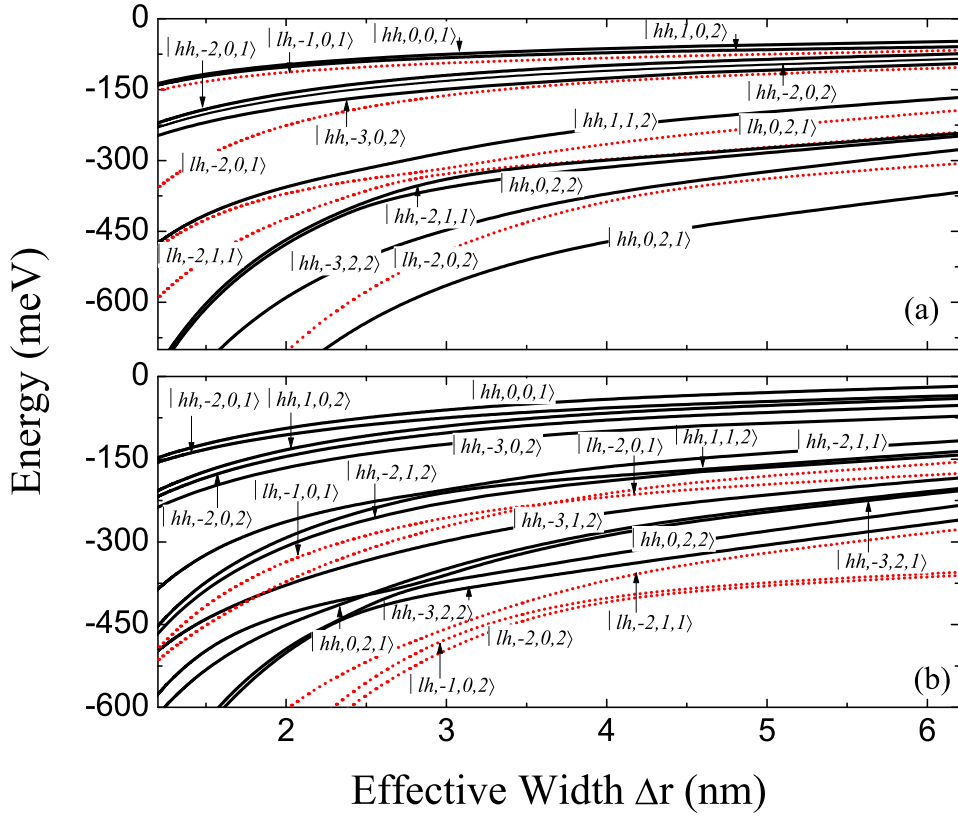
Figure 3.16: Energy levels of hole states as a function of the effective QR width, Δr, for fixed values of QR radius ($R = 14.75$ nm), QR height ($L = 5$ nm) and in-plane strain value: (a) $\varepsilon_{\parallel} = 0$ and (b) $\varepsilon_{\parallel} = 1.37\%$. The dominant HH or LH characters of the energy states are indicated [26].

state hybridization has been tuned by changing the QR width, Δr. In this case, the relaxation of the strain fields may lead to stronger hybridization and to the subsequent HH to LH crossing between ground state characters, when the QR width is reduced below 2 nm.

Scans on the samples show that lateral sizes of iso-lattice parameter regions are mainly symmetric for the QDs while a larger anisotropy is found for QRs along the [110] and [1$\bar{1}$0] directions. The iso-lattice parameter profile of QR shows an elongation in the [1$\bar{1}$0] direction [28]. The signature of such size anisotropy, being clearer in the transversal scans than in the longitudinal scans, may be ascribed to the highly strained condition in which buried QRs are subjected. The lateral size values for each fixed lattice parameter was directly obtained from transversal scans of reciprocal space profile width. This procedure leads to sizes consistent with both microscopy and spectroscopy findings.

Finally, the local in-plane strain projection maps can be also obtained from the definition, $\varepsilon_{\parallel} = (a_{\parallel} - a_{relaxed})/a_{relaxed}$, where $a_{\parallel}$ is the local in-plane lattice parameter from the maps in Figs. 3.13(a) and 3.13(b) and $a_{relaxed}$ is the bulk lattice parameter obtained from Vegard's law
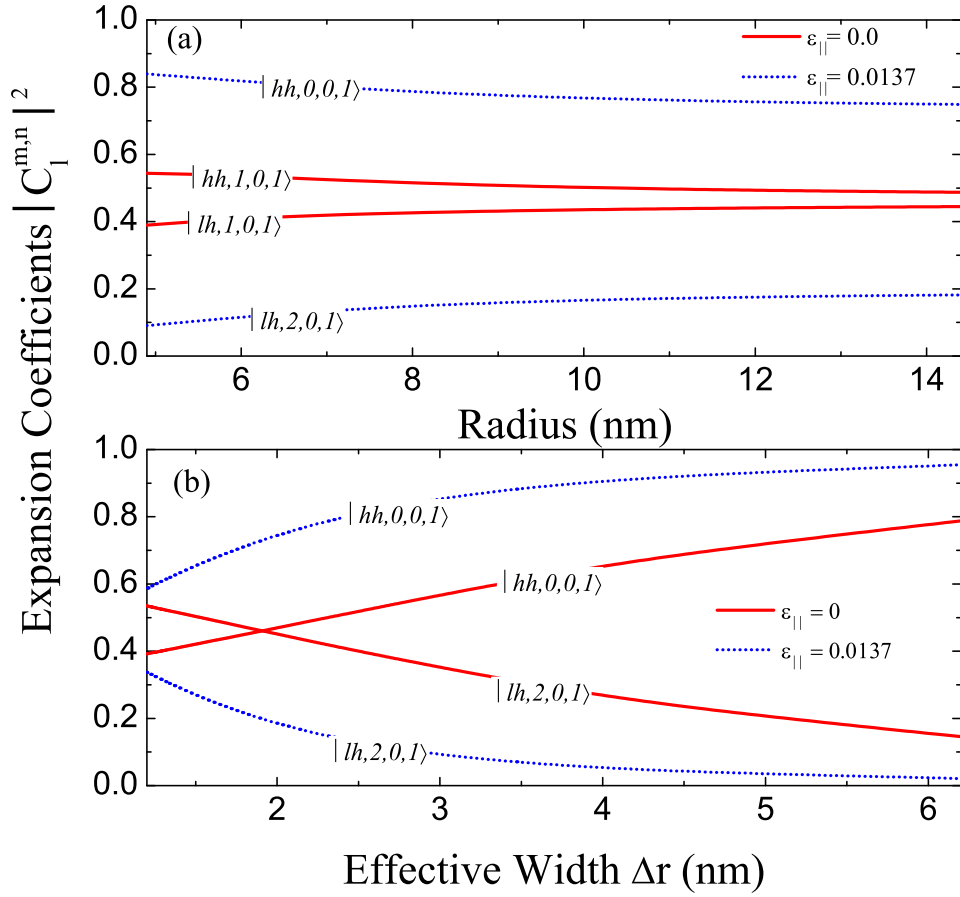
Figure 3.17: Main weight of expansion coefficients, $C_{l,n}^{m}$, for the valence band ground state when expanded in the set $|\alpha, m, n, l\rangle$, as a function of (a) the effective QR radius R, for fixed values of the QR width $\Delta r = 2.29$ nm and QR height $L = 5$ nm, and (b) the QR width Δr for fixed values of the radius $R = 14.75$ nm and QR height $L = 5$ nm. The figures show calculations with (dashed-lines) and without (solid-lines) strain field effects [26].

for the given InAs/GaAs concentration of Figs. 3.13(c) and 3.13(d). It can be noted, from the strain maps shown in Figs. 3.13(e) and 3.13(f), that the most strained region in QRs is closer to the internal radius whereas, in QDs, the maximum strained region occurs at an intermediate radius size.

Since the Indium diffusion coefficient is anisotropic, the QDs and QRs are usually elongated in the $[1\bar{1}0]$ direction with respect to $[110]$ (see Fig. 3.13(a) and 3.13(b)). Certainly, this asymmetry may generate built-in charge distribution which produces piezoelectricity as observed in "large" InAs/GaAs nanostructures and which may be ascribed to lattice mismatch between the materials [29–32]. A detailed study about asymmetries in QRs generated by growth process, in especial for elongation QR, will be presented in the section 4.3 of the next chapter.

The observation of strain field formation within the QRs and the characterization of the In-content distribution just presented may rise questions on their relative effects on the electronic

structure and, in particular, on the valence band structure where shape and size of the potential profile lead to stronger hybridization of the quantum states.

3.4   Conclusions

Our calculations presented in section 3.2 are in agreement with the experimental results obtained by collaborators, and the correlation between them are shown in [21]. The anomalous behavior of the PL peak energy at low temperature observed for both samples was ascribed to strain and localization effects, while the observed anomalous behavior of the electron-hole pair magnetic shift at low magnetic fields was associated to the increase in the exciton reduced mass due to the negative effective mass of the valence band ground state which results in the observation of negative magnetic shifts [33,34]. This leads to a peculiar reduction in the diamagnetic shift detected in the optical recombination of excitons. Yet, as also reported in Ref. [33], unusually large in-plane masses can also be found, and, as described here, even negative diamagnetic shifts could be expected. These additional effects can be ascribed to exciton localization in alloy imperfections.

The unambiguous polarization fluctuations as the magnetic field increases in the InGaAsN QW can be attributed to the spin dynamics during carrier relaxation at the conduction band [35]. We have observed that the polarization degrees for the N-containing samples are slightly higher than for N-free samples and the spin-dependent effects are stronger for wider QWs for both systems. In addition, we have shown that the spin polarization degree is dependent on the character of valence band ground state.

The correlation between theoretical and experimental results in section 3.3 allowed us to determine the profile of the effective confinement potential in the QR structure through the modulation of the QR composition. The verified reduction of the QR dimensions when the samples are capped, was associated to strain and composition effects. Besides, the presence of strain fields affects the electronic structure and this may tune the state hybridization of the valence band ground state, as found in our multiband calculation.

Bibliography

[1] W. Shan, W. Walukiewicz, J. W. Ager III, E. E. Haller, J. F. Geisz, D. J. Friedman, J. M. Olson, and S.R. Krutz, Phys. Rev. Lett. **82**, 1221 (1999).

[2] L. Grenouillet, C. Bru-Chevallier, G. Guillot, P. Gilet, P. Duvaut, C. Vannuffel, A. Million, and A. Chenevas-Paule, Apl. Phys. Lett. **76**, 2241 (2000).

[3] M.-A. Pinault and E. Tournié, Apl. Phys. Lett. **78**, 1562 (2001).

[4] Z. Pan, L. H. Li, Y. W. Lin, B. Q. Sun, D. S. Jiang, and W. K. Ge, Apl. Phys. Lett. **78**, 2217 (2001).

[5] S. Mazzucato, A. Erol, A. Teke, M.C. Arikan, R.J. Potter, N. Balkan, X. Marie, A. Boland-Thoms, H. Carrere, E. Bedel, G. Lacoste, C. Fontaine, and A. Arnoult, Physica E **17**, 250 (2003).

[6] T. Nuytten, M. Hayne, Bhavtosh Bansal, H. Y. Liu, M. Hopkinson, and V. V. Moshchalkov , Phys. Rev. B **84**, 045302 (2011).

[7] O. Rubel, M. Galluppi, S. D. Baranovskii, K. Volz, L. Geelhaar, H. Riechert, P. Thomas, and W. Stolz, J. Appl. Phys. **98**, 063518 (2005).

[8] R. Kudrawiec, M. Latkowska, M. Baranowski, J. Misiewicz, L. H. Li, and J. C. Harmand, Phys. Rev. B **88**, 125201 (2013).

[9] M. Latkowska, R. Kudrawiec, G. Sek, J. Misiewicz, J. Ibanez, M. Hopkinson, and M. Henini, Phys. Status Solidi C,**8**, 1655 (2011); M. Latkowska, R. Kudrawiec, G. Sek, J. Misiewicz, J. Ibanez, M. Hopkinson, and M. Henini, Appl. Phys. Lett. **98**, 131903 (2011).

[10] A. Polimeni, M. Capizzi, M. Geddo, M. Fischer, M. Reinhardt, and A. Forchel, Phys. Rev. B **63**, 195320 (2001).

[11] A. Polimeni, F. Masia, A. Vinattieri, G. Baldassarri Höger von Högersthal, and M. Capizzi, Appl. Phys. Lett. **84**, 2295 (2004).

[12] H. Carrère, A. Arnoult, A. Ricard, and E. Bedel-Pereira, J. of Crystal Growth, **243**, 295 (2002).

[13] T. Kageyama, T. Miyamoto, S. Makino, F. Koyama, and K. Iga, Jpn. J. Appl. Phys. **38**, L298 (1999).

[14] G. E. Pikus and G. L. Bir, Sov. Phys. Solid. State **1**, 136 (1959).

[15] S. Adachi, J. Appl. Phys. **53**, 8775 (1982).

[16] Yu. F. Biryulin, N. V. Ganina, M. G. Mil'vidskii, V. V. Chaldyshev, and Yu. V. Shmartsev, Sov. Phys. Semicond. (English Transl.) **17**, 68 (1983).

[17] I. Vurgaftman and J. R. Meyer, J. Appl. Phys. **94**, 3675 (2003).

[18] J. Ibañez, R. Kudrawiec, J. Misiewicz, M. Schmidbauer, M. Henini, and M. Hopkinson, J. Appl. Phys. **100**, 093522 (2006).

[19] L. Xu, D. Patel, C. S. Menoni, J. Y. Yeh, L. J. Mawst, and N. Tansu, Appl. Phys. Lett. **89**, 171112 (2006).

[20] E. Margapoti, Fabrizio M. Alves, S. Mahapatra, T. Schmidt, V. Lopez-Richard, C. Destefani, E. Menendez-Proupin, Fanyao Qu, C. Bougerol, K. Brunner, A. Forchel, G. E. Marques, and L. Worschech, Phys. Rev. B **82**, 205318 (2010).

[21] V. Lopes-Oliveira, L. K. S. Herval, V. Orsi Gordo, D. F. Cesar, M. P. F de Godoy, Y. Galvão Gobato, M. Henini, A. Khatab, M. Sadeghi, S. Wang, and M. Schmibauer, Journ. of Appl. Phys. **116**, 233703 (2014).

[22] Y. P. Varshni, Physica **34**, 149 (1967).

[23] I. Vurgaftman, J. R. Meyer, and L. R. Ram-Mohan, J. Appl. Phys. **89**, 5815 (2001).

[24] A. Polimeni, M. Capizzi, M. Geddo, M. Fischer, M. Reinhardt, and A. Forchel, Appl. Phys. Lett. **77**, 2870 (2000).

[25] L. K. Castelano, D. F. Cesar, V. Lopez-Richard, G. E. Marques, O. D. D. Couto Jr., F. Iikawa, R. Hey, and P. V. Santos, Phys. Rev. B **84**, 205332 (2011).

[26] M. D. Teodoro, A. Malachias, V. Lopes-Oliveira, D. F. Cesar, V. Lopez-Richard, G. E. Marques, E. Marega Jr., M. Benamara, Y. I. Mazur, and G. J. Salamo, J. Appl. Phys. **112**, 014319 (2012).

[27] G. Fishman, Phys. Rev. B. **52**, 11132 (1995).

[28] L. Villegas-Lelovsky, M. D. Teodoro, V. Lopez-Richard, C. Calseverino, A. Malachias, E. Marega Jr., B. L. Liang, Yu. I. Mazur, G. E. Marques, C. Trallero-Giner, and G. J. Salamo, Nanoscale Res. Lett. **6**, 56 (2010).

[29] M. Hanke, Yu. I. Mazur, E. Marega Jr. Z. Y. AbuWaar, G. J. Salamo, P. Schäfer, and M. Schmidbauer, Appl. Phys. Lett. **91**, 043103 (2007).

[30] J. M. García, D. Granados, J. P. Silveira, and F. Briones, Microelectronics Journal **35**, 7 (2004).

[31] J. A. Barker, R. J. Warburton, and E. P. O'Reilly, Phys. Rev. B **69**, 035327 (2004).

[32] R. J. Warburton, C. Schulhasuer, D. Haft, C. Schäflein, K. Karrai, J. M. García, W. Shoenfeld, and P. M. Petroff, Phys. Rev. B **65**, 113303 (2002).

[33] S. Tomic and E. P. O'Reilly, Phys. Rev. B **71**, 233301 (2005).

[34] A. Lindsay and E. P. O'Reilly, Phys. Rev. Lett. **93**, 196402 (2004).

[35] L. Fernandes dos Santos, Yu. A. Pusep, L. Villegas-Lelovsky, V. Lopez-Richard, G. E. Marques, G. M. Gusev, D. Smirnov, and A. K. Bakarov, Phys. Rev. B **86**, 125415 (2012).

Chapter 4

EXTERNAL FIELDS AND ASYMMETRY EFFECTS IN 0D STRUCTURES

In this chapter, we will focus on external fields and asymmetry effects in 0D nanostructures, in especial QRs. We start the chapter introducing the QR geometry and the external fields in section 4.1, then we analyze the effects of a perpendicular magnetic field in the section 4.2. In section 4.3, we present a systematic study of asymmetry effects in QRs and finish the chapter discussing the bright-to-dark transition found through the simulation of elongated QD-QR stacked structure in section 4.4.

4.1 Introduction

The QR geometry has long been a useful tool for the observation of interference effects in electron trajectories. The observation of AB effect on the excitonic response in this geometry along with the appearance of localized defects during the growth processes [1] demand theoretical studies of their mutual impact on the optical response in magnetic fields.

The study of magnetic fields and asymmetry effects on QR electronic properties is the proposal of this chapter. Some works have portrayed these effects separately in less complex systems [2]. It is well known that these effects, separately, can considerably change the QR properties, either by breaking degeneracies, such as the Zeeman splitting, or by symmetry breakdown caused by deformed QR shapes. One may note that, during the growth process,

the strain effects, discussed in the previous chapter, are responsible for the generation of geo-metric asymmetries (deformations). Moreover, the addition of an in-plane external electric field can also be a way to introduce external asymmetries, as we will see in what follows.

Here, we discuss the effect of a magnetic field applied along the growth direction of the cir-cularly symmetric QR. After that, we describe how the QR shape affects its electronic structure. And finally, we use the presence of an in-plane electric field or a spatial asymmetry in the QR topology as arguments to find the appropriate conditions for the observations of the AB effect in neutral particles. [3–6].

4.2   Magnetic fields in confined states in 0D traps (QR)

We will start the study of the effects of external fields in 0D structures with a magnetic field applied along their growth direction. This is mathematically simple, once the model described in the section 2.4.2, already includes this field explicitly within $\omega^*_{c(e/h)} = eB/\mu^*_{(e/h)}$. The effects of the magnetic field applied along the z direction in symmetric QDs and QRs are well known and were already studied by the author of this thesis [7]. In this section, we will just remark some of these effects.

The conduction band electronic structure in Fig. 4.1 shows how the Zeeman contribution, introduced by the last term in the Hamiltonian of the Eq. (2.25), affects the levels once the magnetic field is non zero. In Fig. 4.1, we see the behavior of the levels when the magnetic field is increased. In this figure, the Zeeman splitting is observed for non-zero magnetic fields ($B \neq 0$) in colors, red and blue, representing the spins up and down, respectively, while the black lines represent the average value between them.

Looking now at the valence band, we can see in Fig. 4.2 how the energy levels would look like for HH and LH when they do not interact with each other. Once we consider that there is no interaction between states, all the levels presented in Fig. 4.2 cross each other and are pure, what allows us precisely identify the levels through their characters. The states that contribute to the formation of the ground state are colored to help with their identification. However, we know that the HH and LH should interact with each other, thus the electronic structure for the valence band is not exactly like the one presented in Fig. 4.2. So, we turn on the interaction between the levels, as presented in Fig. 4.3(a). Now, we cannot identify precisely the levels, once the interactions turn them hybrid. This is seen in Fig. 4.3(b) for the
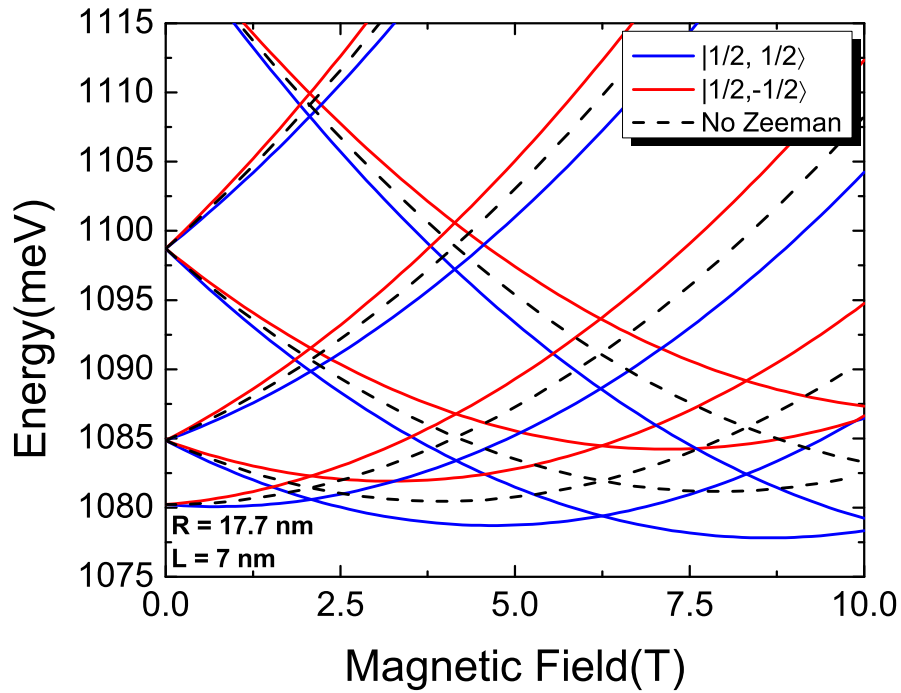
Figure 4.1: Conduction band over magnetic field: spin up (blue lines), spin down (red lines) and without Zeeman effects (black dashed lines).
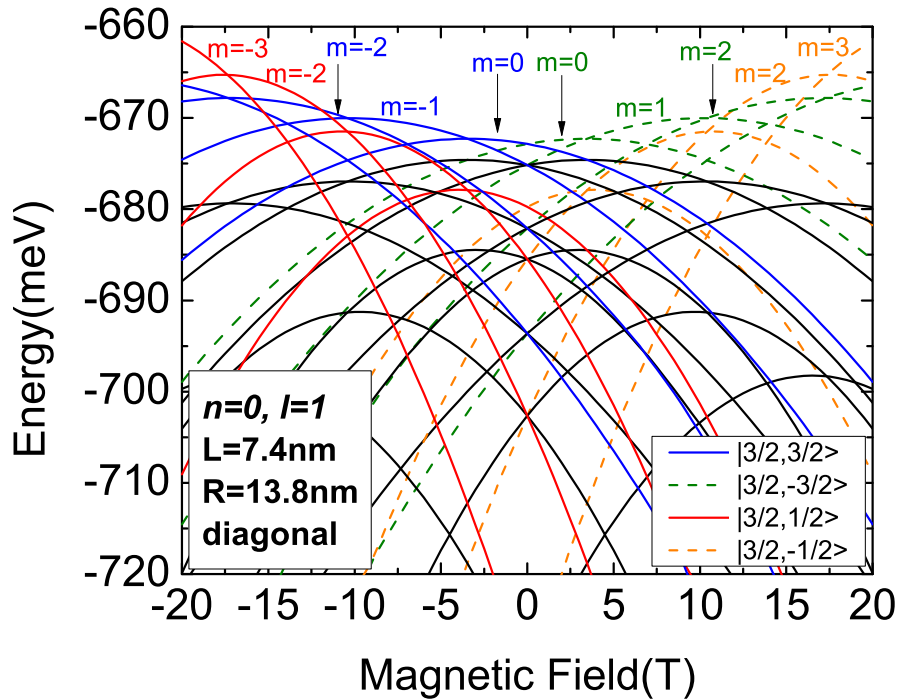
Figure 4.2: First valence band levels for non hybrid circularly symmetric QR showing the main character of the ground state.

ground state coefficients. The high level of hybridization leads to character change, mainly, close to zero field, where the ground state becomes more LH-like, and for high fields, where it is more HH-like. In the next section, we keep the QR configuration: radius, height and width
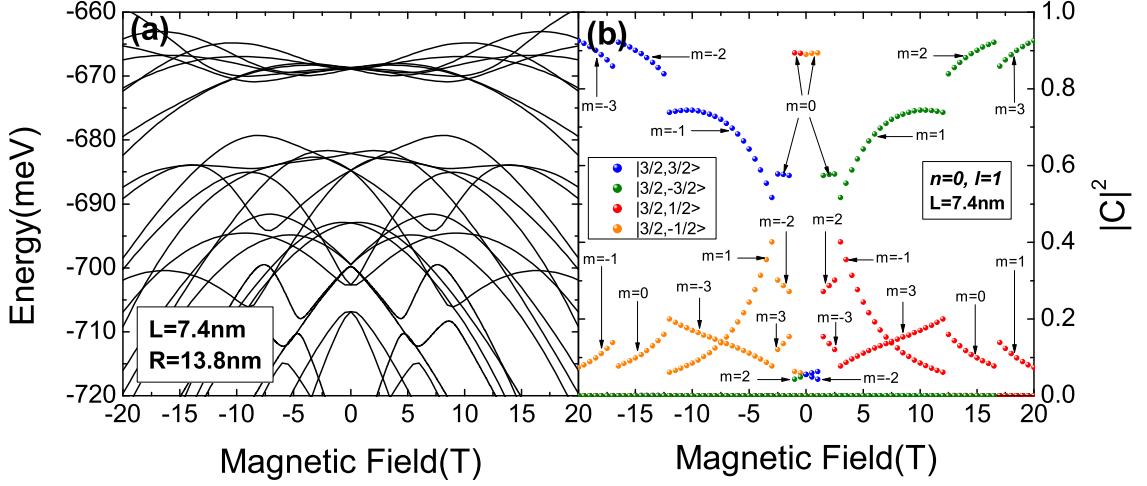
Figure 4.3: (a) Valence band electronic structure for circularly symmetric QR and its (b) ground state coefficients.

and include the asymmetry effects modifying the model for the potential profile and observe what happens to the QR electronic structure.

4.3 Asymmetry effects on conduction and valence electronic states of QRs

In this section, we study the asymmetry effects on the electronic structure of a QR under a perpendicular magnetic field. As cited before, some works have already shown the effects of asymmetries in QRs conduction band [2]. However, these effects in the valence band are rarely studied. Here, we present a systematic study of asymmetry and magnetic field effects in QRs, within a **k.p** formalism. We performed electronic structure calculations of the conduction and valence band for different kind of deformations observed in QRs samples, as shown in Fig. 4.4. The model used here allows modulate the confinement shape in a fairly easy way. The angular momentum hybridization is characterized for different field intensity and asymmetries. The coupling of unperturbed and symmetric states defines the potential appearance of crossings and new anticrossings in the electronic structure as function of field and structural parameters. We aim to analyze some possible results of deformation in QRs caused by growth parameters
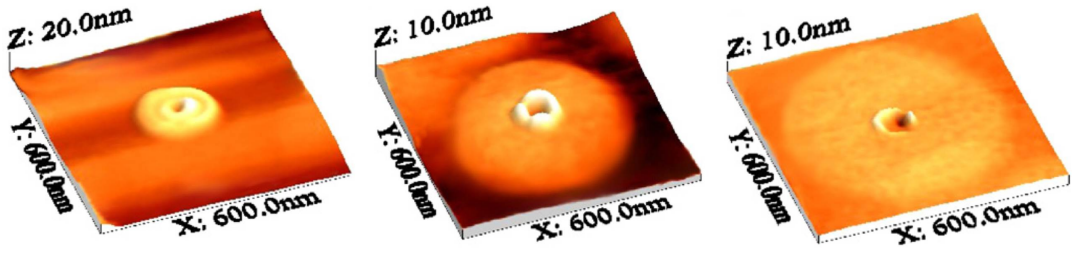
Figure 4.4: Examples of deformed QRs from images obtained experimentally by AFM [8].

like temperature, deposition time, and annealing. Theoretically, the deformations are attained through addition of a term on the potential confinement $V(\rho, \varphi)$.

The first kind of deformation we studied, DR1, was emulated by the addition of $\delta \rho \cos(\varphi)$, transforming Eq. 2.72 in

$$V_1(\rho, \varphi) = \frac{a_1}{\rho^2} + a_2 \rho^2 - 2\sqrt{a_1 a_2} + \delta \rho \cos(\varphi) \qquad (4.1)$$

where δ determines the magnitude of the deformation. As a result, we have the transformation of the undeformed QR potential profile from Fig. 4.5(a) to Fig. 4.5(b). Note that comparing
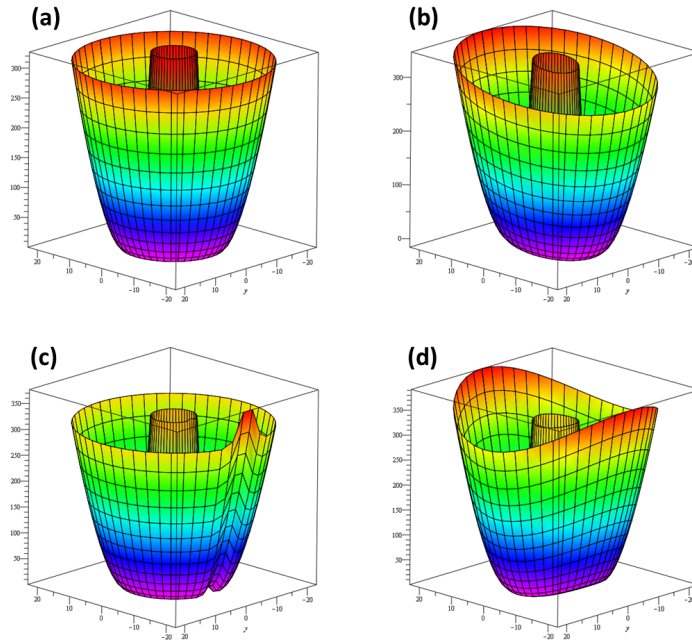
Figure 4.5: Potentials profiles for (a) circularly symmetric QR, and QRs deformed by addition of the terms (b) $\delta \rho \cos(\varphi)$, (c) $\delta \rho^2 exp\left[\frac{-(\varphi - \pi)^2}{2\eta^2}\right]$, and (d) $\delta \rho^2 \cos^2(\varphi)$.

these two figures, DR1 undergoes a deformation due an electric field along x ($\varphi = 0$). The second kind of deformation analyzed, DR2, is a local deformation emulating a pinched QR

63

whose potential confinement is given by

$$V_2(\rho, \varphi) = \frac{a_1}{\rho^2} + a_2\rho^2 - 2\sqrt{a_1 a_2} + \delta\rho^2 exp\left[\frac{-(\varphi - \pi)^2}{2\eta^2}\right] \tag{4.2}$$

and represented in Fig. 4.5(c). And, the third kind of deformation, DR3, is an elongated or elliptical QR displayed in Fig. 4.5(d) and given by

$$V_3(\rho, \varphi) = \frac{a_1}{\rho^2} + a_2\rho^2 - 2\sqrt{a_1 a_2} + \delta\rho^2 cos^2(\varphi). \tag{4.3}$$

In these terms, φ is the azimuthal angle and η is the effective angular width of the perturbation DR2. The three cases will be analyzed in this section, however, the third one will be used together with other effects and studied in more detail in the next section and in chapter 5.

For DR1 case, the calculation of the matrix elements for the new potential provides the selection rules for angular momentum, $m' = m \pm 1$, as shown in Appendix A. The effect of coupling states with the given angular momentum difference can be observed in Figs. 4.6(b) and 4.6(c). Here, the conduction band electronic structure for a DR1 profile is plotted in black lines and contrasted with a circularly symmetric QR (Fig. 4.5(a)) in red lines. The effect of the asymmetry is the appearance of anticrossings following the calculated selection rule. When $\delta = 10$ meV, in Fig. 4.6(b), it is easy to see the anticrossings between $m = 0$ and $m = \pm 1$. Yet, another anticrossing can be observed between $m = -1$ and $m = 1$, due to the mixing among these states and $m = 0$. Now, m is no longer a good quantum number. This becomes more evident when we increase the value of δ up to 20 meV in Fig. 4.6(c). The anticrossings also appear in more energy levels, showing that the hybridization is directly dependent on δ. In addition, one may note that the perturbation also shifts the ground state energy, as can be observed in Figs. 4.6(b) and 4.6(c) where a deformed QR (black lines) is contrasted with an undeformed (red lines). Yet, the ground state predominant character remains the same, independent of the δ value, as seen in Figs. 4.6(d), 4.6(e) and 4.6(f).

Looking at the valence band, in Fig. 4.7, the main effect of hybridization is clearly observed in the character graph, Fig. 4.7(b), where we note for low magnetic fields, that the ground state changes character within the range between 1.5 and 2.5 T.

A comparison between Figs. 4.3(b) and 4.7(b), shows that in this interval the blue (HH up) and green (HH down) colors in Fig. 4.3(b), give way to orange (LH down) and red (LH up) ones in Fig. 4.7(b), respectively. This means that this asymmetry may change the valence band
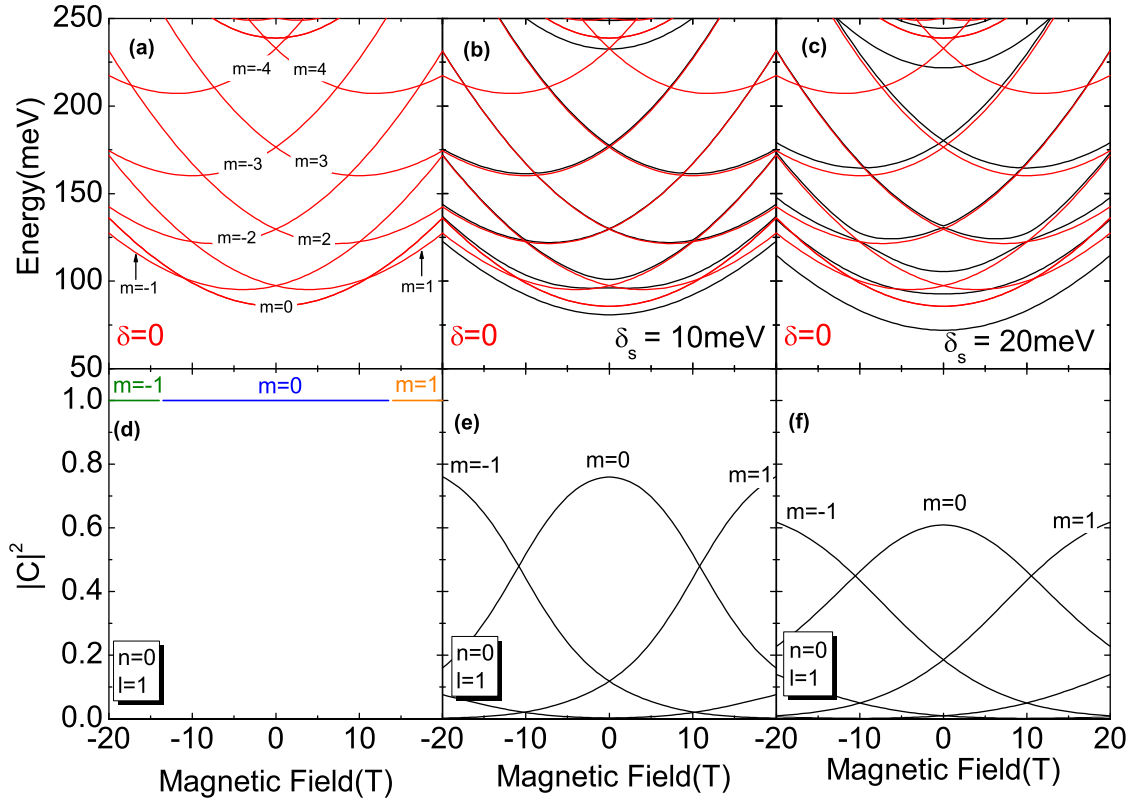
Figure 4.6: (upper panels) Lower conduction band states and (lower panels) its corresponding ground state coefficients for QR deformed by $\delta\rho cos(\varphi)$, comparing $\delta = 0$ to non vanishing δ values. The main character of the states are shown.
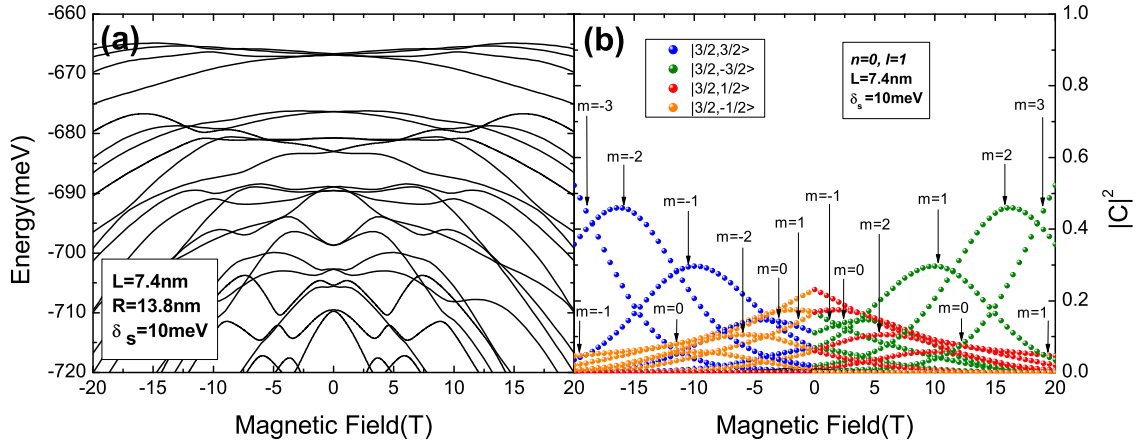
Figure 4.7: (a) Valence band electronic structure for a deformed QR by $\delta\rho cos(\varphi)$ and its (b) ground state coefficients.

ground state character depending on the magnetic field value.

The effect of the electric field along x, seen now in the wavefunction of DR1 was found by plotting the behavior of the wave function $|\Psi_{n,m,l}|^2$, Fig. 4.8(a), and the orbital, Fig. 4.8(b) for the valence band, at $\mathbf{B} = 20$ T. One may note that the wave function is dependent on φ and has a minimum of intensity for $\varphi = 0$, what corresponds to the shape of the orbital in Fig. 4.8(b).
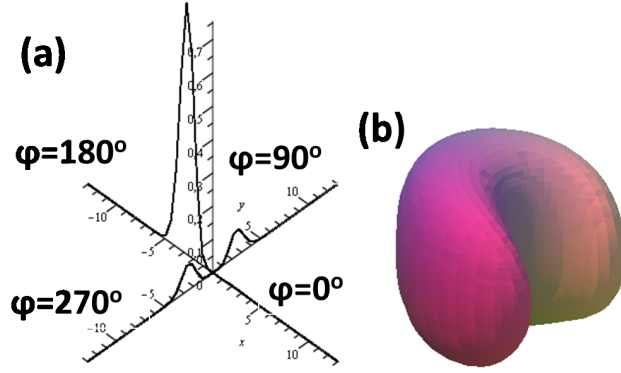
Figure 4.8: (a) 3D wave function for $\delta\rho cos(\varphi)$ case, and (b) valence band electronic orbital at $B = 20$ T.

Contrasting the electronic orbital in this figure with the first orbital in Fig. 2.8, we observe that the presence of this asymmetry promotes circular symmetry breaking.

The second kind of deformation studied, DR2, leads to a different selection rules of the potential profile matrix element, $m' = m \pm 0, 1, 2, ...$ In this case, all states are mixed with each other, what can be seen in the conduction band electronic structure shown in Fig. 4.9(a). Here the ground state does not present crossings with other levels, it is due a mix of ground state and its neighboring states, leading to character changing as the magnetic field grows, as shown in Fig. 4.9(b).
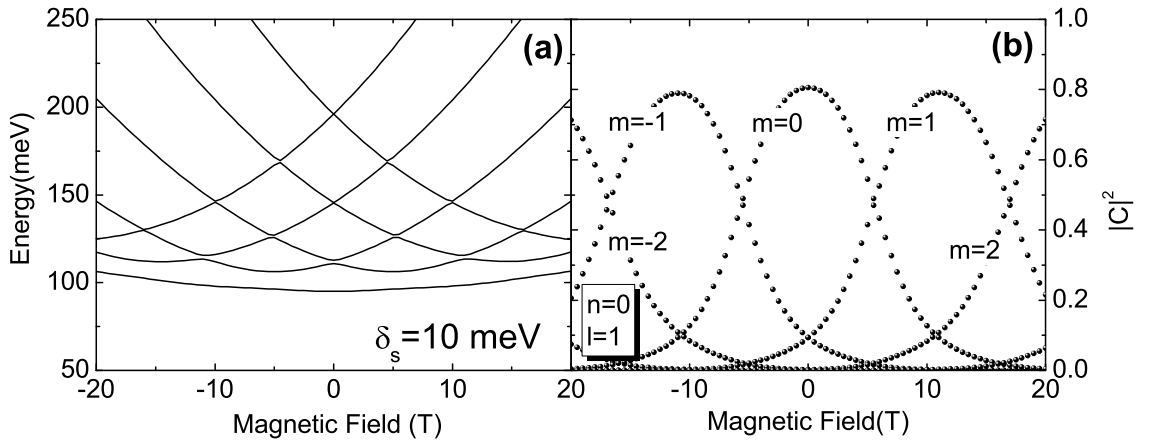
Figure 4.9: (a) Conduction band electronic structure modified by $\delta\rho^2 exp\left[\frac{-(\varphi-\pi)^2}{2\eta^2}\right]$ term, and (b) its corresponding ground state coefficients.

The valence band electronic structure for DR2 case, Fig. 4.10(a), presents a very similar behavior compared to Fig. 4.3(a), but in Fig. 4.10(a) it is possible to see new anticrossings caused by the extra mixing of levels. Furthermore, a comparison between Figs. 4.3(b) and 4.10(b) shows that the ground state has the same predominant character, but in the regions where the
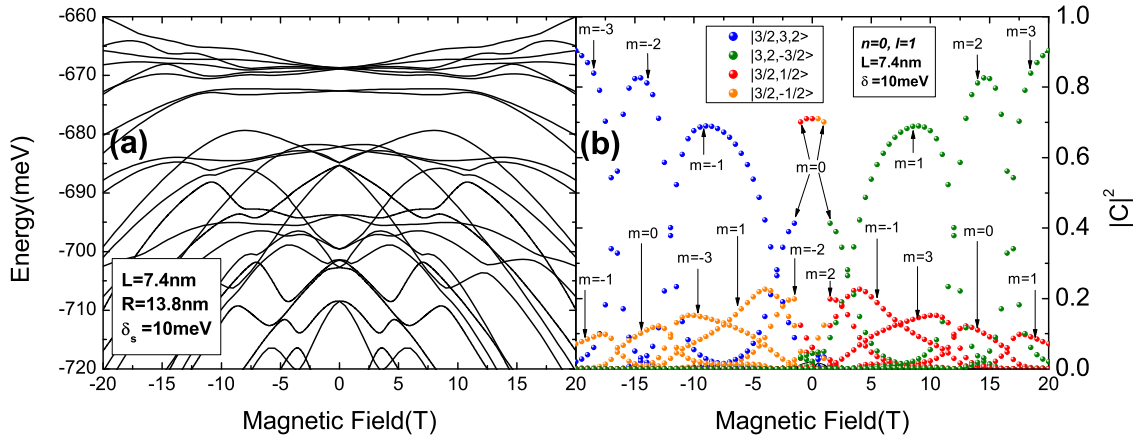
Figure 4.10: (a) Valence band electronic structure for a deformed QR by $\delta \rho^2 exp\left[\frac{-(\varphi - \pi)^2}{2\eta^2}\right]$ and its (b) ground state coefficients.

crossings became anticrossings, due to symmetry breakdown, there is no discontinuity of the coefficients anymore, turning the character transitions smooth. The wave function and electronic orbital for the valence band DR2 at $B = 20$ T, are presented in Fig. 4.11. The orbital has a "pinched" region at $\varphi = 0$, and is enough to break the symmetry.
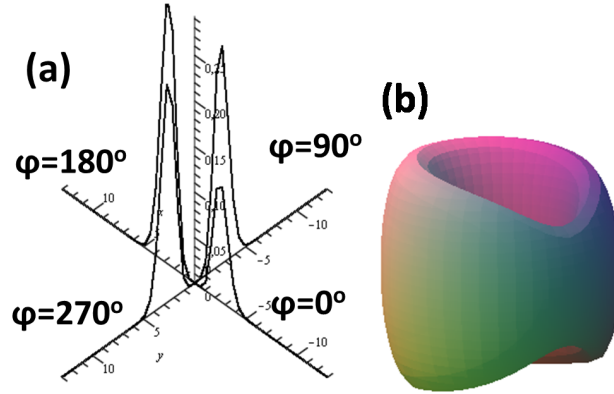
Figure 4.11: (a) 3D wave function for $\delta \rho^2 exp\left[\frac{-(\varphi - \pi)^2}{2\sigma^2}\right]$ case, and (b) valence band electronic orbital at $B = 20$ T.

Finally, for the last kind of deformation we analyzed, DR3, the selection rule $m' = m \pm 0, 2$ was obtained for the asymmetry term. Following this selection rule, Fig. 4.12(a) shows the anticrossings arising from the levels coupling in the conduction band. The most relevant one appears at $B = 0$ T and is the result of coupling between states $m = -1$ and $m = +1$. Since $m = 0$ does not couple to $m = -1$ or $m = +1$, we observe discontinuities in the ground state coefficients plotted in Fig. 4.12(b).

However, it is interesting to note that the valence band ground state for DR3 case should
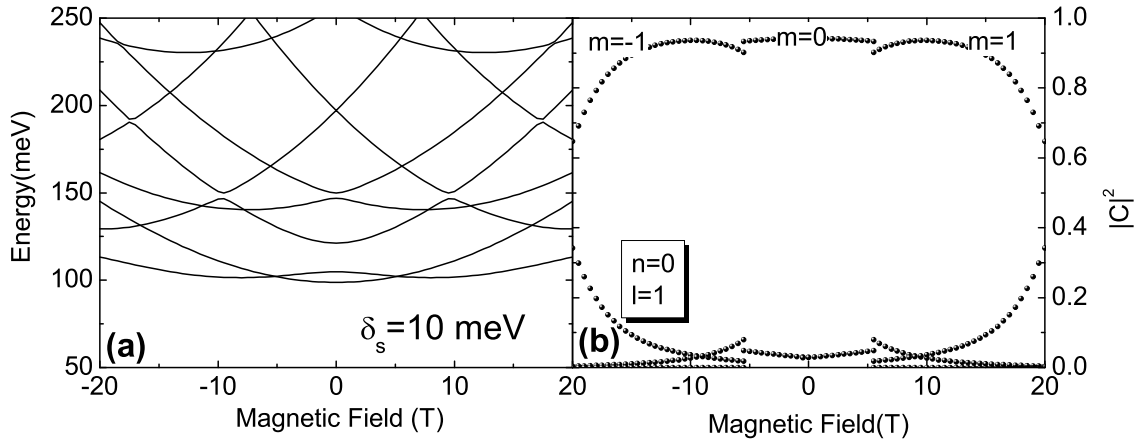
Figure 4.12: (a) Conduction band electronic structure modified by $\delta\rho^2 cos^2(\varphi)$ term, and (b) its corresponding ground state coefficients.

not present crossings with any other state due to the asymmetry. The intrinsic hybridization of the valence band and asymmetry effects together promote couplings strong enough to open anticrossings between the ground state and other states. Another interesting effect, typical of this kind of deformation, is present in Fig. 4.13(b). The ground state shows predominantly odd character on the entire interval of magnetic field studied, while in the previous kind of deformations there were interchanges between odd and even characters. It may be due to the strong effect of the deformation potential DR3 on a heavy mass particle (hole).
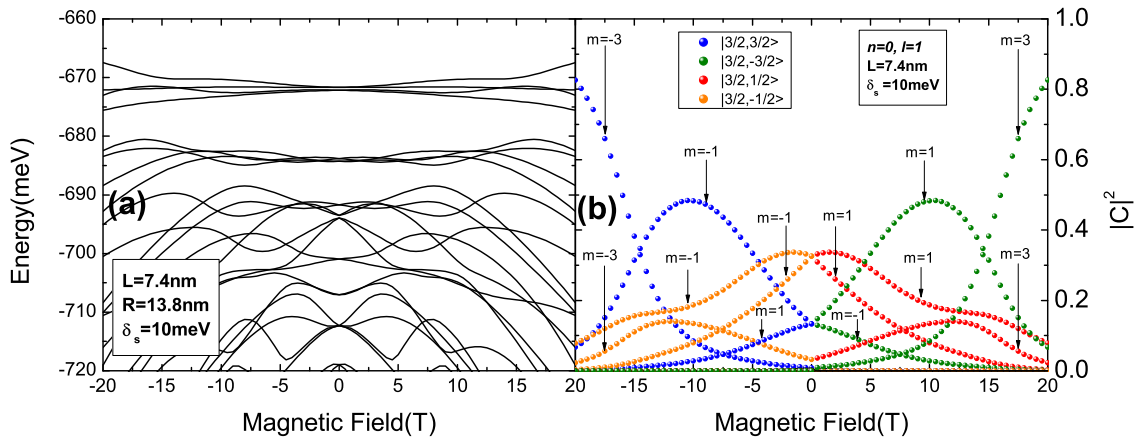
Figure 4.13: (a) Valence band electronic structure for a deformed QR by $\delta\rho^2 cos^2(\varphi)$ and its (b) ground state coefficients.

The wave function and valence band electronic orbital for this kind of deformation were plotted for different values of B in Fig. 4.14. The wave function amplitude in $\varphi = 0$ and $\varphi = 180°$ decreases as the magnetic field increase, vanishing for $B = 20$ T, what reflects on the orbital figure.

68
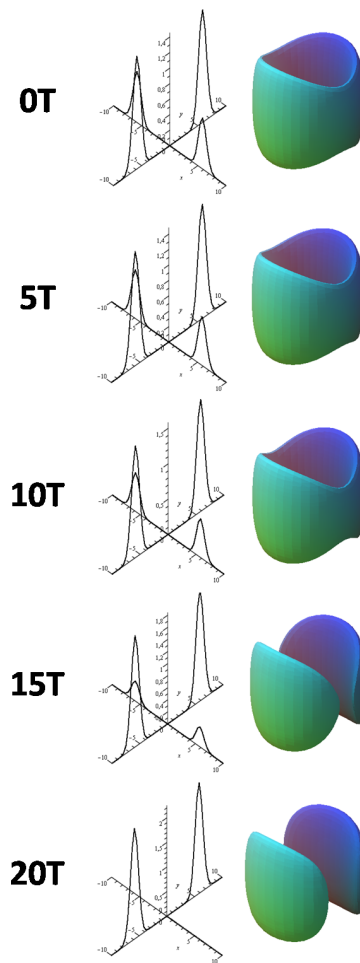
Figure 4.14: Valence band electronic orbitals for the ground state for different magnetic field values.

The results presented in this section show that the asymmetries found in QRs lead to visible symmetry breaking and will have an impact on the optical transitions. Shifts in energy values that affect the optical response and may cause a changing of the valence band ground state character from HH to LH. These shifts can be observed experimentally by photoluminescence spectrum.

4.4 Modulation effects of strain fields in elongated QD-QR stacked

The system studied in this section consists in a hybrid structure where InGaAs/GaAs QRs are grown over a vertical superlattice of laterally aligned InGaAs/GaAs QDs. Again, this analysis was motivated by the experimental results obtained by our collaborators trying to find out

their correlation with strain effects. The samples of coupled QD-QR chains were grown in an MBE chamber on GaAs [001] substrates [9, 10], and are composed of multiple layers of $In_{0.4}Ga_{0.6}As$ QDs separated by capping GaAs barriers and the top layer consisting of InGaAs QRs, are displayed in the AFM images in Fig. 4.15(a) and transmission electron microscope (TEM) in Fig. 4.15(b).
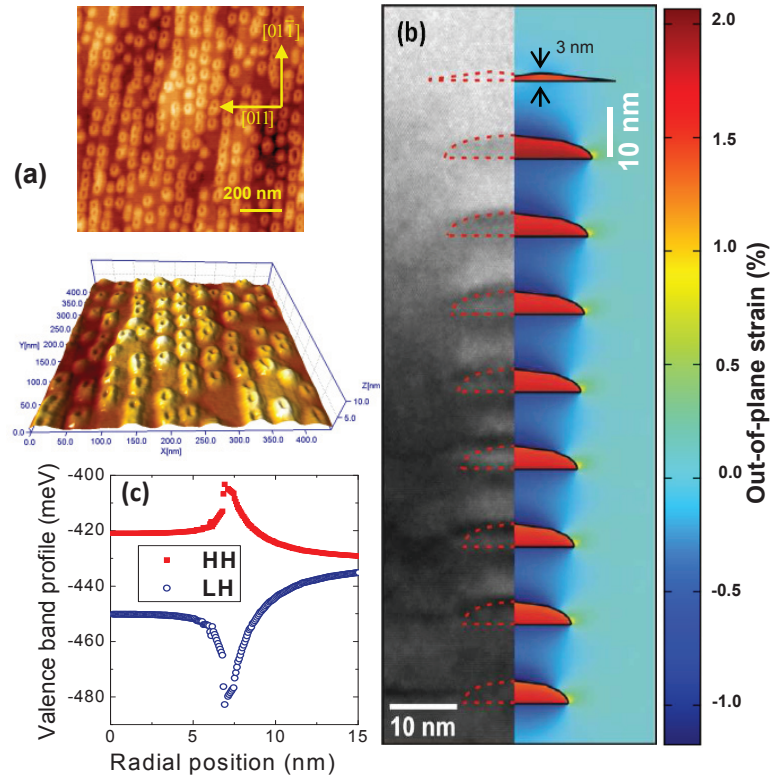
Figure 4.15: Panel (a): AFM image of the topmost layer containing QR chains grown on an $In_{0.4}Ga_{0.6}As$/GaAs(100) vertical QD superlattice. Panel (b): Left side: Multi-beam bright field TEM images of the hybrid multilayered sample used in this work. Right side: The FEM model of the QD/QR stack. For the out-of-plane strain in color code shown on the right, the blue colors are related to compressive (negative) out-of plane strain while green/yellow/red colors denote tensile (positive) out-of-plane strain. Panel(c): Calculated valence band deformation potential profiles for repulsive HH and attractive LH carriers in the QD region. The position axis represented in panel (c) depicts the coordinate along the radial [xy0] direction is on the vertical distance of 0.5 nm from the islands base plane, where $r = 0$ nm corresponds to the center of the QD [11].

The ring-shaped InGaAs nanostructures are clearly preserving the lateral ordering of the seeds consisting in InGaAs QDs chains along $[01\bar{1}]$ direction. The TEM in Fig. 4.15(b) indicates that the QRs have an average diameter of 31.5 ± 4.5 nm and a height of 3.0 nm, whereas the QDs have a smaller average diameter and bigger height. The QRs are larger than QDs due to the strong outer diffusion of materials during the QD-to-QR transformation growth process [10].

The QD and QR dimensions as well as morphologies were matched to the TEM observa-

tions and inserted into a GaAs matrix [12, 13]. A lateral cut from the finite-element method (FEM) results is shown in the right side of Fig. 4.15(b) superimposed to a TEM image of the QD-QR stack on the left side. The color code with green/yellow/red areas represents regions of the QDs and QRs subjected to tensile (positive) out-of-plane strain, due to pseudomorphic relaxation under in-plane compressive strain, while blue regions show areas subjected to compressive (negative) strain due to an in-plane lattice expansion associated to GaAs capping regions between QD layers. We have analyzed out-of-plane and in-plane strain profiles (considering the growth direction as [001]) along the QD stack.

The realistic strain profiles inside the QD and QR layers of our hybrid structure were obtained by our collaborators using a commercial software package to simulate nanostructures by FEM. The modeling is carried out ascribing main crystallographic axes to the FEM geometry axis. In our case, the [001] direction was ascribed to the z (growth/stack) axis, while in-plane [100] and [010] directions lie on the *x* and *y* coordinates (island base plane), respectively.

Strain profiles along selected directions are extracted from the FEM data and used for valence band deformation potential calculations as displayed in Fig. 4.15(c) for the QD according to Ref. [14]. Note the difference between the HH and LH energy shifts what would ultimately lead to difference on the character of the two hole confinement types. Since the HH states will be predominantly confined nearby the lateral QD boundary while the LH states occupy the internal QD region then, HH optical recombination will display a type-II character whereas LH recombination displays a type-I character. We will show, in this section that the light emission from the ground state excitons with type-II character is forbidden by selection rules, yet they have important influence in the detected PL emission. Although the strain fields built in the process of coherent formation of the QDs and QRs leads to a structural link between the stack layers, the distance between them inhibits the electronic coupling.

Besides the QD size difference of the dominant vertical stacking, our system is laterally anisotropic. The $In_{0.4}Ga_{0.6}As$/GaAs QDs are aligned in chain-like structures and so are the QRs in the top layer. In addition to the alignment along the $[01\bar{1}]$ direction, the QRs, like the $In_{0.4}Ga_{0.6}As$ QDs, are slightly elongated with an elliptical shape along this direction. The reason for elongation of the QDs and QRs is the anisotropic diffusion of In adatoms and the anisotropy of surface free energies and elastic strain distribution.

Here, we will provide a study of this anisotropy along with the effect of the external fields. This will include the optical analysis of this multilayer structure, considering the QD and QR

elongation of the potential profile presented in the section 2.4.2 and used to simulate electron and holes states in the section 3.3.

To analyze the effects of increasing eccentricity in the electronic structure we must consider the model described in the previous section by Eq. (4.3) and with the potential exhibited in Fig. 4.5(d). The eccentricity of the lateral confinement is given by $e = \sqrt{1 - a_2/(a_2 + \delta)}$ and is modulated by δ change. For the QD simulation, we set $a_1 = 0$ and $a_2 = 181.8$, while the QR was simulated with $a_1 = 147.5$ and $a_2 = 181.8$. Fig. 4.16 is an example of two profiles with different eccentricities for fixed QR parameters a_1 and a_2.
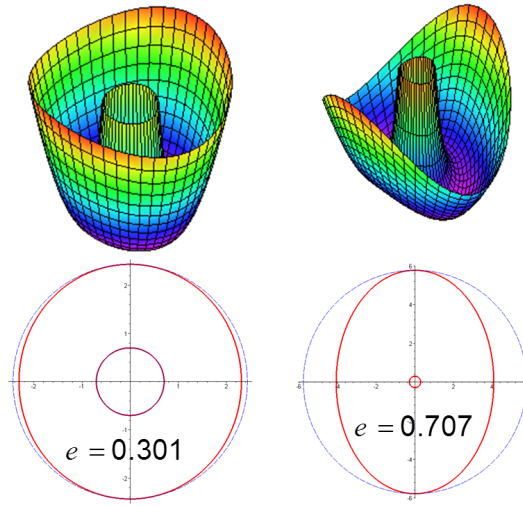
Figure 4.16: Different eccentricities caused by δ variation.

The eccentricity can also be emulated by QR parameters change. Fig. 4.17(a) presents the limits of a broad and a narrow QR and two values of the angle φ. The results for the expansion on the basis $\Phi^\delta(\rho, \varphi, z) = \sum_{n,m,l} C_{n,m,l} \psi_{n,m,l}^{HH}(\rho, \varphi, z)$ for this eccentric confinement, were already shown in Fig. 4.14. The corresponding energy levels and ground state weight coefficients $C_{n,m,l}$ for the two profiles described in Fig. 4.17(a) are plotted in Figs. 4.17(b) and 4.17(c), and 4.17(d) and 4.17(e), respectively.

Note, in Figs. 4.17(b) and 4.17(d), the oscillations of the ground state energy as the magnetic field increases. As expected, at certain critical fields, B_c, where $\sqrt{\hbar/eB_c} = R$, the ground state changes character transiting through branches of increasing values of the angular momentum m, as discussed in the previous section. The actual character of the ground state, determined by the weight coefficients of the linear expansion for $e \neq 0$ is shown in Figs. 4.17(c) and 4.17(e). For increased eccentricity, comparing Figs. 4.17(b) and 4.17(d), the ground state energy oscillation decreases while the angular momentum character remains oscillatory with the state
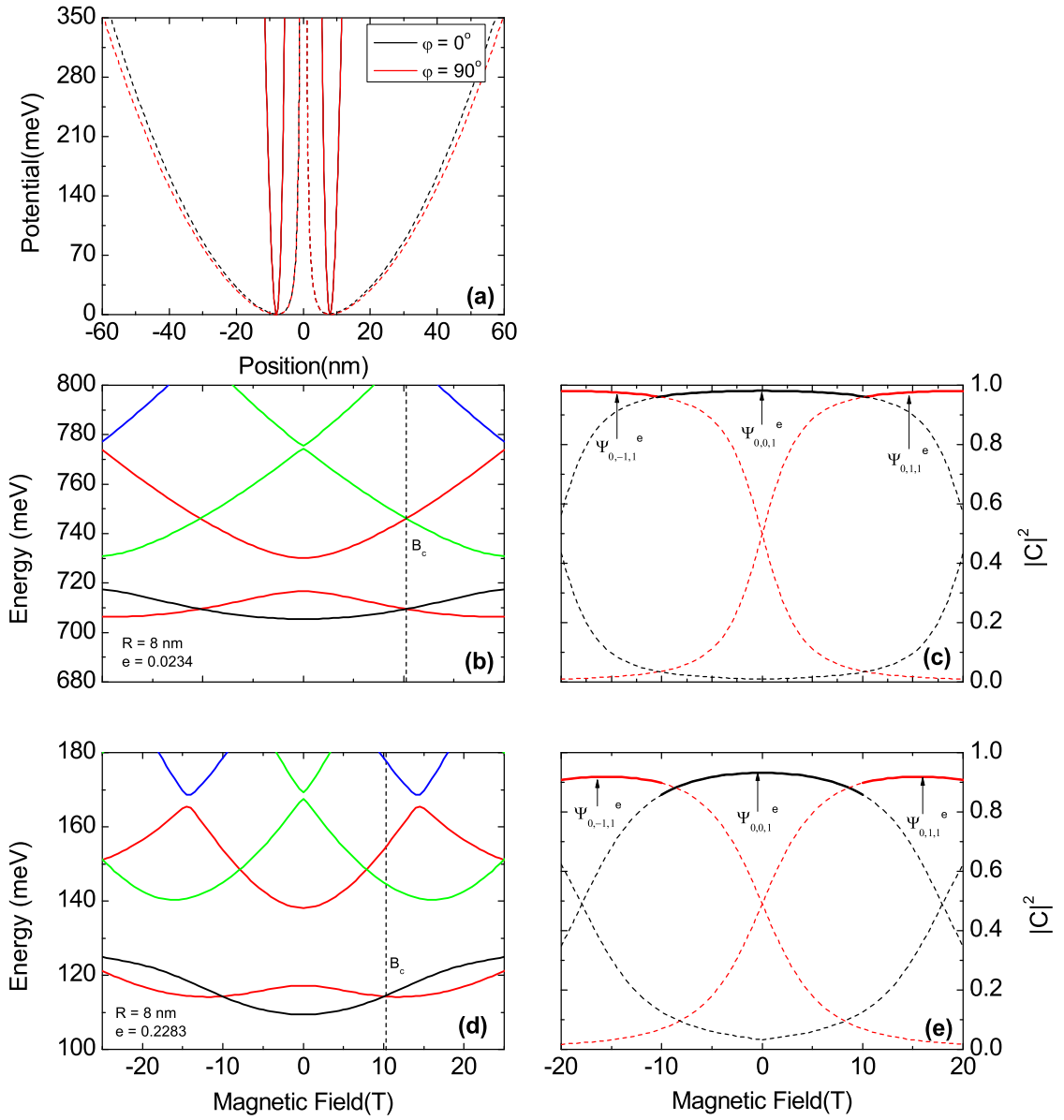
Figure 4.17: (a) Lateral QR profile for the two widths used in the simulations for two values of the angle φ. (b) Energy levels of an eccentric QR with $e = 0.0234$ versus magnetic field and (c), the corresponding conduction band coefficients of the ground state. (d) Energy levels of an eccentric QR with $e = 0.2283$ in a magnetic field and (e), the corresponding conduction band coefficients of the ground state.

hybridization increasing due to stronger inter-level coupling. However, even for highly eccentric confinements, the magnetic field cannot induce sudden change in the conduction band state character at a certain critical field that would lead to sharp differences in both the energy shift and the oscillator strength. This peculiarity can only be expected when analyzing the differences between the HH and LH confinement potential profiles and the tuning of the ground state character of the valence band with the magnetic field. As simulated from the strain profile, the valence band has a type-I character for the LH and type-II character for the HH, due to the strain

field modulation, as shown in Fig. 4.15(c). The details of the transformation of the valence band due to the combination of strain profiles, spatial, and magnetic confinements, as well as interdot coupling are given in a number of reported studies [15–17]. The magnetic tuning of the valence band character (HH or LH) in QDs has been already reported experimentally and confirmed theoretically [18, 19]. The physical explanation for the origin of the type-I to type-II transition with magnetic field in the valence band of III-V QDs was given in Ref. [15]. The in-plane potential profile used to theoretically simulate the effect displayed in Fig. 4.15(c) is shown in Fig. 4.18(a).
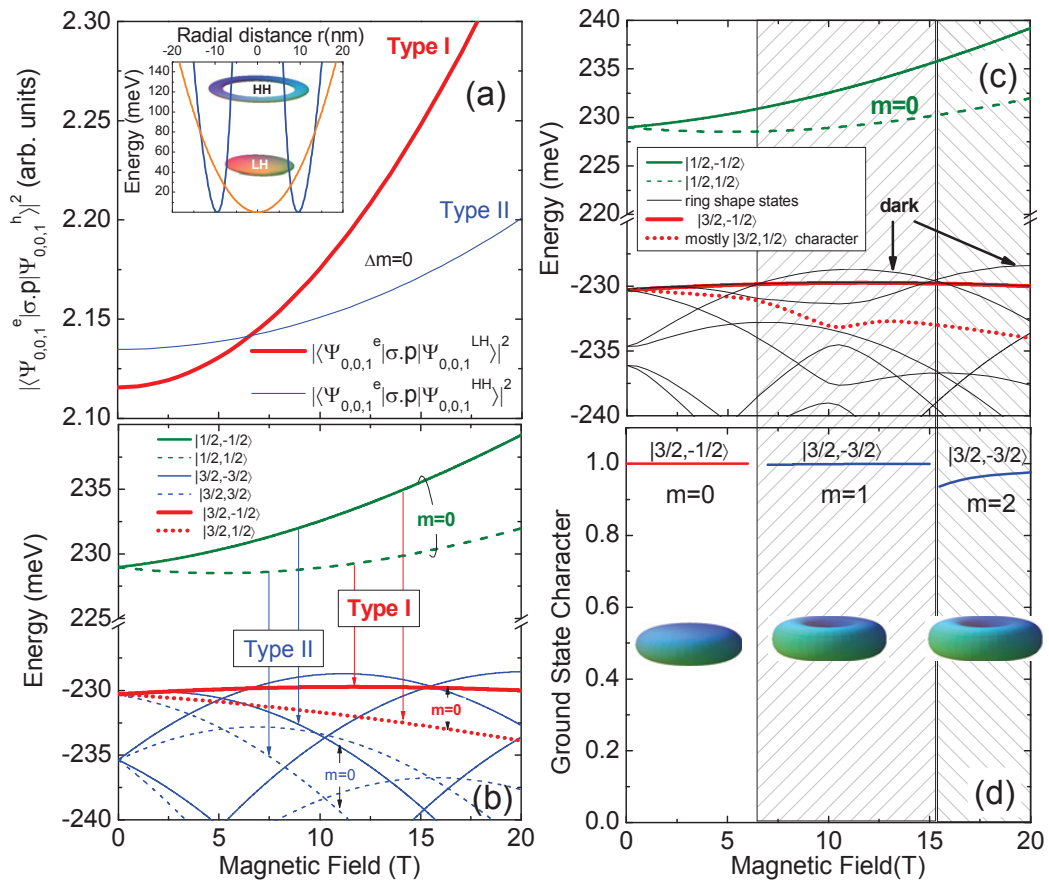
Figure 4.18: (a) The optical transition matrix elements involving the $m = 0$ HH and LH states of a QD with $R = 9.48$ nm and 6 nm height as a function of the magnetic field in the parabolic band approximation. The lateral QD profiles for the HH and LH subbands with a HH in the outer rim and a LH confined inside are shown in the inset. (b) The corresponding upper valence band and lower conduction band states (measured from above the energy gap) in a QD with HH in the outer rim and the electrons and LH confined inside as a function of the magnetic field in the parabolic band approximation. (c) The corresponding energy levels of a similar QD now with $e = 0.104$ calculated within the 4×4 Luttinger model. (d) The corresponding conduction band coefficients of the ground state and the electronic orbitals for each magnetic field region [7].

Before detailing the aspects of the peculiar valence band electronic structure, it is crucial to

discuss the relative probability for an electron-hole pair recombination involving either a HH state confined nearby the outer rim of the QD or a LH state in the internal part of the QR. The optical oscillator strength for the electron-hole pair recombination from the conduction band ground state with $\delta = 0$ and $l = 1$ is proportional to

$$|\langle \psi^e_{n,m,1} | \hat{\sigma}^{\pm} \hat{p} | \psi^h_{n,m,1} \rangle|^2 = |\langle \phi^e_{n,m} | \phi^h_{n,m} \rangle|^2 |\langle u_e | \hat{\sigma}^{\pm} \hat{p} | u_h \rangle|^2, \tag{4.4}$$

where $\hat{\sigma}^{\pm} = 1/\sqrt{2}(\hat{x} \pm i\hat{y})$ is the light angular polarization and the overlap integral can be calculated as

$$
\begin{aligned}
\langle \phi^e_{n,m} | \phi^h_{n,m} \rangle &= 2\pi \left(\frac{\Gamma[n + M_{(e)} + 1]}{2^{M_{(e)}+1} n! \Gamma[M_{(e)}+1]^2 \pi} \right)^{1/2} \frac{\lambda^{M_{(e)}+1}_{(h)}}{\lambda^{M_{(e)}+1}_{(e)}} \\
&\times \left(\frac{\Gamma[n + M_{(h)} + 1]}{2^{M_{(h)}+1} n! \Gamma[M_{(h)}+1]^2 \pi} \right)^{1/2} \int_0^\infty e^{-\frac{\rho'^2}{4}\left(\frac{\lambda^2_{(h)}}{\lambda^2_{(e)}} + 1 \right)} \rho'^{(M_{(h)}+M_{(e)}+1)} \\
&\times \ {}_1F_1\left(-n, M_{(e)}+1, \frac{1}{2}\left(\rho' \frac{\lambda_{(h)}}{\lambda_{(e)}} \right)^2 \right) {}_1F_1\left(-n, M_{(h)}+1, \frac{1}{2}\rho'^2 \right) d\rho'. \tag{4.5}
\end{aligned}
$$

The numerical integration along the radial coordinate in Eq. (4.5) was taken up to 30-40 nm (according to the electronic state) attaining a good convergence. By taking into account that $|\langle u_e | \hat{\sigma}^{\pm} \hat{p} | u_{LH} \rangle|^2 = 1/3|\langle u_e | \hat{\sigma}^{\pm} \hat{p} | u_{LH} \rangle|^2$, the matrix elements, $|\langle \psi^e_{0,0,1} | \hat{\sigma}^{\pm} \hat{p} | \psi^h_{0,0,1} \rangle|^2$, were calculated for the spatial potential profiles with $e = 0$ and no valence band mixing as displayed in Fig. 4.18(a). In these configurations, a crossing between electron-HH and electron-LH transition intensity would be expected at intermediary field $B \simeq 6$ T, in accordance to experimental results for the diamagnetic shift of the exciton ground state transition and the integrated PL intensities, shown respectively in Figs. 4.19(a) and 4.19(b). Yet, the type-II electron-HH optically allowed transition (from the $m = 0$ conduction band ground state to the $m = 0$ valence band levels) is not energetically favorable as depicted in Fig. 4.18(b). Thus, the main transition observed in the QD PL should be type-I since the energetically favorable states for type-II recombination correspond to $m = 1$ and $m = 2$ valence band states, forbidden for transitions from the $m = 0$ electron ground state. In the case of a type-I to type-II optical transition induced by magnetic field, it would also be expected to detect a shift in the energy position of the emission energy of the value of $g^* \mu_B B$ (with g^*-the electron effective Landé factor) due to the sudden change from LH to HH as the field increases. This is however not observed experimentally in Ref. [11],

where only a kink of the diamagnetic shift of the QD emission is perceptible.
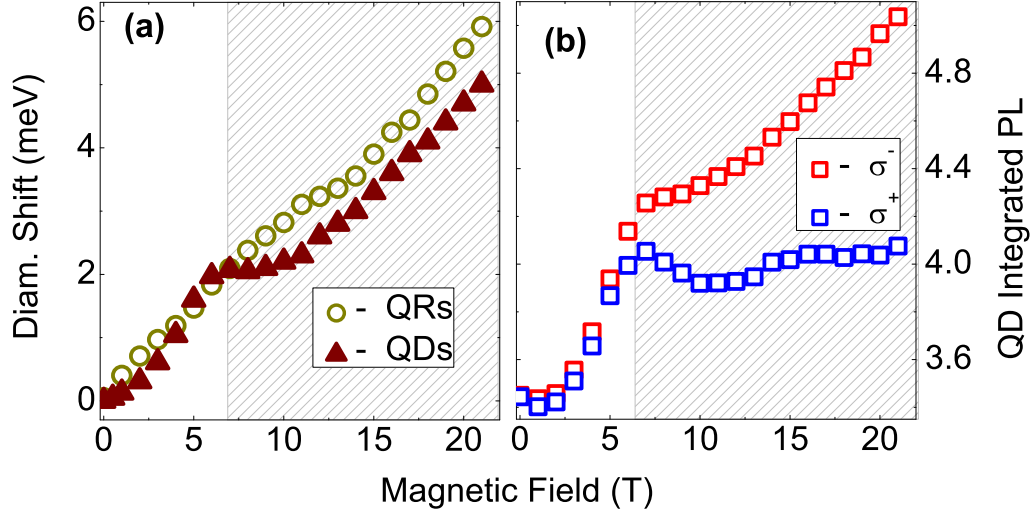
Figure 4.19: (a) Diamagnetic shift of the exciton ground state transitions versus magnetic field. (b) Integrated PL intensities for the hybrid sample, with σ^+ and σ^- polarizations measured in Faraday geometry for QDs as a function of magnetic field [11].

The character change between hole states, apparent energetically in the valence band ground state of the QD, is again illustrated in Fig. 4.18(c), where we tested the result beyond the parabolic band approximation within a Luttinger model as described in Ref. [7] to assess the relative effect of the proximity of both valence subbands and the potential selection rule relaxation do to level mixing. A small eccentricity, $e = 0.104$, has also been added within the range used for the QRs calculations. Despite the appearance of some anticrossings, there are no important contrasts between Figs. 4.18 (b) and 4.18(c). The reduced overlap of the HH and LH wavefunctions, displayed in Fig. 4.18(a) weakens the intersubband mixing. The character coefficients of the main basis components of the valence band ground state are also shown in Fig. 4.18(d) where it is proven that, beyond 6 T, dark excitons are formed and this has an impact in the optical transition rates as discussed in Ref. [3]. To complement this characterization, the wavefunction of the valence band ground state has been drawn for magnetic fields: 5 T, 10 T, and 20 T.

The variations of the PL intensity with the magnetic field in Ref. [11] can be ascribed to the energy crossing around 6T, where the character changes between LH and HH and, given the angular momentum modulation of the HH ground state, a bright-to-dark transition takes place according to the valence band occupancy [3]. It can also be noted that the strength of this effect is undoubtedly stronger for one of the spins. The effect of the bright-to-dark crossing contributes to a decrease of the PL after 6T where the LH and HH levels cross.

4.5 Conclusions

In summary, we have performed an electronic characterization of isolated QR samples. The results obtained are relevant for the optical properties, once the electron-hole pairs will be confined in the high In-content regions of the structure emulated in our calculations.

We have studied asymmetry effects in QRs motivated by experimental results of deformed QRs obtained during the growth process whose main consequence is the circularly symmetry breakdown. The asymmetric diffusion of atoms leads to some degree of anisotropy along the [110] and [1$\bar{1}$0] directions and subsequently to elongated QRs. The characterization of the local in-plane strain field shows that the most strained region of QDs is located at intermediary distances from the center, whereas for QRs the strain regions coincide with the highest In-concentration regions. The presence of strain fields affects the electronic structure and this may tune the state hybridization of the valence band ground state, as found in our multiband calculation. Non-zero values of the effective angular momentum may appear for certain combinations of strain fields and QR sizes. Thus, a fine control of the structural parameters and deformation during the QR synthesis and capping processes may become a powerful tool for the modulation of their optical properties and, certainly, their potential magnetic response.

We have also investigated hybrid structures where InGaAs/GaAs QRs are grown over a vertical superlattice of laterally aligned InGaAs/GaAs QDs. Rather different oscillations of PL intensity of circular polarized emissions detected experimentally [11] in the spectral range of the QD radiation for increasing magnetic field were interpreted in terms of joint effects associated to strain, spatial, and magnetic field confinement on the valence band forming the magneto-exciton ground state of the hybrid structure.

Two possible effects that could lead to different field dependence were studied: eccentricity of the confinement and strain induced different profiles for HH and LH carriers (the HH states will be predominantly confined nearby the lateral QD boundary while the LH states occupy the internal QD region). We demonstrated that the spin-dependent modulation of the intensity of the QD emission is weighted by the bright-to-dark crossing when the character of valence band ground state evolves from type-I LH to a type-II HH. We hope these findings may be further explored in many different samples.

Bibliography

[1] M. D. Teodoro, V. L. Campo Jr, V. Lopez-Richard, E. Marega Jr, G. E. MArques, Y. Galvão Gobato, F. Ilkawa, M. J. S. P. Brasil, Z. Y. AbuWaar, V. G. Dorogan, Yu. I. Mazur, M. Benamara, and G. J. Salamo, Phys. Rev. Lett. **104**, 086401 (2010).

[2] A. Bruno-Afonso and A. Latgé, Phys. Rev. B **71**, 125312 (2005); A. Bruno-Afonso and A. Latgé, Phys. Rev. B **61**, 15887 (2000); A. Bruno-Afonso and A. Latgé, Phys. Rev. B **77**, 205303 (2008).

[3] A. O. Govorov, S. E. Ulloa, K. Karrai, and R. J. Warburton, Phys. Rev. B **66**, 081309 (2002).

[4] A. Chaplik and Pis'ma Zh. Éksp, Teor. Fiz., **62**, 885 (1995)[JETP Lett. **62**, 900(1995)]

[5] R. A. Römer and M. E. Raikh, Phys. Rev. B **62**, 7045 (2000); R. A. Römer and M. E. Raikh, Phys. Stat. Sol. (b), **221**, 535 (2000).

[6] B. Li and F. M. Peeters, Phys. Rev. B **83**, 115448 (2011).

[7] M. D. Teodoro, A. Malachias, V. Lopes-Oliveira, D. F. Cesar, V. Lopez-Richard, G. E. Marques, E. Marega Jr., M. Benamara, Y. I. Mazur, and G. J. Salamo, J. Appl. Phys. **112**, 014319 (2012).

[8] C. Somaschini, S. Biette, A. Fedorov, N. Koguchi, and S. Sanguinetti, J. of Crystal Growth, **323**, 279 (2011).

[9] J. Wu, Z. M. Wang, K. Holmes, E. Marega Jr., Z. Zhou, H. Li, Y. I. Mazur, and G. J. Salamo, Appl. Phys. Lett. **100**, 203117 (2012).

[10] J. Wu, Z. M. Wang, K. Holmes, E. Marega Jr., Y. I. Mazur, and G. J. Salamo, J. Nanopart. Res. **14**, 919 (2012).

[11] V. Lopes-Oliveira, Y. I. Mazur, L. D. de Souza, L. A. B. Marçal, J. Wu, M. D. Teodoro, A. Malachias, V. G. Dorogan, M. Benamara, G. G. Tarasov, E. Marega Jr, G. E. Marques, Z. M. Wang, M. Orlita, G. J. Salamo, and V. Lopez-Richard, Phys. Rev. B **90**, 125315 (2014).

[12] T. Benabbas, Y. Androussi, and A. Lefebvre, J. Appl. Phys. **86**, 1945 (1999).

[13] J. Stangl, V. Holy, and G. Bauer, Rev. Mod. Phys. **76**, 725 (2004).

[14] C. Yi-Ping Chao and S. L. Chuang, Phys. Rev. B **46**, 4110 (1992).

[15] M. Tadic', F. M. Peeters, and K. L. Janssens, Phys. Rev. B **65**, 165333 (2002).

[16] K. L. Janssens, B. Partoens, and F. M. Peeters, Phys. Rev. B **67**, 235325 (2003).

[17] L. Villegas-Lelovsky, M. D. Teodoro, V. Lopez-Richard, C. Calseverino, A. Malachias, E. Marega Jr., B. L. Liang, Yu I. Mazur, G. E. Marques, C. Trallero-Giner, and G. J. Salamo, Nanoscale Res. Lett. **6**, 56 (2010).

[18] E. Margapoti, Fabrizio M. Alves, S. Mahapatra, T. Schmidt, V. Lopez-Richard, C. Destefani, E. Menendez-Proupin, Fanyao Qu, C. Bougerol, K. Brunner, A. Forchel, G. E. Marques, and L. Worschech, Phys. Rev. B **82**, 205318 (2010).

[19] E. Margapoti, Fabrizio M. Alves, S. Mahapatra, T. Schmidt, V. Lopez-Richard, C. Destefani, E. Menendez-Proupin, Fanyao Qu, C. Bougerol, K. Brunner, A. Forchel, G. E. Marques, and L. Worschech, New. J. Phys. **14**, 043048 (2012).

Chapter 5

BERRY PHASE IN RASHBA-QR UNDER TILTED MAGNETIC FIELD

In this chapter, we discuss the role of different orientations of an applied magnetic field as well as the interplay of a selected structural asymmetry, discussed in the previous chapter, and SO coupling on the characteristics of eigenstates in a QR system. We will use a nearly analytical model description of the QR, which allows for a thorough study of elliptical deformations and their influence on the spin character and Berry phase of different quantum states. To attain this goal, we organize the chapter as follows: Section 5.1 contains a brief introduction; Section 5.2 discusses tilted magnetic field effects in QR system; Section 5.3 introduces the SO effects; Section 5.4 presents a study of effects of magnetic field orientation, SO coupling and asymmetry together to generate Berry phases.

5.1 Introduction

The phase acquired when a system is subjected to a cyclic adiabatic process, as described by Berry and others [1–3], contains information on the geometrical properties of the parameter space over which the system is defined. In a spatially extended and multiply connected quantum system, this phase conveys nonlocal information on the system and possible net fluxes akin to the AB phase [4]. As such, it is attractive to develop experimental probes to measure this Berry phase, as well as theoretical models that connect its behavior to microscopic information or external fields. The geometric Berry phase has indeed played a fundamental role in understanding the behavior of a variety of systems and phenomena [2, 3, 5].

In mesoscopic systems, the Berry phase of electronic states has been explored by transport experiments, providing a unique window into microscopic fields and spin textures. They arise from the interplay of external fields, as well as intrinsic SO effects within the semiconductor nanostructures [6–10]. More recently, transport experiments have demonstrated that it is possible to control the geometric phase of electrons by the application of in-plane fields in InGaAs semiconductor mesoscopic ring [11].

Motivated by these experiments, we present here an analysis of the influence of magnetic field orientation and intensity on the Berry phase experienced by electrons in a realistic QR. As we will describe, the modulation of the geometric phase can arise from the symmetry reduction in the confinement potential or the competition between the external magnetic field and the intrinsic field arising from SO coupling effects. As such, this study addresses the link between spatial symmetry and spin properties, and the possible tuning of the geometrical phase by varying the intensity and/or orientation of an external magnetic field.

To this end, we use an effective mass description of the conduction band, and incorporate the effects of confinement asymmetry for electrons in a realistic QR, as well as the resulting Rashba SO coupling fields arising from confinement and external fields. By studying spin maps for angle and magnetic field intensities, we gain insights into the competition between different energy scales and how they impact the Berry phase associated with each electronic state. As level mixing is enhanced near resonant conditions, one anticipates interesting behavior at the anticrossing regions produced for example by varying magnetic field dependence in a given structure. There are pronounced spatial asymmetry effects in the angular momentum and spin character of different states, as one would expect. These asymmetries, introduced or enhanced by shape anisotropies and confinement potential in the QR, are found to play an important role in determining the Berry phase of the different states. We also find that effects of varying magnetic field tilt and intensity, as well as SO coupling, are reflected in the Berry phase and associated spin texture. The substantial phase modulation observed in the lower energy level manifold can be monitored and exploited in transport and optical experiments.

The main results of this work were published in Ref. [12].

5.2 Tilted Magnetic Field in QRs

The system under investigation in this chapter is the same used in the chapter 4, a QR with a general elliptical shape, defined by the lateral potential $V(\rho, \varphi)$ given in Eq. (4.3) and a QW in z direction $V(z)$ given by Eq. (2.69).

However, here, we will improve the DR3 model in order to turn it able to simulate different configurations of magnetic fields. In the chapter 4 we have already discussed about the effects of an applied magnetic field along the growth direction in a QR. Here we will analyze what happens with the conduction band when we change the field orientation varying the magnetic field angle θ from 0 to 90° continuously, as illustrated in Fig. 5.1. Thus, in the presence of a
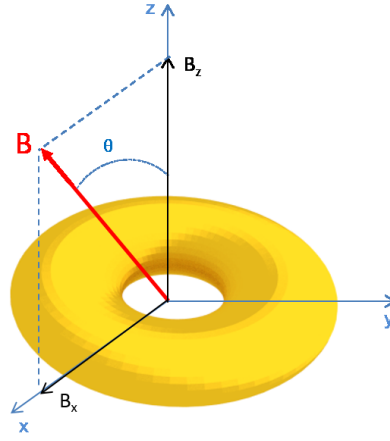
Figure 5.1: Scheme of tilted magnetic field applied in a QR.

magnetic field $\vec{B} = \hat{x}B_x + \hat{z}B_z = \hat{x}B\sin\theta + \hat{z}B\cos\theta$, the vector potential can be written as

$$\vec{A} = \frac{B_z}{2}\rho\hat{\varphi} - B_x z\left(\hat{\rho}\sin\varphi + \hat{\varphi}\cos\varphi\right) . \tag{5.1}$$

The system is described by Eq. (2.25). This equation can also be separated in another way, $H = H_{B_z} + H_{B_x} + H_{Z_x}$. The contribution due to the perpendicular component of the magnetic field (B_z) is given in cylindrical coordinates by

$$
\begin{aligned}
H_{B_z} &= -\frac{\hbar^2}{2\mu^*}\left[\frac{1}{\rho}\frac{\partial}{\partial\rho}\left(\rho\frac{\partial}{\partial\rho}\right) + \frac{1}{\rho^2}\frac{\partial^2}{\partial\varphi^2} + \frac{\partial^2}{\partial z^2}\right] \\
&+ \frac{ie\hbar B_z}{2\mu^*}\frac{\partial}{\partial\varphi} + \frac{e^2 B_z^2 \rho^2}{8\mu^*} + V(\vec{r}) \\
&+ \frac{g\mu_B}{2}B_z\sigma_z .
\end{aligned}
\tag{5.2}
$$

The eigenfunctions in the presence of the B_z component, $\Phi_{lmn}(z,\rho,\varphi)$, are used as the basis set to expand the eigenstates for a general tilted field. A general wavefunction can be written as

$$\Psi = \sum_{l,m,n} \left(C_{lmn}^{\uparrow} \ket{\uparrow} + C_{lmn}^{\downarrow} \ket{\downarrow} \right) \Phi_{lmn}, \tag{5.3}$$

where the spatial dependence has been omitted for simplicity. The term due to the in-plane component of the magnetic field is

$$\begin{aligned} H_{B_x} &= -\frac{ie\hbar z B_x}{\mu^*} \left(\sin\varphi \frac{\partial}{\partial\rho} + \frac{\cos\varphi}{\rho} \frac{\partial}{\partial\varphi} \right) \\ &+ \frac{e^2}{2\mu^*} \left(B_x^2 z^2 - B_z B_x z \rho \cos\varphi \right). \end{aligned} \tag{5.4}$$

and the respective Zeeman contribution can be written as [13]

$$H_{Z_x} = \frac{1}{4} g\mu_B B_x (\sigma^+ + \sigma^-), \tag{5.5}$$

where $\sigma^\pm = \sigma_x \pm i\sigma_y$. More details about this calculations can be found in Appendix B.

In Fig. 5.2, the energy levels are plotted for the conduction band where θ was set equal to $45°$. In this figure, each angular momentum is identified and the spin states up and down differentiated by blue and red colors, respectively. Comparing this graph to Fig. 4.1, we observe that increasing the angle, θ, makes the levels flatter, what can be observed for the ground state, for instance. While for the perpendicular magnetic field case ($\theta = 0$) crossings appear in the ground state around 2 and 6.3 T, when the field is tilted ($\theta = 45°$), these crossings change to 2.9 and 8.8 T, respectively.

Using Fig. 5.2 as reference, we plotted in Fig. 5.3 the energy over magnetic field angle θ for three values of magnetic field intensities, B. The values of B used, correspond to regions where the ground state changes character due to the crossings: $B = 2,9$ T, $B = 8,8$ T and $B = 14,7$ T. One may note that for high fields the character changes more often as θ increases and this happens every time a crossing appears in the energy figures. It is important to note that just changing the magnetic field angle is not enough to change the ground state character to different spin.
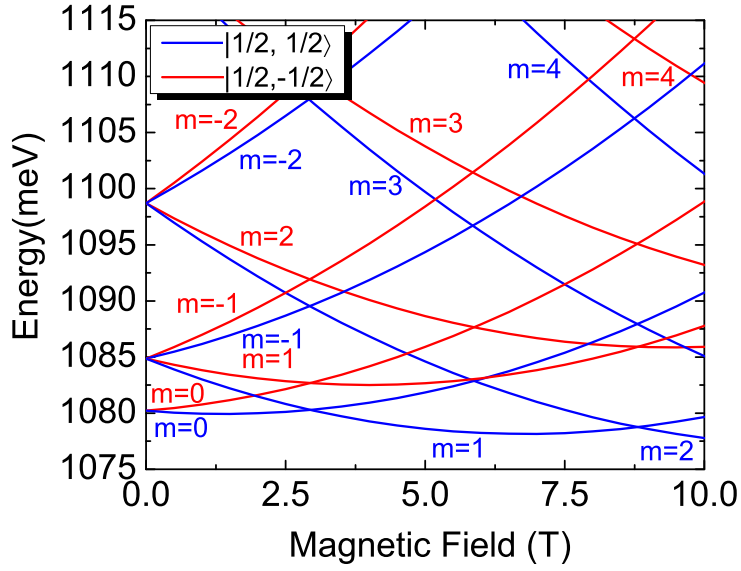
Figure 5.2: Conduction band over magnetic field: spin up (blue lines), spin down (red lines) with a tilted angle of 45°
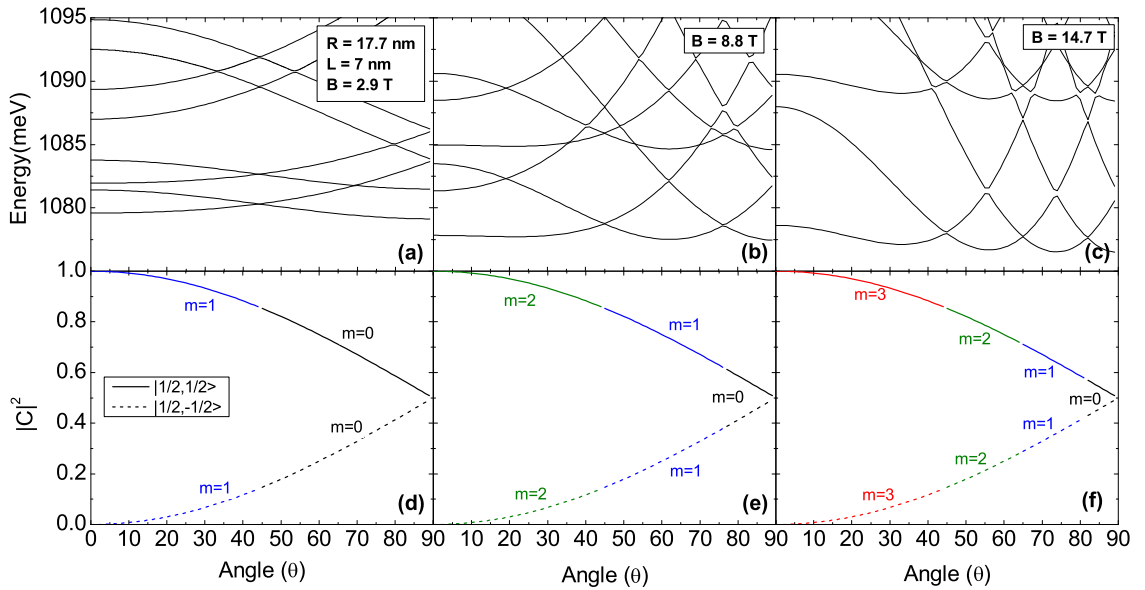
Figure 5.3: Conduction band energy versus magnetic field orientation θ for $R = 17.7$ nm, $L = 7$ nm at fixed magnetic field intensity (a) $B = 2.9$ T, (b) $B = 8.8$ T and (c) $B = 14.7$ T. Corresponding ground state expansion coefficients at (d) $B = 2.9$ T, (e) $B = 8.8$ T and (f) $B = 14.7$ T.

5.3   SO Coupling

In this section, we will discuss the effects of the SO coupling on the QR properties under tilted field. These effects, when included in the electronic structure calculations, lead to the interaction between different spin states. The SO coupling in the presence of SIA can be written

in terms of the field associated with the gradient of the confinement potential, ∇V, as [14]

$$H_{SIA} = \frac{\alpha_s}{\hbar} \vec{\sigma} \cdot \left(\nabla V \times (\vec{p} - e\vec{A}) \right),$$ (5.6)

where α_s characterizes the strength of the SO coupling in the host semiconductor. This can be decomposed, in cylindrical coordinates, into three terms, $H_{SIA} = H_{SIA}^D + H_R + H_K$, where [14]

$$
\begin{aligned}
H_{SIA}^D &= \alpha_s \sigma_z \left\{ \frac{\partial V}{\partial \rho} \left[-\frac{i}{\rho} \frac{\partial}{\partial \varphi} + \frac{eB_z}{2\hbar} \rho \right] + \frac{i}{\rho} \frac{\partial V}{\partial \varphi} \frac{\partial}{\partial \rho} \right. \\
&\left. + \frac{i}{\rho^2} \frac{\partial V}{\partial \varphi} \right\},
\end{aligned}
$$ (5.7)

$$
\begin{aligned}
H_R &= -\alpha_s \frac{\partial V}{\partial z} \left\{ \sigma^+ \left[e^{-i\varphi} \left(\frac{\partial}{\partial \rho} - \frac{i}{\rho} \frac{\partial}{\partial \varphi} + \frac{eB_z}{2\hbar} \rho + \frac{1}{\rho} \right) \right] \right. \\
&\left. - \sigma^- \left[e^{i\varphi} \left(\frac{\partial}{\partial \rho} + \frac{i}{\rho} \frac{\partial}{\partial \varphi} - \frac{eB_z}{2\hbar} \rho + \frac{1}{\rho} \right) \right] \right\},
\end{aligned}
$$ (5.8)

and $H_K = 0$ because $\langle k_z \rangle \simeq 0$. H_{SIA}^D is the spin-diagonal contribution due to the confinement, while the Rashba term H_R is associated with the perpendicular electric field in the well, $\partial V / \partial z = eF$. In Appendix A, the calculations to get the Eqs. (5.7) and (5.8), are detailed.

In Fig. 5.4, we show the changes in the ground state level and its character. For the electronic structure in Fig. 5.4(a), the anticrossings at the ground state, selected and amplified in the square boxes, mean that the levels are mixed due to the SO coupling. The mixtures are confirmed through the graph of the coefficients, also observed in Fig. 5.4(b). This effect can be contrasted with the energies plotted in Fig. 4.1 where the levels are pure.

We can also simultaneously simulate a tilted magnetic field and SO coupling. When the magnetic field is tilted, an additional term has to be included in the Hamiltonian, H_{SIA}, that gives the contribution for B_x component. This term is given by

$$H_{SIA}^{TF} = \alpha_s \frac{ezB_x}{\hbar} \left(\frac{\partial V}{\partial z} \sigma_x - \frac{\partial V}{\partial x} \sigma_z \right).$$ (5.9)

The complete calculation to get Eq. (5.9) is presented in the Appendix B.

Taking the two magnetic field values 2.9 and 14.7 T used in Fig. 5.3, we plotted again the electronic structures and coefficients for the same QR and magnetic field configuration, but with SO coupling. One may note, in Fig. 5.5, the presence of the anticrossings between the
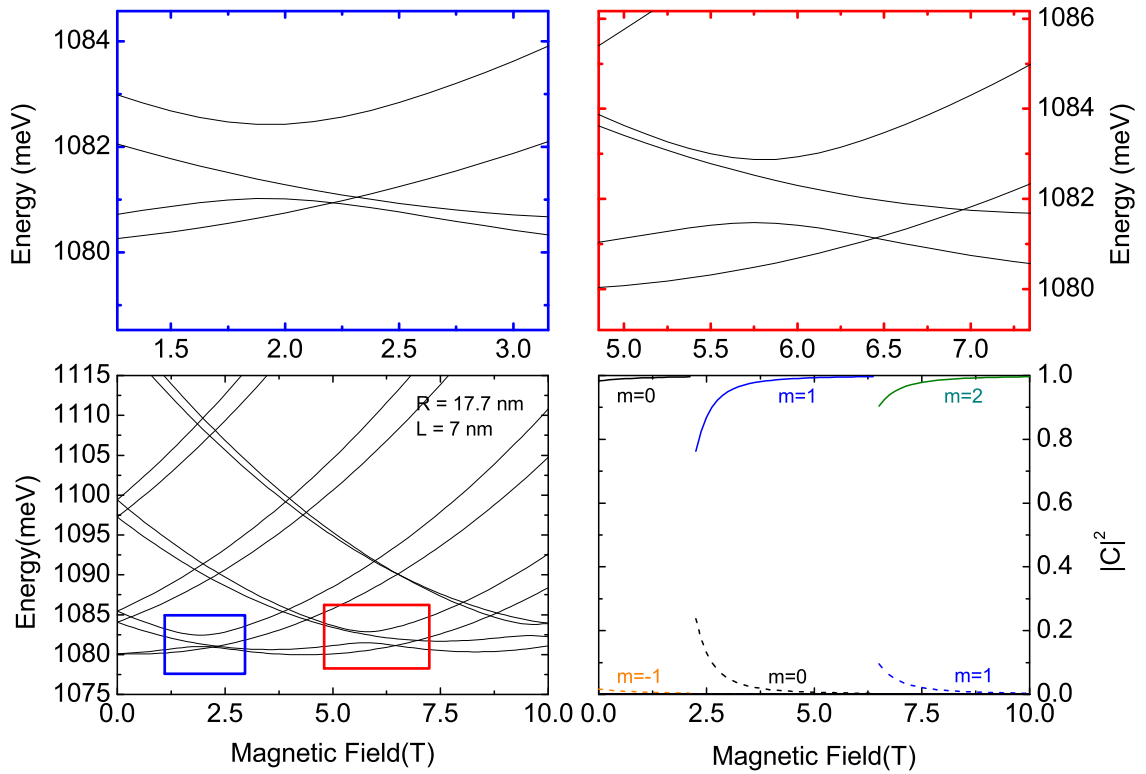
Figure 5.4: (a) Electronic structure and (b) ground state coefficients of a QR with perpendicular magnetic field ($\theta = 0°$) and SO coupling modulated by $F = 100 \; kV/cm^2$. The insets show zooms on the selected regions.

ground state and the other levels, not present before, and a high hybridization of the ground state, mainly for intermediate angle values, around $\theta = 42°$ in Fig. 5.5(d), for instance. This indicates a large role of the spin down character in the ground state.

Therefore, the model described up to here is able to simulate QR with asymmetric shapes, tilted magnetic fields and SO coupling simultaneously. In this way, we can turn on or disable one or more of these effects to understand the contribution of each phenomenon separately, as shown in Fig. 5.6, where we present different possibilities. In Fig. 5.6(a), we calculate the electronic structure for a circularly symmetric QR with a tilted magnetic field applied with an angle $\theta = 45°$, in Fig. 5.6(b) we activated the SO coupling by keeping the same configuration of Fig. 5.6(a). Yet, in Figs. 5.6(c) and 5.6(d), we recalculated the cases on Figs. 5.6(a) and 5.6(b) for an asymmetric (elongated) QR.
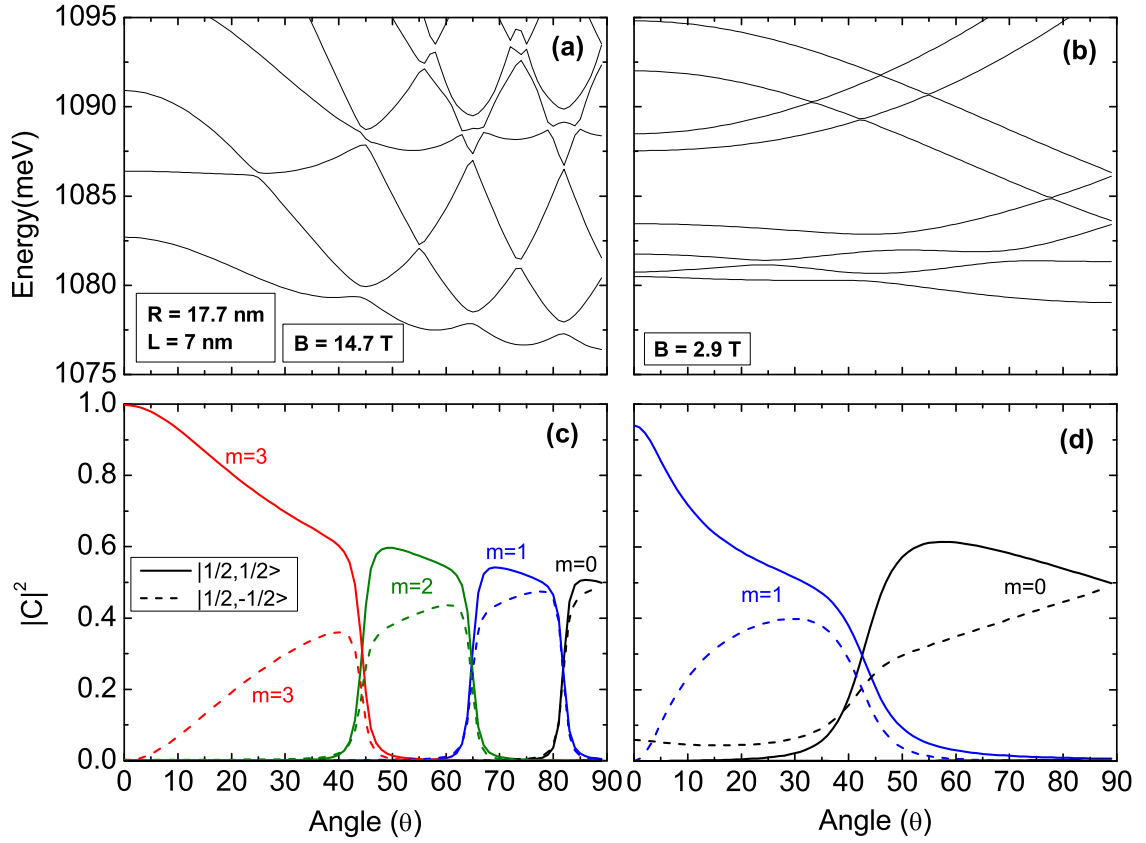
Figure 5.5: Conduction band energy versus magnetic field orientation θ for $R = 17.7$ nm, $L = 7$ nm with SO coupling modulated by $F = 100 \, kV/cm^2$ at fixed magnetic field intensity (a) $B = 14.7$ T, (b) $B = 2.9$ T. Corresponding ground state expansion coefficients at (c) $B = 14.7$ T, (d) $B = 2.9$ T.

5.4 Berry phase in asymmetric Rasha QR under tilted magnetic field

In this section, we will present the effects of tilted magnetic field, asymmetry, and SO coupling in the Berry phase. The Berry phase is an interesting quantity that characterizes the different eigenstates, especially as it incorporates the effects of external fields and SO coupling, and the influence of geometrical confinement. Different experiments would probe the Berry phases in different fashion, depending on the measurement design. Transport phase measurements, for example, would result in a mostly additive contribution of various channels involved in the conductance signal, i.e., those close to the Fermi energy. We illustrate the effect of cumulative phase by considering the total Berry phase for a collection of states, defined over a certain "occupation" in the QR (defined once such structure is connected to current reservoirs and a bias window is defined).
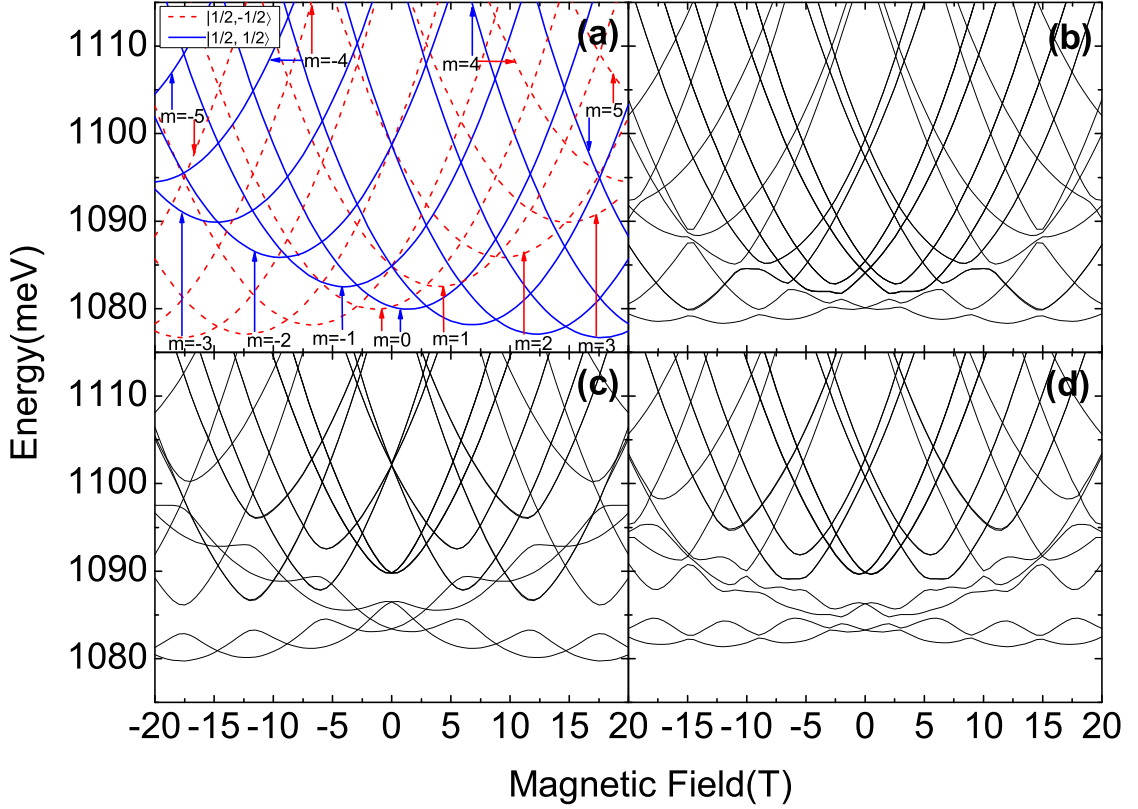
Figure 5.6: Electronic structure for a QR in the presence of a tilted magnetic field ($\theta = 45°$), with SO coupling and asymmetry strength modulated, respectively, by F and δ, where in (a) $\delta = 0$ and $F = 0$, (b) $\delta = 0$ and $F = 100\,kV/cm^2$, (c) $\delta = 2$ meV and $F = 0$ and (d) $\delta = 2$ meV and $F = 100\,kV/cm^2$.

In addition, we characterized the spin content of different eigenstates and analyzed the expectation value for the different components. In particular, we define the spin projection with respect to the z-axis, θ_s, in terms of projections along and perpendicular to the plane,

$$\langle \sigma^+ \rangle = \sum_j C_j^{\uparrow *} C_j^{\downarrow},$$
$$\langle \sigma_z \rangle = \sum_j \left(|C_j^{\uparrow}|^2 - |C_j^{\downarrow}|^2 \right) \tag{5.10}$$

(where $j = \{n, l, m\}$ in all sums), so that

$$\theta_s = \arctan \frac{\langle \sigma_z \rangle}{\langle \sigma^+ \rangle} + \frac{\pi}{2} \left(1 - \text{sgn} \langle \sigma^+ \rangle \right). \tag{5.11}$$

Figs. 5.7 and 5.8 show the electronic structure and the Berry phases for the lower energy manifold in both symmetric and asymmetric QRs. In Fig. 5.7, we plot the energy levels and the corresponding phases as function of the total magnetic field amplitude at a fixed angle, $\theta = 60°$,

while Fig. 5.8 shows the results for a fixed intensity of the magnetic field, $B = 6.625$ T, as a function of the orientation θ.
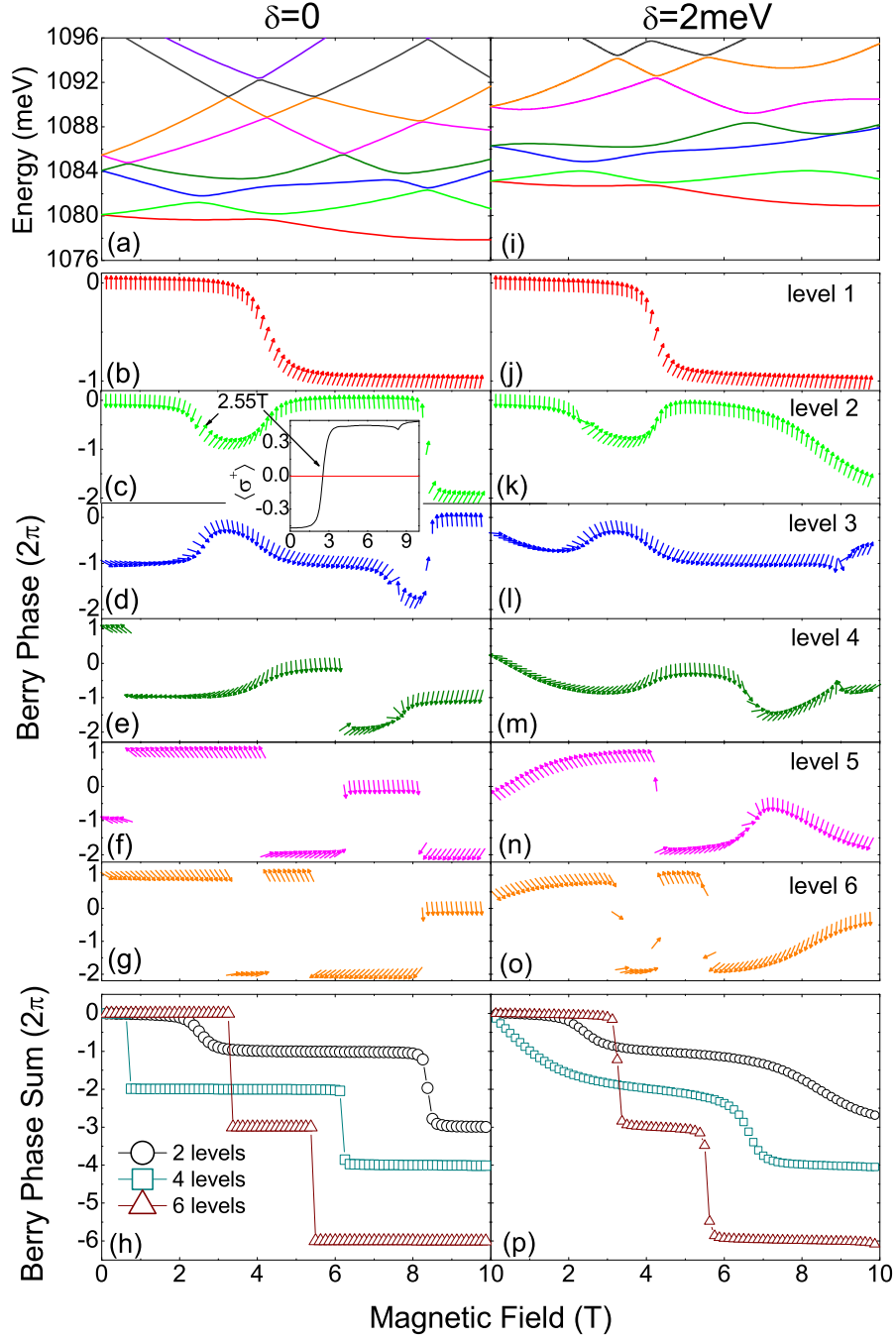
Figure 5.7: Electronic structure for QRs in a magnetic field at fixed tilt angle, $\theta = 60°$, and Rashba field $F = 100$ kV/cm, as a function of the total magnetic field strength for: (a) symmetric ($\delta = 0$) and (i) asymmetric ($\delta = 2$ meV) QR. The Berry phase for different levels for $\delta = 0$ is shown in panels on the left column, (b) through (g); and for $\delta = 2$ meV on the right column, (j) through (o). The cumulative Berry phase for different occupation numbers is shown in panel (h) for the symmetric QR, and panel (p) for the asymmetric QR [12].

The Berry phases of the lowest six levels, calculated using Eq. (2.77), are displayed in

the Figs. 5.7 and 5.8, along with the corresponding mean spin orientations. The arrows along the different Berry phase curves indicate the spin orientation, with θ_s as defined above: an upwards/downwards arrow in these curves, $\theta_s = \pm\pi/2$, indicates a spin lying on the *x-y* plane, while a horizontal arrow indicates a spin aligned along the $\pm z$-axis.
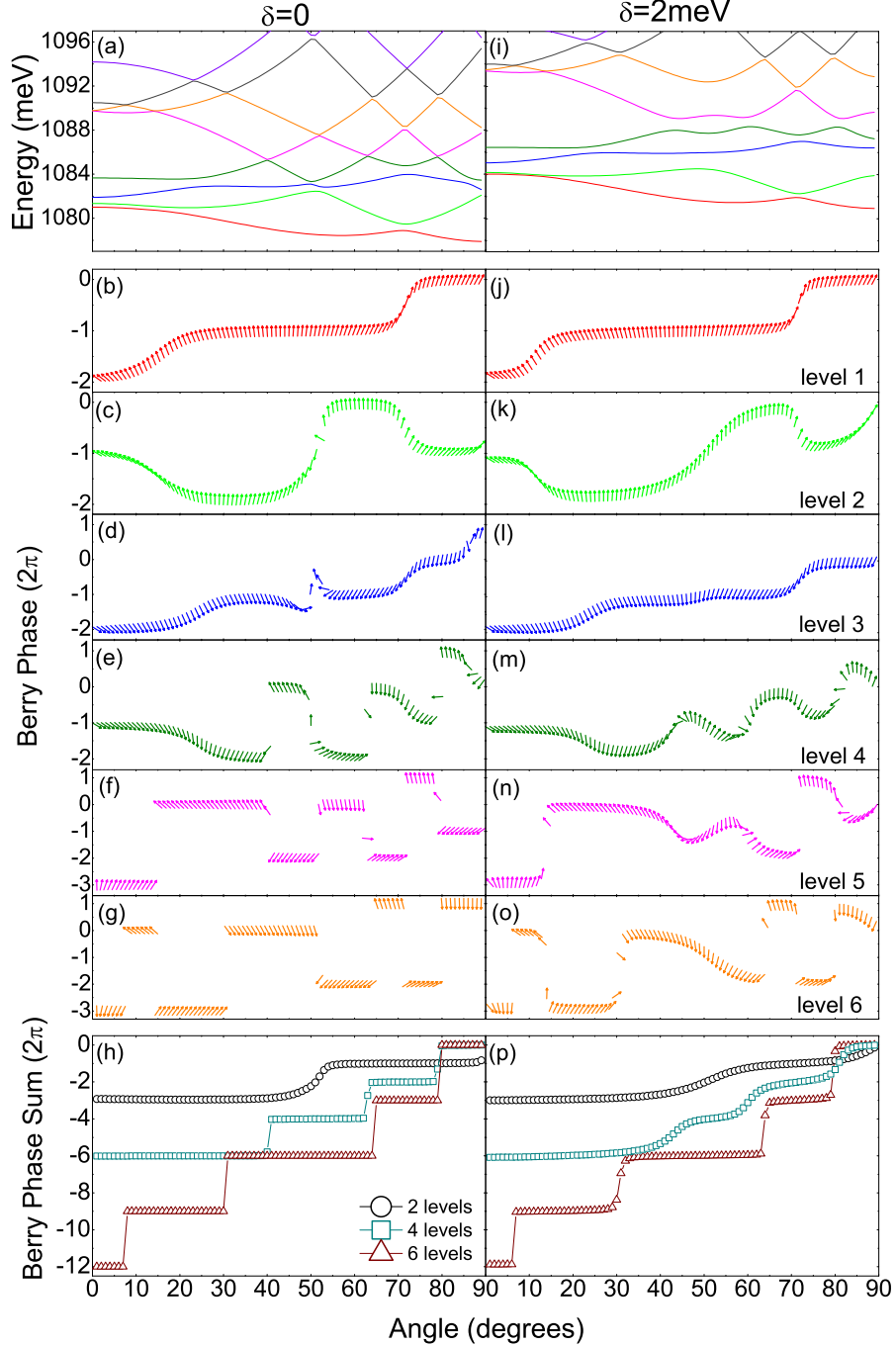
Figure 5.8: Electronic structure for QRs under fixed magnetic and Rashba fields, $B = 6.625$ T and $F = 100$ kV/cm, as a function of the magnetic field tilt angle θ for: (a) symmetric ($\delta = 0$) and (i) asymmetric ($\delta = 2$ meV) QR. Berry phases for different states in both QRs are shown in the panels below. The cumulative Berry phase for different occupations is shown in panels (h) and (p), for the symmetric and asymmetric QRs, respectively [12].

The results in the left panels of both figures are for a circularly symmetric QR. For small magnetic fields, the two lowest energy states exhibit spin mostly on the *x-y* plane, as shown in Figs. 5.7(b) and 5.7(c). On the other hand, the next four levels (Fig. 5.7(d)-(g)) are aligned along the $\pm z$-axis due to the spin mixing caused by SO coupling. Note that at high values of magnetic field the levels become essentially aligned with (Fig. 5.7(b)-(d)) or against (Fig. 5.7(e)-(g)) the magnetic field, as the Zeeman energy dominates over the SO coupling. The evolution of spin orientation for each level is strongly influenced by the anticrossings with other levels, as one would expect. Moreover, anticrossings also affect the Berry phase of states, causing a smooth variation with large amplitude ($\simeq 2\pi$) in many cases, such as in Fig. 5.7(b) and 5.7(c) at around 4 T; in Fig. 5.7(c) and 5.7(d) at around 2.5 T, 4 T and 8 T; and at around 7.8 T in 5.7(d) and 5.7(e).

Stronger spin-tilting and occasional total flips appear close to the region of nonzero (or $\neq 2\pi n$, with integer *n*) Berry phase, as shown in Fig. 5.7(c) at around 2.5 T, and in 5.7(d) and 5.7(e) at around 7.8 T. Thus, the spin hybridization and phase modulation are intrinsically linked due to SO coupling and magnetic field. Spin orientation and phase values smoothly change as a function of magnetic field intensity (or magnetic field orientation in Fig. 5.8). Some apparently sudden spin-flips also appear, as the one highlighted in panel 5.7(c), corresponding to a steep (yet continuous) variation of the spin component, as detailed in the inset. Similar smooth variations are presented for an eccentric (elliptically deformed) QR on the right panels, Fig. 5.7(j)-(o). The main effect introduced by the confinement asymmetry is to make the spin modulation and Berry phase vary more gradually with field intensity. This can be understood as arising from the asymmetry which introduces mixing of different angular momentum components and associated anticrossings. Notice in Fig. 5.7(i), that at higher magnetic fields, B>6 T, various levels mix. This can be seen in the large anticrossings between levels 2 and 3 at around 7 T, levels 4 and 5 at around 6.7 T, and levels 5 and 6 at around 8.5 T. The level mixture makes the spectrum flatter with field and, correspondingly, produces weaker variations in the Berry phase as well.

Fig. 5.7(h) displays the gradual cumulative process of adding Berry phases of the first 2, 4, and 6 consecutive levels of panels (b)-(g). A similar addition has been obtained for the asymmetric QR case, shown in Fig. 5.7(p). This additive process is equivalent to increasing electron number or number of levels around the Fermi level in a transport experiment. The cumulative Berry phase, especially for large number ($\gtrsim 3$) of levels counted, is essentially null

(or $= 2\pi n$). In fact, although individual levels show strong variation of the Berry phase with field, the cumulative phase does not: successive levels have compensating Berry phase changes, so that the cumulative effect is surprisingly near null (except for occasional 2π slips shown in the figure), especially for the 4 and 6-level traces shown.

The introduction of QR eccentricity changes the situation in a somewhat subtle fashion. Comparing left (h) and right (p) panels in Fig. 5.7, it is clear that as the eccentricity induces changes in the electronic spectrum and single-state Berry phases, the cumulative Berry phase shows gradual modulation, so that nontrivial values are seen over finite-size windows in field: 2 - 3 T and 7 - 9 T for cumulative Berry phase of 2 levels; 0 - 1 T and 6 - 7 T, for 4 levels; and 3 - 4 T and 5 - 6 T, for 6 levels. This would suggest that a moderate degree of asymmetry and/or disorder, unavoidably present in real systems, may in fact produce a more robust Berry phase signal in experiments.

Similar contrasts exist between circularly symmetric and asymmetric QRs as function of magnetic field orientation (at constant strength), as shown in Fig. 5.8. As in Fig. 5.7, each state shows a gradual Berry phase evolution with magnetic field angle near level anticrossings, and the diamagnetic shift provided by B_z decreases for larger angles. One can also see a rather interesting evolution of the spin orientation as the tilt angle increases. On the left panels, for the circularly symmetric QR, one also notices relatively sharp changes in Berry phase and spin orientation, as different angular momentum components are mixed by SO coupling. These jumps or drastic changes disappear or become smoother for the asymmetric QR (right panels), as the eccentricity mixes more strongly different angular momentum states. Panels (h) and (p) show the cumulative Berry phase for the two QRs. There is a similar behavior already seen in Fig. 5.7: a smooth variation with angle for small number of levels, changes to essentially null phase value ($2\pi n$) for larger level number. The sudden phase slips however become smoother, resulting in nontrivial values for the asymmetric QR over wider range (angular in this case).

We also explore the spatial variation in the spin orientation ('spin texture') for each state, which is related to the vector spin density, whose components are given by

$$
\begin{aligned}
S_x(\vec{r}) &= \sum_{j,j'} \Phi^*_{j'}(\vec{r}) \left(C^{\uparrow *}_{j'} C^{\downarrow}_j + C^{\downarrow *}_{j'} C^{\uparrow}_j \right) \Phi_j(\vec{r}) \\
S_y(\vec{r}) &= -i \sum_{j,j'} \Phi^*_{j'}(\vec{r}) \left(C^{\uparrow *}_{j'} C^{\downarrow}_j - C^{\downarrow *}_{j'} C^{\uparrow}_j \right) \Phi_j(\vec{r}) \\
S_z(\vec{r}) &= \sum_{j,j'} \Phi^*_{j'}(\vec{r}) \left(C^{\uparrow *}_{j'} C^{\uparrow}_j - C^{\downarrow *}_{j'} C^{\downarrow}_j \right) \Phi_j(\vec{r}) .
\end{aligned}
\tag{5.12}
$$

These components were used to depict the spin behavior around the QR what was done through the calculation of the wave function projection in each spin component. The graphs are performed by

$$x_2 = \frac{S_x}{max(|\vec{r}|)} + x_1 \tag{5.13}$$

$$y_2 = \frac{S_y}{max(|\vec{r}|)} + y_1 \tag{5.14}$$

$$z_2 = \frac{S_z}{max(|\vec{r}|)} + z_1 \tag{5.15}$$

and presented in Fig. 5.9.

The slow evolution of Berry phase for each state signals the mixtures introduced by the different perturbations on an otherwise highly-symmetric picture. The Zeeman field, SO coupling, and structural asymmetries produce simultaneous mixtures of spin, parity, and angular momentum. This effect, contained in the expansion coefficients of the different states, can be visualized as well through spin density maps. Fig. 5.9, left panels, show the expansion coefficients for the four lowest energy states of an asymmetric QR, as function of magnetic field, at a fixed angle $\theta = 60°$. These panels show solid (dashed) curves for the spin up (down) components with different angular momentum m in the given state. The states are mixtures of angular momentum (introduced at zero field by the QR asymmetry) and/or spin (due to SO coupling), which evolve with field to other components (due to the diamagnetic shift of the spectrum), and eventually to more complex mixtures at higher energies.

The right panels in Fig. 5.9 show spin vector maps for the corresponding state at the field $B = 2.375$T, and $\theta = 60°$. This field value corresponds to the anticrossing between the second and third levels in Fig. 5.7(i). The vector maps use arrows with size proportional to the spin density at each point on the plane and blue (or red) colors to indicate a positive (or negative) sign of the z-spin component at that point. The ground state (level 1) shows a spin map predominantly on the plane, although with overall positive S_z component, and with high amplitude near the ends of the long-axis ellipse. The first-excited state, in contrast, shows large negative S_z components and with a spatial distribution that complements that of the ground state. One also notices that the ground state spin map shows local vectors that are essentially parallel all along the QR: this would result in a vanishing Berry phase, as it is indeed seen in Fig. 5.7(j), at this magnetic field. For the second level, however, where the Berry phase $\simeq -\pi$ in Fig. 5.7(k), one notices that the spin arrows in Fig. 5.9 are canted with respect to those a quarter of the way
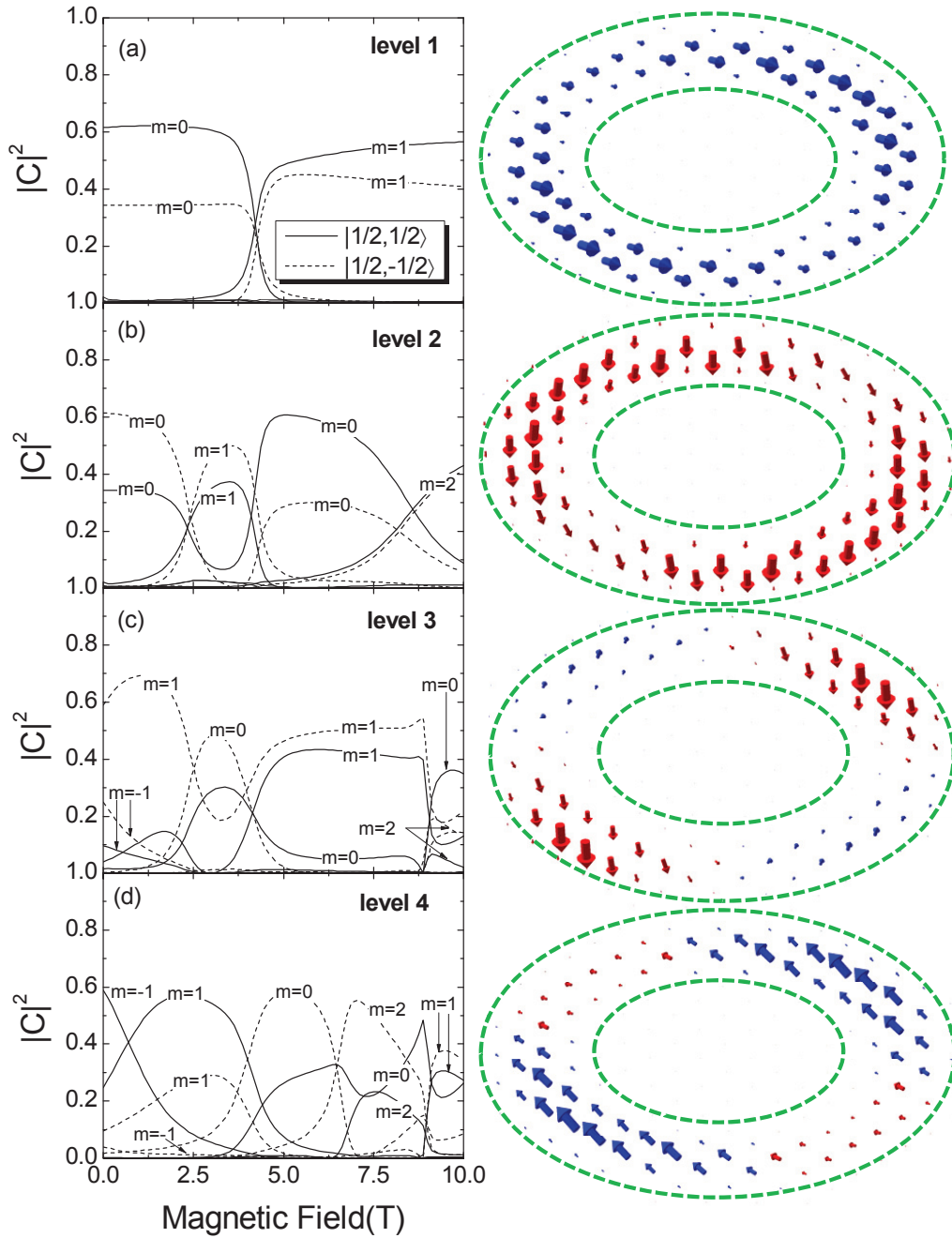
Figure 5.9: Panels on the left column shown expansion coefficients for the four lowest states of an asymmetric QR ($\delta = 2$ meV), and fixed Rashba field $F = 100$ kV/cm, and magnetic field tilt angle $\theta = 60°$, as function of magnetic field intensity. Level admixtures clearly evolve with sudden switches at level anticrossings. The right column shows spin density vector maps along the QR (z-integrated) for the four lowest states at a field $B = 2.375$ T. Blue arrows have a positive projection along z, while for red arrows the projection is negative. Notice nearly parallel vectors in level 1 result in a null Berry phase; in contrast, canting of vectors in level 2 contribute to a Berry phase of $\simeq -\pi$ (see Fig. 5.7(k)) [12].

along the QR. It is this non-parallel nature of the spins along the QR structure that characterizes

a non-vanishing Berry phase. Levels 3 and 4 show even more structure, with spin vector ampli-

tude more localized near the long ends of the ellipse, but with S_z component that changes sign as one moves along the QR. The relative twisting of the spin vector density along the QR, contributes to the non-vanishing Berry phase seen in Fig. 5.7(l)-(m), although with much smaller value than for level 2. Other levels with non-vanishing Berry phase show similar canted spin texture across the QR.

5.5   Conclusions

We have used a nearly analytical description of the states in QRs of finite width. This model, used before to describe realistic structures in experiments, allows us to extract interesting insights on the role of SO coupling and its interplay with external magnetic field effects, such as diamagnetic shifts and Zeeman splitting. We have moreover introduced asymmetry in the confinement structure to see how this affects the level structure and associated spin texture and Berry phase of different states. We observed that possible experimental sweeps of magnetic field tilt or amplitude, produce controllable changes in the state characteristics, which can be traced in particular through the smooth variation of the Berry phase of each state. It is also clear that as SO coupling could be made stronger with applied electric fields, the Rashba effect would also controllably change the overall geometric phase in QRs.

Somewhat surprisingly, we found that the unavoidable defects or asymmetries in QR confinement produce smooth changes in the Berry phase, as either the magnetic field or tilt (or even Rashba field) is changed. This effect makes the otherwise sudden phase slips in symmetric QRs become smoother and produce non-vanishing (or nontrivial) geometric phases as a consequence. This would suggest that moderate level mixing makes for more robust Berry phases in experiments. One should also comment, that although the multilevel cumulative Berry phase appears essentially null for high number of levels (or wider energy window), it may be possible to access individual (or few) state Berry phases in narrow bias ranges or similarly to other experiments where few states can be sampled.

Bibliography

[1] M. V. Berry, Proc. R. Soc. Lond. A **392**, 45 (1984).

[2] A. Shapere and F. Wilczek, Geometric Phases in Physics. Singapore: World Scientific, 1989.

[3] D. Xiao, M.-C. Chang, and Q. Niu, Rev. Mod. Phys. **82**, 1959 (2010).

[4] Y. Aharonov and D. Bohm, Phys. Rev. **115**, 485 (1959).

[5] S. Filipp, J. Klepp, Y. Hasegawa, C. Plonka-Spehr, U. Schmidt, P. Geltenbort, and H. Rauch, Phys. Rev. Lett. **102**, 030404 (2009).

[6] A. G. Aronov and Y. B. Lyanda-Geller, Phys. Rev. Lett. **70**, 343 (1993).

[7] A. F. Morpurgo, J. P. Heida, T. M. Klapwijk, B. J. van Wees, and G. Borghs, Phys. Rev. Lett. **80**, 1050 (1998).

[8] J.B. Yau, E.P. De Poortere, and M. Shayegan, Phys. Rev. Lett. **88**, 146801 (2002).

[9] T. Bergsten, T. Kobayashi, Y. Sekine, and J. Nitta, Phys. Rev. Lett. **97**, 196803 (2006).

[10] B. Grbić, R. Leturcq, T. Ihn, K. Ensslin, D. Reuter, and A. D. Wieck, Phys. Rev. Lett. **99**, 176803 (2007).

[11] F. Nagasawa, D. Frustaglia, H. Saarikoski, K. Richter, and J. Nitta, Nat. Commun. **4**, 2526 (2013).

[12] V. Lopes-Oliveira, L. K. Castelano, G. E. Marques, S. E. Ulloa, and V. Lopez-Richard, Phys. Rev. B **92**, 035441 (2015).

[13] G. Lommer, F. Malcher, and U. Rössler, Phys. Rev. Lett. **60**, 728 (1988).

[14] C. F. Destefani, S. E. Ulloa, and G. E. Marques, Phys. Rev. B **69**, 125302 (2004).

Chapter 6

GENERAL CONCLUSIONS

In this thesis, we studied a series of properties related to semiconductor nanostructures based in InAs and GaAs, InGaAs, and InGaAsN. We followed a sequence of tasks to develope the building blocks for the simulation of the electronic properties of a variety of quantum systems ending at the QRs. Beside purely theoretical interests, part of the tasks were carried out in partnership with experimental groups, simulating and interpreting their results. But, always keeping the focus on our main objective: study the effects related to QRs systems. Thus, in the last years, we have developed a model for QRs able to simulate realistic both QR or QD. This model allowed to characterize several properties and define the dominant effects.

To attain our goals, we started by studying the basic effects of quantum confinement, composition and strain in semiconductor nanostructures by building the effective band Hamiltonians. We firstly simulated an anomalous behavior of the PL peak energy at low temperature observed experimentally for samples of InGaAs and InGaAsN QW systems with QD shape defects. We ascribed some anomalous effects detected experimentally as due to strain modulation and localization. The results were compared for different QWs sizes. In this analysis, we observed that spin-dependent effects are stronger for wider QWs for both systems, N-free and N-containing samples. In addition, we showed that the spin polarization degree is dependent on the character of valence band ground state as expected for QD kind of confinement.

Moving towards the QRs, we improved our QD models and determined the profile of the effective confinement potential through the modulation of the QR composition. Then, the appearance of strain fields in QRs was associated to the reduction of their dimensions when the samples are capped. It affects the valence band ground state and we were able o understand this process.

Next, we studied the effects of external fields and asymmetries in QRs. Three different deformations effects were analyzed in the conduction and valence band, leading to some degree of anisotropy along the $[110]$ and $[1\bar{1}0]$ directions. This analysis was useful to assess how powerful our tool was for the simulations of the optical properties.

After the study of general effects of deformation, we used one of the three types of asymmetries in the analysis of elongated QD-QR stacked systems. This type of deformation was chosen because represents well the structures obtained by our experimental collaborators being the most probable form assumed by the QRs during their growth.

Using the elongated QR model, we contrasted our calculation with the PL results and interpreted them in terms of joint effects associated to strain, spatial, and magnetic field confinement on the valence band forming the magneto-exciton ground state of the hybrid structure. We also demonstrated that the spin-dependent modulation of the intensity of the QD emission is weighted by the bright-to-dark crossing when the character of valence band ground state evolves from type-I LH to a type-II HH.

Finally, the most realistic QR model was achieved and used to study the effect of a controllable applied magnetic field, asymmetry/deformation and SO in a conduction band QR. We were able to determine their relative weight to modulate the Berry phase of different states. We observed that the asymmetries in QRs change considerably the Berry phase as well as magnetic fields. Besides, we mapped the spin texture and observed the effects of the asymmetry.

To finish, We can conclude that the model developed in this thesis allows the direct simulation of a QR or a QD system. Further, this model is easily extensible for vertical coupled QRs and core-shell structure, that are the proposals for continuation of this research.

Appendix A

SO FIELD AND SELECTION RULES

In this Appendix, we detail the SIA Hamiltonian and the selection rules calculations.

A.1 SIA Hamiltonian

The SIA term for the QR confinement, $V(\mathbf{r}) = V(\rho, \varphi) + V(z)$, and coupling parameter α_s is given by

$$H_{SIA} = \alpha_s \boldsymbol{\sigma} \cdot (\nabla V \times k) \tag{A.1}$$

which we detail below in Cartesian coordinates.

$$H_{SIA} = \alpha_s \boldsymbol{\sigma} \cdot \left[\left(\frac{\partial V}{\partial x}\hat{i} + \frac{\partial V}{\partial y}\hat{j} + \frac{\partial V}{\partial z}\hat{k} \right) \times \left(k_x\hat{i} + k_y\hat{j} + k_z\hat{k} \right) \right] \tag{A.2}$$

$$H_{SIA} = \alpha_s \boldsymbol{\sigma} \cdot \left[\left(\frac{\partial V}{\partial y}k_z - \frac{\partial V}{\partial z}k_y \right)\hat{i} + \left(\frac{\partial V}{\partial z}k_x - \frac{\partial V}{\partial x}k_z \right)\hat{j} + \left(\frac{\partial V}{\partial x}k_y - \frac{\partial V}{\partial y}k_x \right)\hat{k} \right] \tag{A.3}$$

$$H_{SIA} = \alpha_s \left[\sigma_x \left(\frac{\partial V}{\partial y}k_z - \frac{\partial V}{\partial z}k_y \right) + \sigma_y \left(\frac{\partial V}{\partial z}k_x - \frac{\partial V}{\partial x}k_z \right) + \sigma_z \left(\frac{\partial V}{\partial x}k_y - \frac{\partial V}{\partial y}k_x \right) \right] \tag{A.4}$$

$$H_{SIA} = \alpha_s \left[\left(\sigma_x \frac{\partial V}{\partial y} - \sigma_y \frac{\partial V}{\partial x} \right) k_z + \frac{\partial V}{\partial z} \left(\sigma_y k_x - \sigma_x k_y \right) + \sigma_z \left(\frac{\partial V}{\partial x}k_y - \frac{\partial V}{\partial y}k_x \right) \right] \tag{A.5}$$

The contribution of the first terms in the right hand side of Eq. (A.5) to the lower sub-band vanishes because $\langle k_z \rangle = 0$. According to the symmetry of the problems tackled, we may transform Eq. (A.5) in cylindrical coordinates using the following relations

$$\sigma_\pm = \frac{1}{2}(\sigma_x \pm i\sigma_y), \tag{A.6}$$

$$k_\pm = k_x \pm ik_y \tag{A.7}$$

and the following relation

$$\left(\frac{\partial}{\partial x} \mp i\frac{\partial}{\partial y} \right) = L_\mp \left(\frac{\partial}{\partial \rho} \mp \frac{i}{\rho}\frac{\partial}{\partial \varphi} \right), \tag{A.8}$$

$$\frac{\partial}{\partial x} = \cos\varphi\frac{\partial}{\partial \rho} - \frac{1}{\rho}\sin\varphi\frac{\partial}{\partial \varphi}, \tag{A.9}$$

and

$$\frac{\partial}{\partial y} = \sin\varphi\frac{\partial}{\partial \rho} + \frac{1}{\rho}\cos\varphi\frac{\partial}{\partial \varphi}, \tag{A.10}$$

to transform $\frac{\partial}{\partial x}$ and $\frac{\partial}{\partial y}$ to $\frac{\partial}{\partial \rho}$ and $\frac{\partial}{\partial \varphi}$, where $L_\pm = e^{\pm i\varphi}$.

Firstly, we substitute the Eq. (A.6) in Eq. (A.5), and obtain

$$H_{SIA} = \alpha_s \left\{ \frac{\partial V}{\partial z}[-i(\sigma_+ - \sigma_-)k_x - (\sigma_+ + \sigma_-)k_y] + \sigma_z \left(\frac{\partial V}{\partial x}k_y - \frac{\partial V}{\partial y}k_x \right) \right\}, \tag{A.11}$$

rewritten as

$$H_{SIA} = \alpha_s \left\{ -\frac{\partial V}{\partial z}[i\sigma_+(k_x - ik_y) - i\sigma_-(k_x + ik_y)] + \sigma_z \left(\frac{\partial V}{\partial x}k_y - \frac{\partial V}{\partial y}k_x \right) \right\} \tag{A.12}$$

to make easier to replace the Eq. (A.7), that in Eq. (A.12) results in

$$H_{SIA} = \alpha_s \left\{ -i\frac{\partial V}{\partial z}(\sigma_+ k_- - \sigma_- k_+) + \sigma_z \left[\frac{\partial V}{\partial x}\left(\frac{k_+ - k_-}{2i} \right) - \frac{\partial V}{\partial y}\left(\frac{k_+ + k_-}{2} \right) \right] \right\} \tag{A.13}$$

or better in

$$H_{SIA} = \alpha_s \left\{ -i\frac{\partial V}{\partial z}(\sigma_+ k_- - \sigma_- k_+) - \frac{i}{2}\sigma_z \left[\left(\frac{\partial V}{\partial x} - i\frac{\partial V}{\partial y} \right)k_+ - \left(\frac{\partial V}{\partial x} + i\frac{\partial V}{\partial y} \right)k_- \right] \right\}. \tag{A.14}$$

Thus, we may substitute Eq. (A.8) into Eq. (A.14) and yielding

$$
\begin{aligned}
H_{SIA} &= \alpha_s \left\{ -i\frac{\partial V}{\partial z}\left(\sigma_+ k_- - \sigma_- k_+\right) - \frac{i}{2}\sigma_z \left[L_- \left(\frac{\partial V}{\partial \rho} - \frac{i}{\rho}\frac{\partial V}{\partial \varphi} \right) k_+ \right.\right. \\
&\quad - \left.\left. L_+ \left(\frac{\partial V}{\partial \rho} + \frac{i}{\rho}\frac{\partial V}{\partial \varphi} \right) k_- \right] \right\}.
\end{aligned}
\tag{A.15}
$$

The Hamiltonian in Eq. (A.15) can be separated into two contributions: H_{SIA}^D and H_R, where H_{SIA}^D is the contribution due to the radial confinement, and H_R is the Rashba term of associated with the perpendicular confinement effective field, dV/dz. Therefore,

$$
H_R = -i\alpha_s \frac{\partial V}{\partial z}\left(\sigma_+ k_- - \sigma_- k_+\right)
\tag{A.16}
$$

and

$$
H_{SIA}^D = -i\frac{\alpha_s}{2}\sigma_z \left[\frac{\partial V}{\partial \rho}\left(L_- k_+ - L_+ k_-\right) - \frac{i}{\rho}\frac{\partial V}{\partial \varphi}\left(L_- k_+ + L_+ k_-\right) \right].
\tag{A.17}
$$

Using the Eq. (A.18)

$$
k_\pm = \pm iL_\pm A_\pm = -ie^{\pm i\varphi}\left[\frac{\partial}{\partial \rho} \pm \frac{i}{\rho}\frac{\partial}{\partial \varphi} \mp \alpha\rho \right]
\tag{A.18}
$$

with $\alpha = \frac{eB_z}{2c\hbar}$ and

$$
A_\pm = \mp\frac{\partial}{\partial \rho} - \frac{i}{\rho}\frac{\partial}{\partial \varphi} + \alpha\rho,
\tag{A.19}
$$

in Eq. (A.17) we have

$$
\begin{aligned}
H_{SIA}^D &= -i\frac{\alpha_s}{2}\sigma_z \left\{ \frac{\partial V}{\partial \rho}\left[L_-(iL_+ A_+) + L_+(iL_- A_-) \right] \right. \\
&\quad - \left. \frac{i}{\rho}\frac{\partial V}{\partial \varphi}\left[L_-(iL_+ A_+) - L_+(iL_- A_-) \right] \right\}
\end{aligned}
\tag{A.20}
$$

that can be simplified to

$$
H_{SIA}^D = \frac{\alpha_s}{2}\sigma_z \left\{ \frac{\partial V}{\partial \rho}[A_+ + A_-]\frac{i}{\rho}\frac{\partial V}{\partial \varphi}[A_+ - A_-] \right\}.
\tag{A.21}
$$

However, $A_\pm$ are not hermitian. To make this Hamiltonian hermitian, we will replace $A_\pm$ by

$\hat{A}_\pm$, where $\hat{A}_\pm = A_\pm \mp \frac{1}{\rho}$ and proceed with following the steps

$$H_{SIA}^D = \frac{\alpha_s}{2}\sigma_z \left\{ \frac{\partial V}{\partial \rho} [\hat{A}_+ + \hat{A}_-] - \frac{i}{\rho}\frac{\partial V}{\partial \varphi} [\hat{A}_+ - \hat{A}_-] \right\} \tag{A.22}$$

$$H_{SIA}^D = \frac{\alpha_s}{2}\sigma_z \left\{ \frac{\partial V}{\partial \rho} \left[A_+ - \frac{1}{\rho} + A_- + \frac{1}{\rho} \right] - \frac{i}{\rho}\frac{\partial V}{\partial \varphi} \left[A_+ - \frac{1}{\rho} - A_- - \frac{1}{\rho} \right] \right\} \tag{A.23}$$

$$H_{SIA}^D = \frac{\alpha_s}{2}\sigma_z \left\{ \frac{\partial V}{\partial \rho} [A_+ + A_-] - \frac{i}{\rho}\frac{\partial V}{\partial \varphi} [A_+ - A_-] + \frac{2i}{\rho^2}\frac{\partial V}{\partial \varphi} \right\} \tag{A.24}$$

$$
\begin{aligned}
H_{SIA}^D = \ & \frac{\alpha_s}{2}\sigma_z \left\{ \frac{\partial V}{\partial \rho} \left[-\frac{\partial}{\partial \rho} - \frac{i}{\rho}\frac{\partial}{\partial \varphi} + \frac{eB_z}{2c\hbar}\rho + \frac{\partial}{\partial \rho} - \frac{i}{\rho}\frac{\partial}{\partial \varphi} + \frac{eB_z}{2c\hbar}\rho \right] \right. \\
& \left. - \frac{i}{\rho}\frac{\partial V}{\partial \varphi} \left[-\frac{\partial}{\partial \rho} - \frac{i}{\rho}\frac{\partial}{\partial \varphi} + \frac{eB_z}{2c\hbar}\rho - \frac{\partial}{\partial \rho} + \frac{i}{\rho}\frac{\partial}{\partial \varphi} - \frac{eB_z}{2c\hbar}\rho \right] + \frac{2i}{\rho^2}\frac{\partial V}{\partial \varphi} \right\} \tag{A.25}
\end{aligned}
$$

$$H_{SIA}^D = \frac{\alpha_s}{2}\sigma_z \left\{ \frac{\partial V}{\partial \rho} \left[-2\frac{i}{\rho}\frac{\partial}{\partial \varphi} + 2\frac{eB_z}{2c\hbar}\rho \right] - \frac{i}{\rho}\frac{\partial V}{\partial \varphi} \left[-2\frac{\partial}{\partial \rho} \right] + \frac{2i}{\rho^2}\frac{\partial V}{\partial \varphi} \right\} \tag{A.26}$$

until get

$$H_{SIA}^D = \alpha_s\sigma_z \left\{ \frac{\partial V}{\partial \rho} \left[-\frac{i}{\rho}\frac{\partial}{\partial \varphi} + \frac{eB_z}{2c\hbar}\rho \right] + \frac{i}{\rho}\frac{\partial V}{\partial \varphi}\frac{\partial}{\partial \rho} + \frac{i}{\rho^2}\frac{\partial V}{\partial \varphi} \right\}. \tag{A.27}$$

Proceeding analogously for Eq. (A.16), replacing Eq. (A.18) in (A.16), we obtain an hermitian Hamiltonian for H_R, as follows

$$H_R = -i\alpha_s\frac{\partial V}{\partial z} \left(\sigma_+(-iL_-\hat{A}_-) - \sigma_-(iL_+\hat{A}_+) \right) \tag{A.28}$$

$$H_R = -\alpha_s\frac{\partial V}{\partial z} \left(\sigma_+(L_-\hat{A}_-) + \sigma_-(L_+\hat{A}_+) \right) \tag{A.29}$$

$$H_R = -\alpha_s\frac{\partial V}{\partial z} \left(\sigma_+L_-\left(A_- + \frac{1}{\rho} \right) + \sigma_-L_+\left(A_+ - \frac{1}{\rho} \right) \right) \tag{A.30}$$

$$H_R = -\alpha_s\frac{\partial V}{\partial z} \left(\sigma_+L_-A_- + \sigma_-L_+A_+ + \frac{1}{\rho}\sigma_+L_- - \frac{1}{\rho}\sigma_-L_+ \right) \tag{A.31}$$

$$H_R = -\alpha_s \frac{\partial V}{\partial z} \left(i\sigma_+ k_- - i\sigma_- k_+ + \frac{1}{\rho}\sigma_+ L_- - \frac{1}{\rho}\sigma_- L_+ \right) \tag{A.32}$$

$$H_R = -i\alpha_s \frac{\partial V}{\partial z} \left(\sigma_+ k_- - \sigma_- k_+ - \frac{i}{\rho}\sigma_+ L_- + \frac{i}{\rho}\sigma_- L_+ \right) \tag{A.33}$$

The Eqs. (A.27) and (A.33) are general expressions for the SIA Hamiltonian. For QRs or QDs whose potential are given by

$$V(\rho) = \frac{a_1}{\rho^2} + a_2\rho^2 - \sqrt{a_1 a_2} + \delta\rho^2 \cos^2 \varphi \tag{A.34}$$

and

$$V(z) = eFz, \tag{A.35}$$

where

$$\frac{\partial V}{\partial \rho} = -\frac{2a_1}{\rho^3} + 2a_2\rho + 2\delta\rho \cos^2(\varphi) \tag{A.36}$$

and

$$\frac{\partial V}{\partial \varphi} = -2\delta\rho^2 \sin(\varphi)\cos(\varphi), \tag{A.37}$$

the Eqs. (A.27) and (A.27) become

$$
\begin{aligned}
H^D_{SIA} = {} & 2\alpha_s\sigma_z \left[\left(-\frac{a_1}{\rho^2} + a_2\rho^2 + \delta\rho^2\cos^2(\varphi) \right) \frac{eB_z}{2c\hbar} - i\delta\sin(\varphi)\cos(\varphi) \right. \\
& - \left. i\delta\rho\sin(\varphi)\cos(\varphi)\frac{\partial}{\partial\rho} - \frac{i}{\rho^2}\left(-\frac{a_1}{\rho^2} + a_2\rho^2 + \delta\rho^2\cos^2(\varphi) \right)\frac{\partial}{\partial\varphi} \right] \quad \text{(A.38)}
\end{aligned}
$$

and

$$
\begin{aligned}
H_R = {} & -\alpha_s\frac{\partial V}{\partial z} \left\{ \sigma_+ \left[e^{-i\varphi}\left(\frac{\partial}{\partial\rho} - \frac{i}{\rho}\frac{\partial}{\partial\varphi} + \frac{eB_z}{2c\hbar}\rho + \frac{1}{\rho} \right) \right] \right. \\
& - \left. \sigma_- \left[e^{i\varphi}\left(\frac{\partial}{\partial\rho} + \frac{i}{\rho}\frac{\partial}{\partial\varphi} - \frac{eB_z}{2c\hbar}\rho + \frac{1}{\rho} \right) \right] \right\}, \quad \text{(A.39)}
\end{aligned}
$$

respectively.

Knowing that $\Psi_m = e^{-im\varphi}/\sqrt{2\pi}$ and applying $\langle\Psi^*_{m_1}|H^D_{SIA}|\Psi_{m_2}\rangle = h^D_{SIA}$ and $\langle\Psi^*_{m_1}|H_R|\Psi_{m_2}\rangle = h_R$, and using the **angular momentum selection rules** presented in Section A.2, we obtain the ex-

pressions

$$
\begin{aligned}
h_{SIA}^{D}(m_1,m_2) &= 2\alpha_s\sigma_z\left\{\left[\left(-\frac{a_1}{\rho^2}+a_2\rho^2+\frac{\delta}{2}\rho^2\right)\frac{eB_z}{2c\hbar}+\left(\frac{a_1}{\rho^4}-a_2-\frac{\delta}{2}\right)m_2\right]\delta_{m_2,m_1}\right.\\
&+ \left[\frac{1}{4}\delta\rho^2\frac{eB_z}{2c\hbar}-\frac{\delta}{4}\rho\frac{\partial}{\partial\rho}-\frac{\delta}{4}(m_2+3)\right]\delta_{m_2,m_1+2}\\
&+ \left.\left[\frac{1}{4}\delta\rho^2\frac{eB_z}{2c\hbar}+\frac{\delta}{4}\rho\frac{\partial}{\partial\rho}-\frac{\delta}{4}(m_2-3)\right]\delta_{m_2,m_1-2}\right\}
\end{aligned}
\tag{A.40}
$$

and

$$
\begin{aligned}
h_R &= -\alpha_s\frac{\partial V}{\partial z}\left\{\sigma_+\left[\frac{\partial}{\partial\rho}-\frac{(m_2-1)}{\rho}+\frac{eB_z}{2c\hbar}\rho\right]\delta_{m_2,m_1-1}\right.\\
&- \left.\sigma_-\left[\frac{\partial}{\partial\rho}+\frac{(m_2+1)}{\rho}-\frac{eB_z}{2c\hbar}\rho\right]\delta_{m_2,m_1+1}\right\}.
\end{aligned}
\tag{A.41}
$$

The matrices in Eqs. (A.40) and (A.41) can be render Hermitian with the symmetrization

$$
H_{herm.} = \frac{1}{2}(H+H^\dagger).
\tag{A.42}
$$

For Eq. (A.40), it means that $(\langle\Psi_{m_1}^*|H_{SIA}^D|\Psi_{m_2}\rangle)^\dagger=\langle\Psi_{-m_2}^*|(H_{SIA}^D)^\dagger|\Psi_{-m_1}\rangle=E_{SIA}^{'D}(m_2,m_1)$. Thus

$$
\begin{aligned}
h_{SIA}^{'D}(m_2,m_1) &= 2\alpha_s(-\sigma_z)\left\{\left[\left(-\frac{a_1}{\rho^2}+a_2\rho^2+\frac{\delta}{2}\rho^2\right)\frac{e(-B_z)}{2c\hbar}\right.\right.\\
&+ \left.\left(\frac{a_1}{\rho^4}-a_2-\frac{\delta}{2}\right)(-m_1)\right]\delta_{-m_2,-m_1}\\
&+ \left[\frac{1}{4}\delta\rho^2\frac{e(-B_z)}{2c\hbar}-\frac{\delta}{4}\rho\frac{\partial}{\partial\rho}-\frac{\delta}{4}(-m_1+3)\right]\delta_{-m_2,-m_1+2}\\
&+ \left.\left[\frac{1}{4}\delta\rho^2\frac{e(-B_z)}{2c\hbar}+\frac{\delta}{4}\rho\frac{\partial}{\partial\rho}-\frac{\delta}{4}(-m_1-3)\right]\delta_{-m_2,-m_1-2}\right\}
\end{aligned}
\tag{A.43}
$$

or

$$
\begin{aligned}
h_{SIA}^{'D}(m_2,m_1) &= 2\alpha_s\sigma_z\left\{\left[\left(-\frac{a_1}{\rho^2}+a_2\rho^2+\frac{\delta}{2}\rho^2\right)\frac{eB_z}{2c\hbar}+\left(\frac{a_1}{\rho^4}-a_2-\frac{\delta}{2}\right)m_1\right]\delta_{m_2,m_1}\right.\\
&+ \left[-\frac{1}{4}\delta\rho^2\frac{eB_z}{2c\hbar}-\frac{\delta}{4}\rho\frac{\partial}{\partial\rho}+\frac{\delta}{4}(m_1-3)\right]\delta_{m_2,m_1-2}\\
&+ \left.\left[-\frac{1}{4}\delta\rho^2\frac{eB_z}{2c\hbar}+\frac{\delta}{4}\rho\frac{\partial}{\partial\rho}+\frac{\delta}{4}(m_1+3)\right]\delta_{m_2,m_1+2}\right\}.
\end{aligned}
\tag{A.44}
$$

We can separating the right side of Eqs. (A.40) and (A.44) into three parts and labeling them

h_1^D, h_2^D, h_3^D, $h_1'^D$, $h_2'^D$ and $h_3'^D$, where

$$h_1^D = 2\alpha_s \sigma_z \left[\left(-\frac{a_1}{\rho^2} + a_2 \rho^2 + \frac{\delta}{2}\rho^2 \right) \frac{eB_z}{2c\hbar} + \left(\frac{a_1}{\rho^4} - a_2 - \frac{\delta}{2} \right) m_2 \right] \delta_{m_2,m_1}, \tag{A.45}$$

$$h_2^D = 2\alpha_s \sigma_z \left[\frac{1}{4}\delta\rho^2 \frac{eB_z}{2c\hbar} - \frac{\delta}{4}\rho\frac{\partial}{\partial\rho} - \frac{\delta}{4}(m_2+3) \right] \delta_{m_2,m_1+2}, \tag{A.46}$$

$$h_3^D = 2\alpha_s \sigma_z \left[\frac{1}{4}\delta\rho^2 \frac{eB_z}{2c\hbar} + \frac{\delta}{4}\rho\frac{\partial}{\partial\rho} - \frac{\delta}{4}(m_2-3) \right] \delta_{m_2,m_1-2}, \tag{A.47}$$

$$h_1'^D = 2\alpha_s \sigma_z \left[\left(-\frac{a_1}{\rho^2} + a_2 \rho^2 + \frac{\delta}{2}\rho^2 \right) \frac{eB_z}{2c\hbar} + \left(\frac{a_1}{\rho^4} - a_2 - \frac{\delta}{2} \right) m_1 \right] \delta_{m_2,m_1}, \tag{A.48}$$

$$h_2'^D = 2\alpha_s \sigma_z \left[-\frac{1}{4}\delta\rho^2 \frac{eB_z}{2c\hbar} - \frac{\delta}{4}\rho\frac{\partial}{\partial\rho} + \frac{\delta}{4}(m_1-3) \right] \delta_{m_2,m_1-2} \tag{A.49}$$

and

$$h_3'^D = 2\alpha_s \sigma_z \left[-\frac{1}{4}\delta\rho^2 \frac{eB_z}{2c\hbar} + \frac{\delta}{4}\rho\frac{\partial}{\partial\rho} + \frac{\delta}{4}(m_1+3) \right] \delta_{m_2,m_1+2}. \tag{A.50}$$

We draw a simple matrix, with m running from -1 to 1, $n = 0$, where the elements are organized in the following position: the first 3x3 block correspond to the spin up and the second, to spin down

$$M_{m_1,m_2} = \frac{1}{2} \begin{pmatrix} h_1^D + h_1'^D & 0 & h_2^D + h_3'^D & 0 & 0 & 0 \\ 0 & h_1^D + h_1'^D & 0 & 0 & 0 & 0 \\ h_3^D + h_2'^D & 0 & h_1^D + h_1'^D & 0 & 0 & 0 \\ 0 & 0 & 0 & -(h_1^D + h_1'^D) & 0 & -(h_2^D + h_3'^D) \\ 0 & 0 & 0 & 0 & -(h_1^D + h_1'^D) & 0 \\ 0 & 0 & 0 & -(h_3^D + h_2'^D) & 0 & -(h_1^D + h_1'^D) \end{pmatrix} \tag{A.51}$$

While for Eq. (A.41) $(\langle \Psi_{m_1}^* | H_R | \Psi_{m_2} \rangle)^\dagger = \langle \Psi_{-m_2}^* | (H_R)^\dagger | \Psi_{-m_1} \rangle = h_R'(m_2, m_1)$

$$\begin{aligned} h_R' &= -\alpha_s \frac{\partial V}{\partial z} \left\{ (-\sigma_-) \left[\frac{\partial}{\partial\rho} - \frac{(-m_1-1)}{\rho} + \frac{e(-B_z)}{2c\hbar}\rho \right] \delta_{-m_2,-m_1-1} \right. \\ &\quad - (-\sigma_+) \left[\frac{\partial}{\partial\rho} + \frac{(-m_1+1)}{\rho} - \frac{e(-B_z)}{2c\hbar}\rho \right] \delta_{-m_2,-m_1+1} \right\} \end{aligned} \tag{A.52}$$

or

$$h'_R = -\alpha_s \frac{\partial V}{\partial z} \left\{ (-\sigma_-) \left[\frac{\partial}{\partial \rho} + \frac{(m_1+1)}{\rho} - \frac{e(B_z)}{2c\hbar}\rho \right] \delta_{m_2,m_1+1} \right.$$

$$\left. + (\sigma_+) \left[\frac{\partial}{\partial \rho} - \frac{(m_1-1)}{\rho} + \frac{e(B_z)}{2c\hbar}\rho \right] \delta_{m_2,m_1-1} \right\}. \tag{A.53}$$

Calling now

$$h_{R_1} = -\alpha_s \frac{\partial V}{\partial z} \sigma_+ \left[\frac{\partial}{\partial \rho} - \frac{(m_2-1)}{\rho} + \frac{eB_z}{2c\hbar}\rho \right] \delta_{m_2,m_1-1} \tag{A.54}$$

$$h_{R_2} = \alpha_s \frac{\partial V}{\partial z} \sigma_- \left[\frac{\partial}{\partial \rho} + \frac{(m_2+1)}{\rho} - \frac{eB_z}{2c\hbar}\rho \right] \delta_{m_2,m_1+1} \tag{A.55}$$

$$h'_{R_1} = \alpha_s \frac{\partial V}{\partial z} \sigma_- \left[\frac{\partial}{\partial \rho} + \frac{(m_1+1)}{\rho} - \frac{e(B_z)}{2c\hbar}\rho \right] \delta_{m_2,m_1+1} \tag{A.56}$$

$$h'_{R_2} = -\alpha_s \frac{\partial V}{\partial z} \sigma_+ \left[\frac{\partial}{\partial \rho} - \frac{(m_1-1)}{\rho} + \frac{e(B_z)}{2c\hbar}\rho \right] \delta_{m_2,m_1-1} \tag{A.57}$$

In the matrix these elements would appear as

$$M_{m_1,m_2} = \frac{1}{2} \begin{pmatrix} 0 & 0 & 0 & 0 & 0 & 0 \\ 0 & 0 & 0 & h_{R_1}+h'_{R_2} & 0 & 0 \\ 0 & 0 & 0 & 0 & h_{R_1}+h'_{R_2} & 0 \\ 0 & h_{R_2}+h'_{R_1} & 0 & 0 & 0 & 0 \\ 0 & 0 & h_{R_2}+h'_{R_1} & 0 & 0 & 0 \\ 0 & 0 & 0 & 0 & 0 & 0 \end{pmatrix} \tag{A.58}$$

A.2   Angular Momentum Selection Rules

The section rules for angular momentum are

$$\int_0^{2\pi} e^{im_1\varphi} e^{-im_2\varphi} d\varphi = 2\pi \delta_{m_2,m_1} \tag{A.59}$$

$$\int_0^{2\pi} e^{im_1\varphi} \frac{\partial}{\partial \varphi} e^{-im_2\varphi} d\varphi = -2\pi i m_2 \delta_{m_2,m_1} \tag{A.60}$$

$$\int_0^{2\pi} e^{im_1\varphi} \frac{\partial^2}{\partial^2 \varphi} e^{-im_2\varphi} d\varphi = -2\pi m_2^2 \delta_{m_2,m_1} \tag{A.61}$$

$$\int_0^{2\pi} e^{im_1\varphi} e^{\pm i\varphi} e^{-im_2\varphi} d\varphi = 2\pi \delta_{m_2,m_1 \pm 1} \tag{A.62}$$

$$\int_0^{2\pi} e^{im_1\varphi} e^{\pm i\varphi} \frac{\partial}{\partial \varphi} e^{-im_2\varphi} d\varphi = -2\pi i (m_2 \pm 1) \delta_{m_2,m_1 \pm 1} \tag{A.63}$$

$$\int_0^{2\pi} e^{im_1\varphi} \cos\varphi e^{\pm i\varphi} e^{-im_2\varphi} d\varphi = \pi \delta_{m_2,m_1 \pm 0,2} \tag{A.64}$$

$$\int_0^{2\pi} e^{im_1\varphi} \cos\varphi e^{\pm i\varphi} \frac{\partial}{\partial \varphi} e^{-im_2\varphi} d\varphi = -i\pi m_2 \delta_{m_2,m_1 \pm 0,2} \tag{A.65}$$

$$\int_0^{2\pi} e^{im_1\varphi} \cos^3\varphi e^{\pm i\varphi} e^{-im_2\varphi} d\varphi = \frac{3\pi}{4} \delta_{m_2,m_1 \pm 0,2} + \frac{\pi}{4} \delta_{m_2,m_1 \mp 2} + \frac{\pi}{4} \delta_{m_2,m_1 \pm 4} \tag{A.66}$$

$$\int_0^{2\pi} e^{im_1\varphi} \cos^3\varphi e^{\pm i\varphi} \frac{\partial}{\partial \varphi} e^{-im_2\varphi} d\varphi = -\frac{3\pi}{4} i m_2 \delta_{m_2,m_1 \pm 0,2} - \frac{\pi}{4} \delta_{m_2,m_1 \mp 2} - \frac{\pi}{4} i m_2 \delta_{m_2,m_1 \pm 4} \tag{A.67}$$

$$\int_0^{2\pi} e^{im_1\varphi} \sin\varphi e^{\pm i\varphi} e^{-im_2\varphi} d\varphi = \pm \pi i \delta_{m_2,m_1} \mp \pi i \delta_{m_2,m_1 \pm 2} \tag{A.68}$$

$$\int_0^{2\pi} e^{im_1\varphi} \sin\varphi e^{\pm i\varphi} \frac{\partial}{\partial \varphi} e^{-im_2\varphi} d\varphi = \pm \pi m_2 \delta_{m_2,m_1} \mp \pi m_2 \delta_{m_2,m_1 \pm 2} \tag{A.69}$$

$$\begin{aligned}
\int_0^{2\pi} e^{im_1\varphi} \sin^2\varphi \cos\varphi e^{\pm i\varphi} e^{-im_2\varphi} d\varphi &= \frac{\pi}{4} \delta_{m_2,m_1} + \frac{\pi}{4} \delta_{m_2,m_1 \pm 2} \\
&\quad - \frac{\pi}{4} \delta_{m_2,m_1 \mp 2} - \frac{\pi}{4} \delta_{m_2,m_1 \pm 4}
\end{aligned} \tag{A.70}$$

$$\begin{aligned}
\int_0^{2\pi} e^{im_1\varphi} \sin^2\varphi \cos\varphi e^{\pm i\varphi} \frac{\partial}{\partial \varphi} e^{-im_2\varphi} d\varphi &= -\frac{\pi}{4} i m_2 \delta_{m_2,m_1} - \frac{\pi}{4} i m_2 \delta_{m_2,m_1 \pm 2} \\
&\quad + \frac{\pi}{4} i m_2 \delta_{m_2,m_1 \mp 2} + \frac{\pi}{4} i m_2 \delta_{m_2,m_1 \pm 4}
\end{aligned} \tag{A.71}$$

Appendix B

TILTED MAGNETIC FIELD

To build a Hamiltonian considering a tilted magnetic field, $\vec{B}$, we will assume that it is applied in the xz plane with an angle θ with respect to the growth direction (z-direction),

$$\vec{B} = B\sin(\theta)\hat{i} + B\cos(\theta)\hat{k} \tag{B.1}$$

This tilted magnetic field affects the kinetic part of the Hamiltonian,

$$H = \frac{1}{2\mu^*}|\vec{p} - e\vec{A}|^2, \tag{B.2}$$

where the potential vector $\vec{A}$ is related to the field by

$$\vec{B} = \vec{\nabla} \times \vec{A}. \tag{B.3}$$

To solve the Hamiltonian of Eq. (B.2), we employ the following Gauge

$$\vec{A} = \frac{B_z}{2}(-y, x, 0) + B_x(0, -z, 0) \tag{B.4}$$

where $B_x = B\sin(\theta)$ and $B_z = B\cos(\theta)$ and we get the following result

$$H = \frac{1}{2\mu^*}\left(i\hbar\frac{\partial}{\partial x} + e\frac{B_z}{2}y\right)^2 + \frac{1}{2\mu^*}\left(i\hbar\frac{\partial}{\partial y} - e\frac{B_z}{2}x - eB_xz\right)^2 + \frac{p_z^2}{2\mu^*} \tag{B.5}$$

The above equation, can be rewritten in cylindrical coordinates, using

$$k_x = -i\hbar\frac{\partial}{\partial x} + e\frac{B_z}{2}y, \tag{B.6}$$

$$k_y = -i\hbar \frac{\partial}{\partial y} - e\frac{B_z}{2}x - eB_x z \tag{B.7}$$

and

$$\vec{A} = \frac{B_z}{2}\rho\,\hat{\varphi} - B_x z(\sin(\varphi)\hat{\rho} + \cos(\varphi)\hat{\varphi}). \tag{B.8}$$

The Hamiltonian in cylindrical coordinates will be

$$
\begin{aligned}
H &= \frac{1}{2\mu^*}\left\{ -\hbar^2\nabla^2 + 2ie\hbar\left[B_z\frac{\partial}{\partial\varphi} + zB_x\left(\sin(\varphi)\frac{\partial}{\partial\rho} + \frac{\cos(\varphi)}{\rho}\frac{\partial}{\partial\varphi}\right)\right]\right\} \\
&\quad + \frac{1}{2\mu^*}\left(\frac{e^2 B_z^2\rho^2}{4} + e^2 B_x^2 z^2 + e^2 B_z B_x z\rho\cos(\varphi)\right).
\end{aligned}
\tag{B.9}
$$

or

$$
\begin{aligned}
H &= -\frac{\hbar^2}{2\mu^*}\left[\frac{1}{\rho}\frac{\partial}{\partial\rho}\left(\rho\frac{\partial}{\partial\rho}\right) + \frac{1}{\rho^2}\frac{\partial^2}{\partial\varphi^2} + \frac{\partial^2}{\partial z^2}\right] + \frac{ie\hbar B_z}{2\mu^*}\frac{\partial}{\partial\varphi} + \frac{e^2 B_z^2\rho^2}{8\mu^*} + V_{QW}(z) \\
&\quad - \frac{ie\hbar z B_x}{\mu^*}\left(\sin(\varphi)\frac{\partial}{\partial\rho} + \frac{\cos(\varphi)}{\rho}\frac{\partial}{\partial\varphi}\right) + \frac{1}{2\mu^*}\left(e^2 B_x^2 z^2 - e^2 B_z B_x z\rho\cos(\varphi)\right)
\end{aligned}
\tag{B.10}
$$

The Hamiltonian, $H = H_{B_z} + H_{B_{\rho z}}$, can then be separated into the contribution due to a perpendicular magnetic field,

$$H_{B_z} = -\frac{\hbar^2}{2\mu^*}\left[\frac{1}{\rho}\frac{\partial}{\partial\rho}\left(\rho\frac{\partial}{\partial\rho}\right) + \frac{1}{\rho^2}\frac{\partial^2}{\partial\varphi^2} + \frac{\partial^2}{\partial z^2}\right] + \frac{ie\hbar B_z}{2\mu^*}\frac{\partial}{\partial\varphi} + \frac{e^2 B_z^2\rho^2}{8\mu^*} + V_{QW}(z) \tag{B.11}$$

and the terms due to the in-plane component

$$H_{B_{\rho z}} = -\frac{ie\hbar z B_x}{\mu^*}\left(\sin(\varphi)\frac{\partial}{\partial\rho} + \frac{\cos(\varphi)}{\rho}\frac{\partial}{\partial\varphi}\right) + \frac{1}{2\mu^*}\left(e^2 B_x^2 z^2 - e^2 B_z B_x z\rho\cos(\varphi)\right) \tag{B.12}$$

B.1 Zeeman Splitting due to Tilted Magnetic Field

The applied magnetic field breaks the spin degeneracy and the induced Zeeman splitting due to the tilted magnetic field is given by

$$H_{ZS} = \frac{g\mu_B}{2}\vec{B}\cdot\vec{\sigma}, \tag{B.13}$$

or

$$H_{ZS} = \frac{g\mu_B}{2}\left(B_x\sigma_x + B_y\sigma_y + B_z\sigma_z\right). \tag{B.14}$$

Using the relations $\sigma_x = \sigma_+ + \sigma_-$ and $\sigma_y = -i(\sigma_+ - \sigma_-)$

$$H_{ZS} = \frac{g\mu_B}{2}\left(B_x(\sigma_+ + \sigma_-) - iB_y(\sigma_+ - \sigma_-) + B_z\sigma_z\right) \tag{B.15}$$

B.2 SO Due to Tilted Magnetic Field

The tilted field contribution to the SO Hamiltonian is introduced by just replacing, in Eq. (A.7) (Appendix I), k_x, k_y and k_z by k'_x, k'_y and k'_z, respectively, where

$$k'_x = k_x, \tag{B.16}$$

$$k'_y = k_y - \frac{ezB_x}{c\hbar} \tag{B.17}$$

and

$$k'_z = k_z. \tag{B.18}$$

Thus, the Eq. (A.5) (Appendix I) becomes

$$H_{SIA}^{TF} = \alpha_s\left[\left(\sigma_x\frac{\partial V}{\partial y} - \sigma_y\frac{\partial V}{\partial x}\right)k'_z + \frac{\partial V}{\partial z}\left(\sigma_y k_{x'} - \sigma_x k_{y'}\right) + \sigma_z\left(\frac{\partial V}{\partial x}k_{y'} - \frac{\partial V}{\partial y}k'_x\right)\right] \tag{B.19}$$

which in terms of k_x, k_y and k_z is

$$
\begin{aligned}
H_{SIA}^{TF} &= \alpha_s\left[\left(\sigma_x\frac{\partial V}{\partial y} - \sigma_y\frac{\partial V}{\partial x}\right)k_z + \frac{\partial V}{\partial z}\left[\sigma_y k_x - \sigma_x\left(k_y - \frac{ezB_x}{c\hbar}\right)\right]\right.\\
&+ \left.\sigma_z\left[\frac{\partial V}{\partial x}\left(k_y - \frac{ezB_x}{c\hbar}\right) - \frac{\partial V}{\partial y}k_x\right]\right]
\end{aligned} \tag{B.20}
$$

After some algebra

$$
\begin{aligned}
H_{SIA}^{TF} &= \alpha_s\left[\left(\sigma_x\frac{\partial V}{\partial y} - \sigma_y\frac{\partial V}{\partial x}\right)k_z + \frac{\partial V}{\partial z}\left(\sigma_y k_x - \sigma_x k_y\right)\right.\\
&+ \left.\sigma_z\left(\frac{\partial V}{\partial x}k_y - \frac{\partial V}{\partial y}k_x\right)\right] + \alpha_s\left(\frac{\partial V}{\partial z}\sigma_x\frac{ezB_x}{c\hbar} - \frac{\partial V}{\partial x}\sigma_z\frac{ezB_x}{c\hbar}\right)
\end{aligned} \tag{B.21}
$$

or in a simplified way

$$H_{SIA}^{TF} = H_{SIA} + \alpha_s \left(\frac{\partial V}{\partial z} \sigma_x \frac{ezB_x}{c\hbar} - \frac{\partial V}{\partial x} \sigma_z \frac{ezB_x}{c\hbar} \right),$$

(B.22)

where the terms can be labeled as

$$H_{SIA}^{D(TF)} = -\alpha_s \frac{\partial V}{\partial x} \sigma_z \frac{ezB_x}{c\hbar}$$

(B.23)

and

$$H_R^{TF} = \alpha_s \frac{\partial V}{\partial z} \sigma_x \frac{ezB_x}{c\hbar} = \alpha_s \frac{\partial V}{\partial z} (\sigma_+ + \sigma_-) \frac{ezB_x}{c\hbar}.$$

(B.24)

Appendix C

PARAMETERS OF In$_{0.36}$Ga$_{0.64}$As AND In$_{0.36}$Ga$_{0.64}$As$_{0.088}$N$_{0.012}$ CALCULATED BY LINEAR INTERPOLATION

Table C.1: Calculated parameters for the samples In$_{0.36}$Ga$_{0.64}$As and In$_{0.36}$Ga$_{0.64}$As$_{0.088}$N$_{0.012}$ [1]

Parameters	GaN	GaAs	InAs	InN	In$_{0.36}$Ga$_{0.64}$As	In$_{0.36}$Ga$_{0.64}$As$_{0.988}$N$_{0.012}$
$E_g(eV)$	3.299	1.519	0.417	1.94	1.0106	0.9503
$a_c(eV)$	-2.2	-7.17	-5.08	-1.85	-6.417	-6.365
$a_v(eV)$	-0.69	-1.16	-1.00	-0.70	-1.102	-1.097
$b(eV)$	-2.20	-2.00	-1.80	-1.20	-1.928	-1.927
$d(eV)$	-3.4	-4.8	-3.6	-9.3	-4.368	-4.382
$c_{11}(GPa)$	293	1221	833	187	1081	1071
$c_{12}(GPa)$	159	566	453	125	525	521
$c_{44}(GPa)$	155	600	396	86	526	522
$a(nm)$	0.452	0.565	0.606	0.498	0.580	0.578
m^*	0.15	0.067	0.026	0.12	0.052	0.053
γ_1	2.67	6.98	20.0	3.72	11.67	11.56
γ_2	0.75	2.06	8.5	1.26	4.38	4.34
γ_3	1.10	2.93	9.2	1.63	5.19	5.14
g	-	-0.44	-15	-	-5.68	-

Bibliography

[1] I. Vurgaftman, J. R. Meyer, and L. R. Ram-Mohan, J. Appl. Phys. **89**, 5815 (2001).

Appendix D

MATRIX ELEMENTS FOR QR LUTTINGER HAMILTONIAN

Luttinger Hamiltonian

$$H(m) = \begin{pmatrix} H_{1,1} & H_{1,2} & H_{1,3} & 0 \\ H_{2,1} & H_{2,2} & 0 & H_{2,4} \\ H_{3,1} & 0 & H_{3,3} & H_{3,4} \\ 0 & H_{4,2} & H_{4,3} & H_{4,4} \end{pmatrix}. \qquad \text{(D.1)}$$

The Hilbert space of solutions can be separated into orthogonal subspaces according to the wavenumber m, where the matrix elements are given by

$$H_{1,1} = \frac{2\pi\hbar^2}{2m_0}(\gamma_1 + \gamma_2)\left[\frac{\partial^2}{\partial\rho^2} + \frac{1}{\rho}\frac{\partial}{\partial\rho} - \frac{m^2}{\rho^2}\right] + \frac{2\pi\hbar^2}{2m_0}(\gamma_1 - 2\gamma_2)\frac{\partial^2}{\partial z^2} + V(r);$$

$$H_{2,2} = \frac{2\pi\hbar^2}{2m_0}(\gamma_1 - \gamma_2)\left[\frac{\partial^2}{\partial\rho^2} + \frac{1}{\rho}\frac{\partial}{\partial\rho} - \frac{(m-1)^2}{\rho^2}\right] + \frac{2\pi\hbar^2}{2m_0}(\gamma_1 + 2\gamma_2)\frac{\partial^2}{\partial z^2} + V(r);$$

$$H_{3,3} = \frac{2\pi\hbar^2}{2m_0}(\gamma_1 - \gamma_2)\left[\frac{\partial^2}{\partial\rho^2} + \frac{1}{\rho}\frac{\partial}{\partial\rho} - \frac{(m-2)^2}{\rho^2}\right] + \frac{2\pi\hbar^2}{2m_0}(\gamma_1 + 2\gamma_2)\frac{\partial^2}{\partial z^2} + V(r);$$

$$H_{4,4} = \frac{2\pi\hbar^2}{2m_0}(\gamma_1 + \gamma_2)\left[\frac{\partial^2}{\partial\rho^2} + \frac{1}{\rho}\frac{\partial}{\partial\rho} - \frac{(m-3)^2}{\rho^2}\right] + \frac{2\pi\hbar^2}{2m_0}(\gamma_1 - 2\gamma_2)\frac{\partial^2}{\partial z^2} + V(r);$$

$$H_{1,2} = -2\pi \frac{\hbar^2 \sqrt{3} \gamma_3}{4m_0} \left[\frac{\partial^2}{\partial z \partial \rho} - \frac{m-1}{\rho} \frac{\partial}{\partial z} \right];$$

$$H_{1,3} = 2\pi \frac{\hbar^2 \sqrt{3}}{4m_0} (\gamma_2 + \gamma_3) \times \left[-\frac{\partial^2}{\partial^2 \rho} + \frac{2m-3}{\rho} \frac{\partial}{\partial \rho} - \frac{1}{\rho^2} (m^2 - 2m) \right];$$

$$H_{2,1} = -2\pi \frac{\hbar^2 \sqrt{3} \gamma_3}{4m_0} \left[\frac{\partial^2}{\partial z \partial \rho} + \frac{m}{\rho} \frac{\partial}{\partial z} \right];$$

$$H_{2,4} = 2\pi \frac{\hbar^2 \sqrt{3}}{4m_0} (\gamma_2 + \gamma_3) \times \left[-\frac{\partial^2}{\partial^2 \rho} + \frac{(2m-5)}{\rho} \frac{\partial}{\partial \rho} - \frac{1}{\rho^2} (m^2 - 4m + 3) \right];$$

$$H_{3,1} = 2\pi \frac{\hbar^2 \sqrt{3}}{4m_0} (\gamma_2 + \gamma_3) \times \left[-\frac{\partial^2}{\partial^2 \rho} + \frac{1-2m}{\rho} \frac{\partial}{\partial \rho} - \frac{1}{\rho^2} (m^2 - 2m) \right];$$

$$H_{3,4} = -2\pi \frac{\hbar^2 \sqrt{3} \gamma_3}{4m_0} \left[\frac{\partial^2}{\partial z \partial \rho} + \frac{m-3}{\rho} \frac{\partial}{\partial z} \right];$$

$$H_{4,2} = 2\pi \frac{\hbar^2 \sqrt{3}}{4m_0} (\gamma_2 + \gamma_3) \times \left[-\frac{\partial^2}{\partial^2 \rho} + \frac{3-2m}{\rho} \frac{\partial}{\partial \rho} - \frac{1}{\rho^2} (m^2 - 4m + 3) \right];$$

$$H_{4,3} = -2\pi \frac{\hbar^2 \sqrt{3} \gamma_3}{4m_0} \left[\frac{\partial^2}{\partial z \partial \rho} + \frac{m-2}{\rho} \frac{\partial}{\partial z} \right]. \tag{D.2}$$